Geochemical ngerprints of glacially eroded bedrock from West Antarctica: Detrital thermochronology, radiogenic isotope systematics and trace element geochemistry in Late Holocene glacial-marine sediments

Journal Item

Geochemical fingerprints of glacially eroded bedrock from West Antarctica: Detrital thermochronology, radiogenic isotope systematics and trace element geochemistry in Late Holocene glacial-marine sediments

Patric Simões Pereira, Tina van de Flierdt, Sidney R. Hemming, Samantha J. Hammond, Gerhard Kuhn, Stefanie Brachfeld, Cathleen Doherty, Claus-Dieter Hillenbrand

PII:	S0012-8252(17)30597-4
DOI:	doi:10.1016/j.earscirev.2018.04.011
Reference:	EARTH 2621
To appear in:	*Earth-Science Reviews*
Received date:	17 November 2017
Revised date:	20 April 2018
Accepted date:	30 April 2018

Please cite this article as: Patric Simões Pereira, Tina van de Flierdt, Sidney R. Hemming, Samantha J. Hammond, Gerhard Kuhn, Stefanie Brachfeld, Cathleen Doherty, Claus-Dieter Hillenbrand , Geochemical fingerprints of glacially eroded bedrock from West Antarctica: Detrital thermochronology, radiogenic isotope systematics and trace element geochemistry in Late Holocene glacial-marine sediments. The address for the corresponding author was captured as affiliation for all authors. Please check if appropriate. Earth(2018), doi:10.1016/j.earscirev.2018.04.011

Geochemical fingerprints of glacially eroded bedrock from West Antarctica: detrital thermochronology, radiogenic isotope systematics and trace element geochemistry in Late Holocene glacial-marine sediments

Patric Simões Pereira[1,2,*], Tina van de Flierdt[2], Sidney R. Hemming[3,4], Samantha J. Hammond[5], Gerhard Kuhn[6], Stefanie Brachfeld[7], Cathleen Doherty[8] and Claus-Dieter Hillenbrand[9]

[1]Grantham Institute for Climate Change and the Environment, Imperial College London, South Kensington Campus, London SW7 2AZ, UK
[2]Department of Earth Science and Engineering, Imperial College London, South Kensington Campus, London SW7 2AZ, UK
[3]Department of Earth and Environmental Sciences, Columbia University, Lamont-Doherty Earth Observatory, Palisades, New-York 10964, USA
[4]Department of Earth and Environmental Sciences, Columbia University, New-York 10027, USA
[5]Department of Environment, Earth and Ecosystems, The Open University, Walton Hall, Milton Keynes MK7 6AA, UK
[6]Alfred-Wegener-Institut, Helmholtz-Zentrum für Polar- und Meeresforschung, Marine Geosciences, Bremerhaven 27568, Germany
[7]Department of Earth and Environmental Studies, Montclair State University, Montclair, New Jersey 07043, USA
[8]Environmental and Occupational Health Sciences Institute, Rutgers University, Piscataway, New Jersey 08854, USA

[9]British Antarctic Survey, High Cross, Madingley Road, Cambridge CB3 0ET, UK

[*]Corresponding author: p.simoes-pereira14@imperial.ac.uk

Abstract

Geochemical provenance studies of glacial-marine sediments provide a powerful approach to describe subglacial geology, sediment transport pathways, and past ice sheet dynamics. The marine-based West Antarctic Ice Sheet (WAIS) is considered highly vulnerable to ocean warming and sea level rise that is likely to cause its rapid and irreversible retreat. Studies of its past response to climate change are hence essential for projecting its future behaviour. The application of radiogenic and trace element provenance studies for past ice sheet reconstructions requires surveying the geographic variability of geochemical compositions of glaciomarine sediments. In this study, we characterize the provenance of the detrital fraction of 67 Late Holocene marine sediment samples collected off the Pacific margin of West Antarctica (60°W to 160°W), including $^{40}Ar/^{39}Ar$ ages of individual hornblende and biotite grains (>150µm), as well as Sr and Nd isotope and trace element composition of the fine-grained (<63µm) sediment fraction. Overall, this approach allows differentiating West Antarctica into five source regions: the Antarctic Peninsula, Bellingshausen Sea, Amundsen Sea, Wrigley Gulf-Hobbs Coast and Sulzberger Bay. Minor geochemical variability is found within each individual sector due to local variability in onland geology. $^{40}Ar/^{39}Ar$ ages of iceberg-rafted hornblende and biotite grains record primarily Carboniferous to Lates Quaternary ages (~0 to 380 Ma), with a notable age peak of ~100 Ma, associated with plutonic intrusions or deformation events during the mid-Cretaceous. Permian-Jurassic $^{40}Ar/^{39}Ar$ ages are widespread in the Amundsen Sea sector, marking episodes of large-volume magmatism along the long-lived continental margin. Metasedimentary rocks and Late Cenozoic alkali basalts in West Antarctica cannot be detected using detrital hornblende and biotite $^{40}Ar/^{39}Ar$ ages due to the absence or small grain-size (i.e. <150µm) of these minerals in such rocks. These sources can however be readily recognized by their fine-grained geochemical composition. In addition, geographic trends in the provenance from proximal to distal sites provide insights into major sediment transport pathways. While the transport of fine-grained detritus follows bathymetric cross-shelf troughs, the distribution of iceberg-rafted grains shows influence by transport in the Antarctic Coastal Current. Our study provides the first systematic

geochemical characterisation of sediment provenance off West Antarctica, and highlights the importance of combining multiple provenance approaches in different size fractions of glacial-marine sediments, and paves the way to investigate past WAIS dynamics.

Key words: Geochemical provenance, West Antarctic Ice Sheet, subglacial geology, sediment transport pathways

1. Introduction

The West Antarctic Ice Sheet (WAIS) holds enough ice to raise global sea-level by 4.3 m if completely melted (**Fretwell et al., 2013**). Its base rests largely on surfaces of bedrock and sedimentary strata that are well below sea level with an inland-deepening slope, making the WAIS vulnerable to changing environmental conditions (e.g. **Oppenheimer, 1998**), particularly to ocean warming and sea-level rise via the marine ice sheet instability hypothesis (e.g. **Rignot and Jacobs, 2002; Schoof, 2007; Katz and Worster, 2010; Jacobs et al., 2011; Joughin and Alley, 2011; Pritchard et al., 2012**) and/or marine ice cliff instability (**DeConto and Pollard, 2016; Wise et al., 2017**). This vulnerability is confirmed by modern observational data, which show thinning of ice shelves, acceleration of ice stream flow, and overall mass loss in the Pacific sector of the WAIS (**Payne et al., 2004; Rignot et al., 2008; Pritchard et al., 2009, 2012; Shepherd et al., 2012; Mouginot et al., 2014**). Most of the current retreat occurs in the Amundsen Sea sector, which drains approximately ~35% of the WAIS. High rates of mass loss originate from the Pine Island and Thwaites glaciers, with potential collapse being hypothesised to occur in as little as ~400 years (**Oppenheimer, 1998** and references therein**; Vaughan et al., 2011; Joughin et al., 2014**). The proposed mechanism for collapse is an irreversible retreat of the grounding line (**Schoof, 2007; Katz and Worster, 2010**), facilitated by the landward dipping bed under the WAIS. Thereby, the bathymetric setting of the continental shelf may trigger initial retreat by allowing relatively warm Circumpolar Deep Water that is upwelling onto the shelf to enter sub-ice shelf cavities through cross-shelf troughs carved by past ice stream advances (e.g. **Walker et al, 2007; 2013; Jenkins et al., 2010, 2016**).

While modern and historical processes leading to ice-sheet loss are increasingly well studied and understood (e.g. **Hillenbrand et al. 2017; Smith et al., 2017; Turner et al., 2017**), reconstructions of the past stability of the WAIS are still sparse (e.g. **Scherer et al., 1998; Hillenbrand et al., 2002, 2009a; Pollard and DeConto, 2009; Naish et al., 2009; Vaughan et al., 2011**). One promising tool to learn about past ice stability has been to study the provenance of

marine detrital sediments. Radiogenic isotope fingerprinting and dating has been successfully applied to reconstruct ice sheet history in the Northern Hemisphere (e.g. **Gwiazda et al., 1996; Hemming et al., 1998, Hemming and Hajdas, 2003; Peck et al., 2007; Downing et al., 2013; Reyes et al., 2014)** and around East Antarctica (e.g. **Williams et al., 2010; Pierce et al., 2011, 2014, 2017; Cook et al., 2013, 2014, 2017).** Geochemical (i.e. radiogenic isotope composition) studies of glacially derived sediments with a West Antarctic provenance have so far been restricted to the Ross Sea (**Farmer et al., 2006; Licht and Palmer, 2013**; **Licht et al., 2014**), glacial till samples from distinct ice streams (**Farmer and Licht, 2016; Licht et al., 2014; Welke et al., 2016**), and only a few marine sediment core top analyses along the West Antarctic margin (**Walter et al., 2000; Roy et al., 2007; van de Flierdt et., 2007; Hemming et al., 2007**).

In this study, we close this gap and describe the detailed geochemical provenance of glacially derived Late Holocene sediments along the Pacific margin of West Antarctica. Our primary motivation is to identify isotopic and geochemical fingerprints for individual WAIS sectors, and to characterize its subglacial geology building on the pioneering work of **Roy et al. (2007), van de Flierdt et al. (2007)** and **Hemming et al. (2007)**. Paramount to such studies is the knowledge of the geological history of the exposed and subglacial bedrock (**Figs. 1, 2**) and its overall geochemical variability. Outcrop studies, integrated with airborne and field geophysical campaigns have significantly increased our knowledge of the hidden bedrock below the Antarctic Ice Sheet (e.g**. Ferraccioli et al., 2009; Smith et al., 2013; Jordan et al., 2013a,b; Aitken et al., 2014**). Investigations of sediments that are shed from Antarctica can also contribute to understanding subglacial geology as well as providing the groundwork for using this approach to document the past history of the ice sheets. Here we present results on the geochemical signature of 67 surface sediment samples using $^{40}Ar/^{39}Ar$ ages of individual hornblende and biotite grains (>150µm or >63µm), and strontium (Sr) and neodymium (Nd) isotope ratios and trace element compositions of the fine-grained fraction (<63µm). We present these results in the context of published studies of the geology and geochemistry of West Antarctica from field observations and geophysical investigations. By

combining different provenance tools, we characterize source sectors of glacigenic detritus, a vital precondition for unravelling the history of the WAIS by tracing down-core provenance changes in marine sediment records. We place a particular emphasis on the Amundsen Sea sector, and relate our new sediment provenance results to specific ice drainage signatures, as well as pathways and transport mechanisms that may deliver sediments to their sites of deposition.

2. Regional Framework of West Antarctica

2.1. Tectonic history

The Antarctic continent preserves a geological record from ~3.5 Ga to present. Most known Precambrian rocks are found in East Antarctica (see **Boger, 2011** for a recent review), while West Antarctica generally has a younger, largely Phanerozoic, geological history. West Antarctica consists of four micro-continental blocks: the Antarctic Peninsula, Ellsworth-Whitmore Mountains, Thurston Island and Marie Byrd Land (**Dalziel and Elliot, 1982)** (**Figs. 1, 2**).

The 'birth' of West Antarctica is largely associated with the onset of the accretionary Terra Australis (Ross) Orogeny (~510 Ma). The Terra Australis Orogeny took place after suturing of West Gondwana (South American and South African shields) and the Australo-Antarctic plates (Kuunga Orogen), which shifted the locus of active subduction from between the pre-collision complexes of Gondwana towards the Proto-Pacific margin (**Cawood, 2005**). This orogenic event resulted in deformation of passive margin sediments, formation of back-arc basins with quiescent sedimentation (Ellsworth-Whitmore Mountains, **Fig. 1**), and led to arc-type plutonism and subsequent crustal accretion onto the Gondwana margin (**Cawood, 2005; Boger, 2011**).

Convergence along the Pacific margin of Gondwana led to deposition and subsequent accretion of Cambrian-Ordovician turbiditic sequences, and intrusion of Devonian-Carboniferous (~375–345 Ma) granitoids. Relicts of these Early Palaeozoic rocks are found in the Ross province of Marie Byrd Land (**Pankhurst et al., 1998; Mukasa and Dalziel, 2000**), on Thurston Island (**Pankhurst**

et al., 1993; Riley et al., 2017) and in the Eastern Domain of the Antarctic Peninsula (**Millar et al., 2002**), considered as the innermost and oldest arc-terranes in West Antarctica (**Vaughan and Storey, 2000**) (**Figs. 1, 2**).

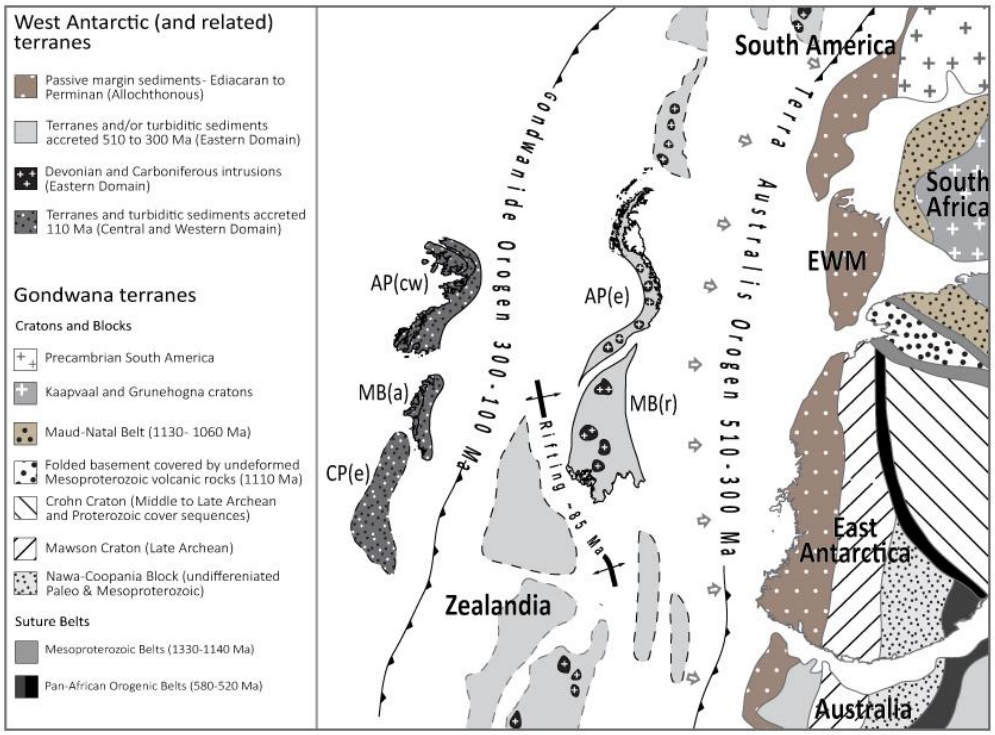

Figure 1: Tectonic reconstruction of West Antarctica during the Early Palaeozoic to Cretaceous (modified from Boger, 2011). AP – Antarctic Peninsula, MB(a) – Amundsen Province of Marie Byrd Land, related to the Central Domain, MB(r) – Ross Province of Marie Byrd Land, related to the Eastern Domain, CP – Campbell Plateau. Indices: e – Eastern Domain, c – Central Domain, w – Western Domain.

During the late Carboniferous, collision of Gondwana with Laurentia terminated the Terra Australis Orogeny, which was followed by the Gondwanide Orogeny (**Fig. 1**). This transition marked the initiation of a series of magmatic arc terranes, largely calc-alkaline granodiorite, diorite, and monzogranite intrusions in the Central Domain (Amundsen Province) of Marie Byrd Land and in the Central Domain of the Antarctic Peninsula during the Late Palaeozoic-Mesozoic. Notable episodes of

magmatism occurred during the late Triassic-early Jurassic (236-199 Ma), mid-Jurassic (~180-160 Ma) and Early to Late Cretaceous (~140-80) (**Leat et al., 1995; Storey et al., 1996**). Though initially disconnected from Antarctica, these terranes became accreted to the continent by the end of the Cretaceous.

The outermost terrane belt in West Antarctica, the Western Domain of the Antarctic Peninsula (**Vaughan and Storey, 2000**) is composed of Carboniferous to Late Cretaceous accretionary sedimentary rocks such as those found on Alexander Island (**Fig. 2**). This terrane accreted to the West Antarctic margin by 103 – 107 Ma, leading to back-arc plutonism and metamorphism of the Western and Central Domain in the mid-Cretaceous (**Wendt et al., 2008; Vaughan et al., 2012a**).

Gondwana break-up led to extensive extrusion of Jurassic volcanic rocks documented by outcrops in the Antarctic Peninsula, and resulted in rifting away of Zealandia in the Cretaceous (**Weaver et al., 1992; Pankhurst et al., 2000; Korhonen et al., 2010**). Plutonism on West Antarctica continued until the Cenozoic with a diachronous eastward cessation of subduction (**Larter and Barker, 1991; Leat et al., 1995; Larter et al., 2002; Cunningham et al., 2002; Mukasa and Dalziel, 2000**). This was followed and accompanied by the extrusion of the widespread Late Cenozoic alkali basalts (e.g. **Futa and LeMasurier, 1983; Hole and LeMasurier, 1994**), which crop out extensively in central West Antarctica, especially the Marie Byrd Land volcanic province (e.g. **LeMasurier and Rex, 1991**).

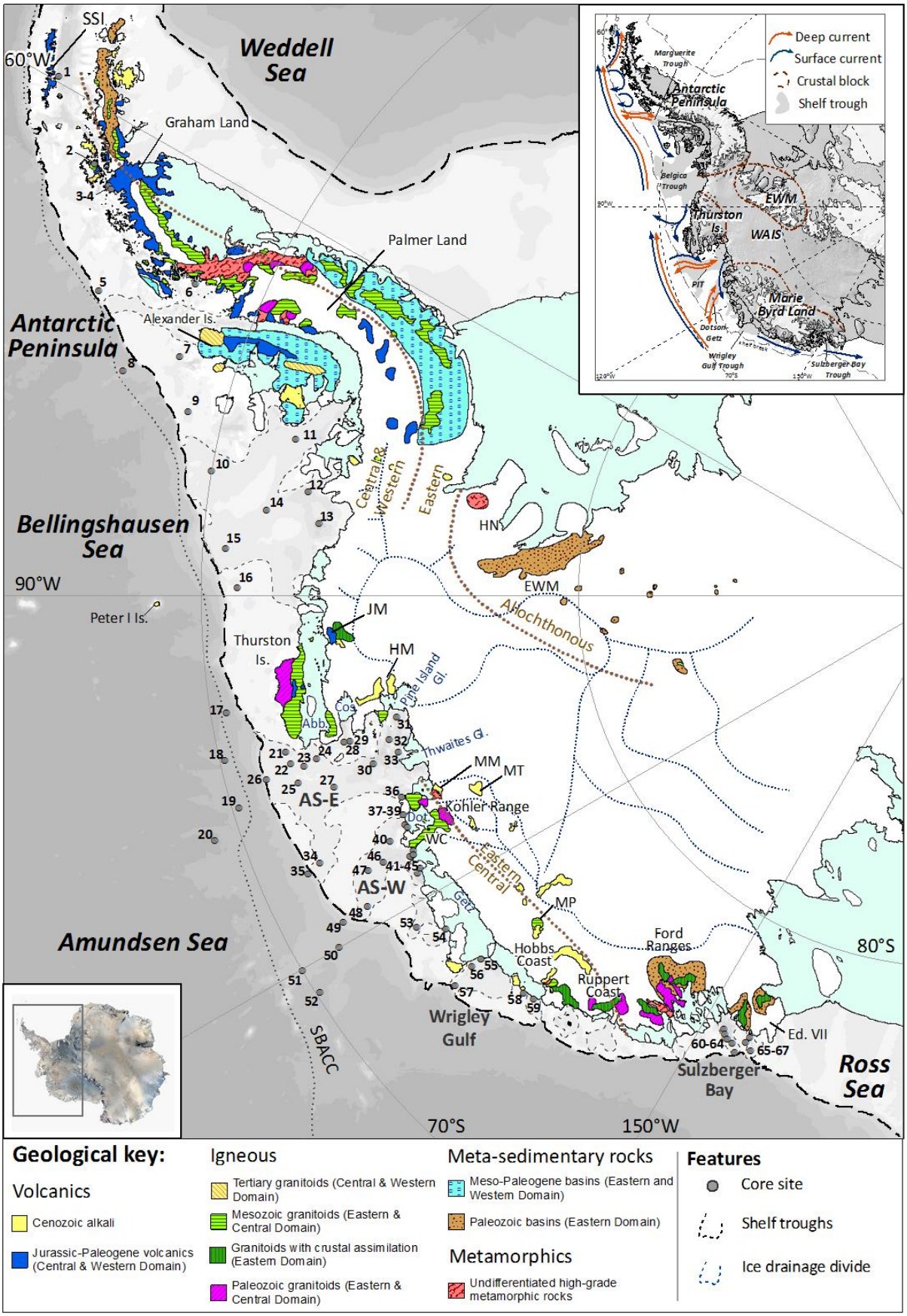

Figure 2: Simplified geological map of West Antarctica, including major geological units discussed in the text (Futa and LeMasurier, 1983; Storey et al., 1988; Pankhurst et al., 1993; McCarron and Smellie, 1998; Mukasa and Dalziel, 2000; Ferraccioli et al., 2002; Korhonen et al., 2010; Burton-Johnson and Riley., 2015). Thin blue dotted lines on the continent represent divides between major ice drainage basins, and brown dotted lines mark approximate boundaries between tectonic domains (Pankhurst et al., 1998; Vaughan and Storey, 2000). Grey dashed line on the continental shelf outlines bathymetric troughs, dashed black lines indicate the approximate location of the shelf break, and dotted line offshore marks position of the Southern Boundary of the Antarctic Circumpolar Current (SBACC; Orsi et al., 1995). Sites of surface sediments analysed in this study are shown as grey circles and numbers refer to their position in Table 1. Abbreviations: Abb – Abbot Ice Shelf; AS: Amundsen Sea; Cos – Cosgrove Ice Shelf; Dot – Dotson Ice Shelf; Ed. VII – Edward VII Peninsula: EWM – Ellsworth-Whitmore Mountains; FR – Ford Ranges; JM – Jones Mts; HN – Haag Nunataks; HM – Hudson Mts ; MM – Mt Murphy; MP – Mount Petras; MT – Mt Takahe; SSI – South Shetland Islands.; TI – Thurston Island; WAIS – West Antarctic Ice Sheet; WC – Walgreen Coast. Inset: Digital elevation model of Antarctica (Bamber et al., 2009) with major crustal blocks of West Antarctica (Dalziel and Elliot, 1982). White contours denote bedrock above modern sea-level (Fretwell et al., 2013). Blue arrows denote main surface ocean currents (Gladstone et al., 2001; Assmann et al., 2005; Murphy et al., 2013) and orange arrows denote deep (i.e. down to ca. 1000 m water depth) currents (Holland et al., 2010; Assmann et al., 2013; Murphy et al., 2013; Ha et al., 2014). Palaeo-ice streams are shown in grey.

2.2. Oceanography

The dominant oceanographic feature off (West) Antarctica is the eastward flowing Antarctic Circumpolar Current (ACC), which is driven by the West Wind Drift, creating a clockwise flow around the Antarctic continent (**Orsi et al., 1995; Sokolov and Rintoul, 2009**). In the eastern Pacific sector of West Antarctica the Southern Boundary of the ACC (SBACC) follows approximately the shelf break

(**Sokolov and Rintoul, 2009**), but the SBACC runs slightly north of it in the eastern Amundsen Sea and deviates further away from the continent towards the Ross Sea (**Orsi et al., 1995; Walker et al., 2013**) (**Fig. 2**). Wind stress and buoyancy forcing drive the westward flowing Antarctic Coastal Current, which spans the area between the SBACC and the coast (e.g. **Stammerjohn et al., 2015; Kim et al., 2016a),** creating a westward flowing surface current (**Fig. 2**). This general circulation pattern is complicated by local winds and large cyclonic gyres, such as in the Bellingshausen Sea (**Fig. 2**) and the Ross Sea. On the shelf of the Bellingshausen Sea, for instance, significant quantities of icebergs initially drift westwards with the coastal current but are then directed northwards near Thurston Island eventually joining the eastward flowing ACC (**Gladstone et al., 2001; Sokolov and Rintoul, 2009**). In the Pacific sector of the Southern Ocean, deep warm water upwells onto the continental shelf (**Fig. 2 inset**), locally protrudes towards the coast via bathymetric cross-shelf troughs, which were eroded by WAIS advances during past ice ages, and causes the bases of floating ice shelves to melt (e.g. **Walker et al., 2007; Thoma et al., 2008; Jenkins et al., 2010; Arneborg et al., 2012; Randall-Goodwin et al., 2015**). In the Amundsen Sea Embayment (ASE) the resulting glacial meltwater is detected in the mid-layer of the water column at about 400-500 m and flows northward along incised troughs towards the shelf break (e.g. **Kim et al., 2016b**).

The velocities of ocean currents measured and/or modelled in the surface and deep waters of our study area are on average ca. ≤5 cm/s, with a maximum of 22 cm/s (**Assmann et al. 2005; Wåhlin et al., 2010, 2012, 2013, 2016; Jacobs et al., 2011, 2013; Arneborg et al., 2012; Carvajal et al., 2013; Walker et al., 2013; Ducklow et al., 2015; Kim et al., 2015; Randall-Goodwin et al., 2015**). Exceptions to this are the westward flowing Antarctic Coastal Current in front of the Dotson Ice Shelf, and a local current within the Amundsen Polyna. The former current reaches a speed up to 40 cm/s in a narrow layer at 70 m water depth (**Kim et al., 2016a**), but this speed decreases to below 22 cm/s when integrated over the entire water column (**Randall-Goodwin et al., 2015**). The latter Amundsen Polynya current is characterized by a flow speed ≤27 cm/s detected at 430 m water

depth north of the Dotson and westernmost Getz ice shelves (**Kim et al., 2016a**). These velocities will become important when discussing transport pathways of detrital mineral grains later on.

3. Approach and samples

3.1. Approach to provenance fingerprinting

Analysis of the provenance of marine detrital sediments requires the consideration of a variety of glaciological and geological factors (see review by **Licht and Hemming, 2017**). Glacial influence on provenance records is exerted by preferential subglacial erosion of specific substrates. Glacial-marine transport and depositional processes in the ocean can furthermore introduce sorting and hence affect mineral assemblages in sediments. Geologically, onland bedrock needs to provide sufficient geochemical heterogeneity in order to produce distinct isotopic fingerprints. In addition, different rock types and mineral components are prone to be disproportionately represented in different grain-size fractions. Plutonic and high-grade metamorphic rocks, for instance, are rich in coarse-grained minerals, and are therefore likely to be over-represented in the coarse fraction of marine sediments. In contrast, sedimentary rocks consist of recycled continental material, and typically show a finer texture as well as depletion in minerals that are less resistant to chemical and physical weathering, such as hornblende and biotite (e.g. **Pierce et al., 2014**). Erosion of sedimentary rocks would lead to enrichment of these minerals in the fine fraction of glacial-marine sediments.

To limit the risk of neglecting or over-representing a particular rock type, we apply different geochemical tracers and analyse two different size-fractions of the same sediment sample. We investigate $^{40}Ar/^{39}Ar$ ages of ice-rafted (>150µm) hornblende and biotite grains, as well as Sr and Nd isotope and trace element compositions of fine-grained (<63µm) detritus. Dating of individual grains from marine sediments has been shown to provide powerful insights into the thermo-metamorphic history of the parent rocks. In the Southern Ocean, detailed studies on the provenance of East Antarctic glacial-marine sediments have shed light on previously documented as well as

undiscovered geological provinces below the ice (e.g. **Roy et al., 2007; Cook et al., 2014, 2017; Pierce et al., 2014, 2017**). Even though most studies so far have focused on $^{40}Ar/^{39}Ar$ analysis of hornblende grains, recent work has elegantly demonstrated how biotite can provide complementary information on source rock metamorphism (**Pierce et al., 2011, 2014**). Both minerals are major rock-forming constituents and are present in a variety of lithologies. The advantage of using the dual dating approach relies on the fact that different lithologies might contain different amounts of hornblende and biotite grains. Additionally, hornblende and biotite minerals have different closure temperatures for argon of ~550°C and ~300°C, respectively (**Harrison, 1982; Harrison et al., 1985**) and hence reflect different points on the cooling path following a major extrusive or tectono-metamorphic event. The distinct attributes between both chronometers can be exploited to extract information on the source rock, only if both minerals originate from the same source. In the marine environment, however, selective transport pathways may compromise such coupling. Critical factors to consider are ocean current speeds, which determine the grain sizes and types of detrital mineral grains being eroded, transported, or deposited and hydraulic equivalence (i.e settling behaviour) of the different mineral types, which determines preferential transport and deposition of one mineral grain type over another.

In order to overcome the potential bias created by using mineral tracers, which rely on the existence of rocks containing these minerals, we also chose to investigate Sr and Nd isotopic compositions and trace element geochemistry of fine-grained (<63µm) detritus. Fine-grained material can be eroded from any type of geology, and its radiogenic isotope composition depends on the age and lithology of the source formation (**Taylor and McLennan, 1995**). Hence, fine-grained Sr and Nd isotopic compositions have the potential to record an integrated signature of bedrock eroded under an ice stream or ice margin (**Hemming et al., 1998; Farmer et al., 2003, 2006; Colville et al., 2011; Pierce et al., 2011; Cook et al., 2013; 2017; Farmer and Licht, 2016**). Samarium (Sm) and Nd are not fractionated during continental erosion due to their nearly equal incorporation in most rock forming minerals. Neodymium model ages, based on the long-lived ^{147}Sm to ^{143}Nd decay

system, are thus effective at reconstructing the mantle extraction age of precursor material of sediments (**Goldstein and Hemming, 2003**). Different minerals tend to have very similar Sm/Nd ratios (e.g. **Bayon et al., 2009, Garçon et al., 2013, Rickli et al., 2014**), making it unlikely that Nd isotopic compositions in sediments are majorly influenced by sedimentary sorting and/or weathering. In contrast, comminution of minerals with variable Rb/Sr ratios can produce grain-size effects in the $^{87}Sr/^{86}Sr$ ratio, particularly due to the enrichment of clay minerals and biotite in the fine-grained fraction (e.g. **Eisenhauer et al., 1999; Goldstein and Hemming, 2003)**. Additionally, $^{87}Sr/^{86}Sr$ ratios can be fractionated during continental weathering due to the different solubility of the parent isotope ^{87}Rb compared to the daughter isotope ^{87}Sr (e.g. **Blum and Erel, 1997**).

3.2. Samples and site selection

For this study, we selected 67 proximal to distal seafloor surface sediment samples from the Pacific margin of West Antarctica. In total, 59 samples were provided from core repositories of the British Antarctic Survey (Cambridge), the Alfred-Wegener Institute for Polar and Marine Research (Bremerhaven), and the Antarctic Marine Geology Research Facility at the Florida State University (formerly at Tallahassee, FL). We additionally complemented our sample selection by eight samples previously studied by **Roy et al. (2007)**, which we picked for $^{40}Ar/^{39}Ar$ age analysis of biotite grains, not carried out in the original study. **Table 1** provides a full description of the site locations and water depths, coring devices, and sample depths. Sites proximal to individual major ice streams were selected to identify the geochemical fingerprint of each ice drainage basin and therefore to constrain subglacial geology (**Fig. 2**). Distal sites were selected to test whether provenance signatures from the terminus of an active ice stream can be traced offshore, with the future goal to reconstruct ice history through time by analysing down-core records. Most sampling sites are located in the ASE, the modern-day locus of major ice stream retreat (e.g. **Rignot et al., 2008, 2014**), and proposed site of substantial WAIS retreat in the past (e.g. **Vaughan et al., 2011**).

Most sediment samples used in this study are seafloor surface samples collected with box and multiple corers, and thus are of modern or at least Late Holocene age, which has been confirmed by AMS ^{14}C dating and/or ^{210}Pb analyses for several of these samples (**Hillenbrand et al., 2010a,b, 2013; Smith et al., 2011, 2014**). Other samples were chosen solely due to their geographical position. Even though no chronological constraints were available for some of those samples, e.g. shelf samples from Sulzberger Bay, the stratigraphic position of these samples near the seafloor surface assures that they are most likely not older than Late Holocene, which is evident from AMS ^{14}C ages of such samples in the Bellingshausen, Amundsen and Ross Seas and on the western Antarctic Peninsula margin (**The RAISED Consortium, 2014**). We followed this approach to avoid the potential influence of past changes in erosion or sediment transport/deposition on the provenance of the studied sediments.

As detailed in section 2, current speeds in the study area are typically ≤22 cm/s. This flow velocity is too low to move sand particles (≥63μm), which would require current speeds exceeding 26-29 cm/s (e.g. **McCave et al., 2017**). Large sheeted (flaky) biotite grains have a hydraulic equivalence to smaller (bulky) hornblende grains according to **Komar et al. (1984)** and **Garzanti et al. (2008, 2009**). These studies concluded that coarse grained (>150μm) biotite grains are hydraulically equivalent to quartz grains with a size exceeding ~75μm. Such grains would not be moved by the ocean currents typical for the West Antarctic margin, allowing interpretation of biotite grains >150μm as subglacial debris, which was released by grounded ice directly at the coast or transported by icebergs further offshore, alongside hornblende grains >150μm. Several samples, however, have been picked for hornblende and biotite grains from the 63 – 150μm fraction due to a low amount of grains in these samples. Due to the weak ocean currents in the study area, bulky hornblende grains from the 63 – 150μm fraction are likely unaffected by hydrodynamic sorting and provide the same lithologic information as the coarser >150μm size fraction. Sediment samples from sites 13 and 41 (**Table 1, Fig. 2**) were, however, picked for biotite grains from the 63 – 150μm

fraction only. These results will hence be discussed separately (i.e. potential for selective mineral transport by ocean currents).

Table 1: 39Ar/40Ar ages analysed in ice-rafted (>150 µm or >63 µm) hornblende and biotite grains from surface sediments off West Antarctica

Core Site	Site location	Core depth (cm)	Sector [a]	Size fraction	Gear	Latitude	Longitude	Water depth (m)	Hornblende grains	Biotite grains	Reference [b]
1	DF86-48	28-34	AP		piston corer	-62.68	-59.74	1234			
2	DF85-53	39-44	AP	>150 µm	piston corer	-64.56	-63.16	201	**55**		this study
3	PD88-111 Grab37	Surface	AP		surface grab	-65.14	-63.97	240			
4	PD88-111 Grab41	Surface	AP		surface grab	-65.23	-64.09	200			
5	ELT05-22	4-6	AP	>150 µm	piston corer	-65.95	-70.25	373	**91**	**7**	Roy et al., 2007; this study
6	DF85-82	28-33	AP	>150 µm	piston corer	-68.24	-67.50	275	**39**		this study
7	PS2524-1	0-1	AP		box corer	-68.49	-72.72	458			
8	ELT05-20	2-4	AP	>150 µm	trigger core	-67.18	-74.78	2926	**37**	**7**	Roy et al., 2007; this study
9	BC470	0-2	BS		box corer	-69.09	-76.39	670			
10	ELT42-09	0-2	BS	>150 µm	piston corer	-69.99	-80.39	567	**30**	**19**	Roy et al., 2007; this study
11	BC361	0-1	BS	>150 µm	box corer	-71.99	-76.55	633	**38**	**38**	this study
12	GC362	0-1	BS		box corer	-72.60	-80.83	846			
13	BC364	0-1	BS	63µm-	box corer	-72.	-83.	1010	*n.m.*	**20**	this study

				2mm		98	44				
14	BC369	0-2	BS	150µm-2mm	box corer	-71.58	-82.86	587	**47**	**44**	this study
15	BC459	0-1	BS	>150 µm	box corer	-70.61	-86.25	676	**61**	**46**	this study
16	PS2543-3	0-1	BS		multi-corer	-70.95	-89.36	537			
17	ELT11-19	0-2	AS-E	>150 µm	trigger corer	-70.42	-99.25	3808	**63**	**16**	Roy et al., 2007; this study
18	ELT11-18	2-4	AS-E	>150 µm	piston corer	-70.14	-102.82	3786	**24**	**5**	Roy et al., 2007; this study
19	ELT11-17	2-4	AS-E	>150 µm	trigger corer	-70.17	-106.64	3456	**6**	**5**	Roy et al., 2007; this study
20	PS58/254-2	0-2	AS-E	>150 µm	multi-corer	-69.31	-108.45	4016	**14**	**7**	this study
21	PS75/192-2	0-1	AS-E		giant box corer	-71.74	-103.33	793			
22	PS69/255-3	0-1	AS-E	150µm-2mm	giant box corer	-71.80	-104.36	654	**31**		this study
23	PS69/251-1	0-1	AS-E		giant box corer	-72.11	-104.81	573			
24	DF85-109	11-17	AS-E	>150 µm	piston corer	-72.49	-104.48	567	**30**		this study
25	BC451	0-1	AS-E	150µm-2mm	box corer	-71.87	-106.04	568	**49**	**51**	this study
26	BC455	0-1	AS-E	>150 µm	box corer	-71.07	-105.08	807	**54**	**44**	this study
27	BC485	0-3	AS-E	150µm-2mm	box corer	-72.73	-107.29	692	**15**	**26**	this study
28	DF85 96-1	83-88	AS-E	>150 µm	piston corer	-73.30	-103.62	786	**30**	*n.m.*	this study
29	PS69/299-1	0-1	AS-E	150µm-2mm	giant box corer	-73.44	-103.65	718	**24**	**57**	this study
30	BC482	0-2	AS-E		box corer	-73.	-106	1113			

						89	.27				
31	BC476	0-2	AS-E		box corer	-74.48	-104.42	1120			
32	PS75/159-1	0-1	AS-E	63µm-2mm	gravity corer	-74.80	-102.36	1046	**1**	*n.m.*	this study
33	PS75/168-1	0-1	AS-E	63µm-2mm	gravity corer	-74.61	-105.87	652	**9**	*n.m.*	this study
34	BC442	0-1	AS-E	150µm-2mm	box corer	-71.68	-113.01	608	**47**	**53**	this study
35	BC443	0-1	AS-E	150µm-2mm	box corer	-71.28	-113.46	1789	**55**	**39**	this study
36	PS69/281-3	0-1	AS-W		giant box corer	-74.33	-110.21	213			
37	NBP07-02 SMG6	Surface	AS-W		surface grab	-74.21	-111.90	343			
38	BC420	0-2	AS-W	>150 µm	box corer	-74.14	-112.86	806	**24**	**15**	this study
39	NBP00-01 KC24	13-19	AS-W		kasten corer	-74.17	-113.18	301			
40	BC421	0-1	AS-W	>150 µm	box corer	-73.62	-113.71	833	**32**	**21**	this study
41	BC412	0-1	AS-W	63µm-2mm	box corer	-73.92	-115.86	1128	**19**	**33**	this study
42	NBP00-01 PC22	5-10	AS-W		piston corer	-74.06	-115.46	1171			
43	NBP00-01 KC21	5-10	AS-W	>150 µm	kasten corer	-74.03	-115.84	1049	**35**		this study
44	NBP07-02 SMG5	Surface	AS-W		surface grab	-74.02	-117.30	350			
45	PS69/275-2	0-1	AS-W	>150 µm	giant box corer	-73.89	-117.55	1517	**11**	**37**	this study
46	BC407	0-2	AS-W	>150 µm	box corer	-73.21	-115.24	815	**6**	**18**	this study
47	PS69/283-5	0-1	AS-W	150µm-	giant box	-72.	-115	612	**52**	**44**	this study

				2mm	corer	76	.38				
48	BC431	0-1	AS-W	>150 µm	box corer	-72.30	-118.16	512	**45**	**42**	this study
49	BC433	0-1	AS-W	150µm-2mm	box corer	-71.56	-118.31	1722	**43**	**41**	this study
50	BC492	0-1	AS-W	>150 µm	box corer	-71.15	-119.96	2073	*n.m.*	**26**	this study
51	ELT33-12	2-6	AS-W	>150 µm	piston corer	-70.00	-120.17	2615	**27**	**18**	Roy et al., 2007; this study
52	ELT33-11	0-2	AS-W	>63µm	piston corer	-70.10	-122.26	3639	**10**		Roy et al., 2007
53	PS2545-1	0-1	AS-W		giant box corer	-73.16	-121.95	636			
54	NBP00-01 KC17	7-13	AS-W		kasten corer	-73.79	-123.53	891			
55	NBP99-02 PC21	8-13	WH	>150 µm	piston corer	-74.08	-127.79	702	**9**	**5**	this study
56	NBP99-02 TC23	0-3	WH		trigger weight corer	-73.78	-127.86	726			
57	NBP00-01 PC14	1-3	WH	>150 µm	piston corer	-73.11	-128.32	591	**51**		this study
58	PS75/133-1	0-1	WH	>150 µm	giant box corer	-74.34	-133.08	474	**19**	**40**	this study
59	PS75/130-2	0-1	WH	>150 µm	giant box corer	-74.45	-134.15	793	**22**	**40**	this study
60	DF83-III BC28	2-4	SB	>63µm	box corer	-76.83	-152.48	1024	**18**		this study
61	NBP96-01 PC12	0-3	SB		(giant) piston corer	-76.74	-152.85	881			
62	NBP96-01 TC13	0-3	SB		trigger weight corer	-76.65	-153.36	739			
63	NBP99-02 Grab20	Surface	SB		surface grab	-76.41	-154.82	458			
64	DF83 PC31	0-3	SB	>63µm	piston corer	-76.	-154	713	**5**		this study

						60	.10				
65	DF83-III BC26A	1-3	SB	>63µm	box corer	-76.95	-155.62	1353	**3**	*n.m.*	this study
66	NBP96-01 JTC11	0-3	SB		trigger weight corer	-76.78	-155.44	392			
67	DF83-III BC33	3.5-5.5	SB		box corer	-76.63	-156.40	770			

a) AP: Antarctic Peninsula sector, BS: Bellingshausen Sea, AS-E: eastern Amundsen Sea, AS-W: western Amundsen Sea, WH: Wrigley Gulf-Hobbs Coast, SB: Sulzberger Bay

b) See Appendix S1 for complete dataset

4. Analytical procedures

Sediment samples were freeze-dried, weighed, and wet sieved through a 63-micron sieve. The sand fraction (>63µm) was subsequently dry sieved at 150µm to obtain the >150µm fraction (**Table 1**). The fine-grained (<63µm) fraction was separated by gravitational settling, after which the clear supernatant was discarded, and sediment was dried in an oven at 60°C. Approximately 1g of <63µm sediment was leached with buffered acetic acid to remove calcium carbonate, followed by 0.02M hydroxylamine hydrochloride solution to extract Fe-Mn oxyhydroxide coatings (**Rutberg et al., 2000)**. Finally, the dried residue from leaching was thoroughly homogenised using an agate mortar.

Hornblende and biotite grains were hand-picked from the coarse (>150µm) fraction for $^{40}Ar/^{39}Ar$ age analysis on 43 of the 67 samples. Picking was extended to include the >63µm fraction only if too few grains were available in the >150µm fraction. Eight samples were exclusively picked from the 63 – 150µm fraction, of which seven were picked for hornblende grains and two for biotite grains (**Table 1; Appendix S1**). Fresh (i.e. glassy or black) grains were hand-picked from the coarse fraction with weathering being relatively minor or negligible (see also **Licht and Hemming, 2017**). Single grains and monitor standards (Fish Canyon sanidine) were irradiated at the USGS reactor in Denver, CO. Calibration for the neutron flux was based on J-values calculated to normalize Fish Canyon sanidine ages to 28.201+/- 0.046 Ma (**Kuiper et al., 2008**). $^{40}Ar/^{39}Ar$ ages were calculated from measurements of gas released using a single-step CO_2 laser fusion at the Argon Geochronology for the Earth Sciences (AGES) laboratory at Lamont-Doherty Earth Observatory. Argon isotope ratios were corrected for atmospheric argon ($^{40}Ar/^{36}Ar$ = 298.6, **Lee et al., 2006**), procedural blanks and mass discrimination from frequent measurements of blanks and air pipettes. Nuclear interference corrections were made based on the values reported by **Dalrymple et al. (1981)**.

Radiogenic isotope (Sr, Nd) and trace element analyses were carried out on two separate aliquots (~50mg) from the residual and leached (i.e. detrital) <63µm sediment fraction. Aliquots

were weighed into pre-cleaned Savillex vials and dissolved in a mixture of HF (2ml), HNO_3 (1ml) and $HClO_4$ (0.8ml) for three to four days on a hotplate until no visible particles remained. After digestion, one set of aliquots were dried and taken up in acid for the three-stage ion exchange chromatography in preparation for Sr and Nd isotope analysis. The Sr fraction was extracted from the sample matrix using Eichrom's Sr Spec resin in HNO_3 medium (similar to **Hemming et al., 2007**, modified from **Pin and Bassin, 1992**). The sample matrix was collected from this step and rare earth elements (REEs) were subsequently separated from the sample matrix using a cation exchange resin (AG50W-X8) in HCl medium (following the specific method of **Struve et al., 2016**). The Nd fraction was subsequently separated from the other REEs using Ln-Spec resin in HCl medium (modified after **Pin and Zalduegui, 1997**).

Dried Sr cuts were re-dissolved in 6M HCl, loaded as 1µl aliquots on degassed tungsten filaments, and covered by 1µl of $TaCl_5$ activator solution. Strontium isotopes were measured using a Trition Thermal Ionisation Mass Spectrometer (TIMS) in the Mass Spectrometry and Isotope Geochemistry laboratories at Imperial College London (MAGIC). Measured $^{87}Sr/^{86}Sr$ ratios were corrected for mass bias using an exponential law and assuming a $^{88}Sr/^{86}Sr$ ratio of 8.375. Repeated SRM987 standard measurements over the duration of three months yielded an $^{87}Sr/^{86}Sr$ ratio of 0.710261 ± 13 (2 S.D., n=31), in agreement with the published value for SRM987 of 0.710252 ± 13 (2 S.D., n=88; **Weis et al., 2006**). Strontium blanks were typically below 200pg (n=5), except for one batch that yielded a blank of 460pg Sr.

Neodymium isotope ratios were analysed on a Nu Plasma HR MC-ICP-MS in the MAGIC laboratories. Neodymium isotope ratios were corrected for instrumental mass bias using a $^{146}Nd/^{144}Nd$ ratio of 0.7219 and an exponential law. Measured $^{143}Nd/^{144}Nd$ ratios for all samples are reported after correcting for the average JNdi $^{143}Nd/^{144}Nd$ ratio of the session to the accepted value of 0.512115 (**Tanaka et al., 2000**). Blanks for the Nd procedure were typically below 10 pg (n=3) but always below 40 pg (n=1). Repeat measurements of the USGS BCR-2 standard over multiple runs

during the course of this study yielded $^{143}Nd/^{144}Nd$ ratios of 0.512637 ± 14 (2 S.D., n=43) and $^{87}Sr/^{86}Sr$ ratios of 0.705011 ± 13 (2 S.D., n=12), in agreement with published values of by **Weis et al. (2006)**.

Aliquots for trace element analysis were dried and transported to the Open University in Milton Keynes, and made up to a 1000-fold dilution of the original sample weight with MQ H_2O, such that the final solutions were in a 0.45 M HNO_3 matrix. Trace element analyses were conducted at the Open University, using an Agilent 8800 ICP-QQQ. The ICP-QQQ has a collision / reaction (ORS) cell, which allows for targeted removal of interference ions. Most elements reported here are measured using no gas (if interferences are not an issue) or He gas in the collision reaction cell, with the exception of the REE, which were measured in mass shift mode, using O_2 in the cell. Analyses were calibrated against five USGS reference materials (BIR-1, W-2, DNC-1, BHVO-2, AGV-1) at the start of each measurement session. An internal standard was added on line to monitor and correct for instrument drift. In addition, a monitor block, consisting of the reference material BCR-2, a repeated unknown, and a nitric solution, was run every five to seven unknowns, to assess the drift correction and monitor the precision and accuracy of analyses. Oxide formation (measured as CeO^+ / Ce^+) was kept low at <1.0% in no gas, or <0.6% in He gas mode, and doubly charged species (Ce^{++} / Ce^+) at <1.5% and <1.0%, respectively. Detection limits of trace elements were typically 2–50ppt in solution for light elements and ≤2ppt for mid to heavy elements (Rb – U). Overall, precision on repeated BCR-2 standard measurements (n=12) was usually below 5%, while accuracy checks were below 10% (except for Ti at 18%).

5. Results

5.1. $^{40}Ar/^{39}Ar$ ages of individual hornblende and biotite grains

$^{40}Ar/^{39}Ar$ ages for 1281 hornblende and 864 biotite grains are reported in **Table 1** and **Appendix S1** and illustrated in **Figure 3** for each geographical sector. From east to west, the sectors are: Antarctic Peninsula (AP sector, 60-75°W), Bellingshausen Sea (BS sector, 75-90°W), Amundsen Sea (AS sector,

90-125°W), Wrigley Gulf-Hobbs Coast (WH sector, 125-150°W) and Sulzberger Bay (SB sector, 150-160°W). Our results include 178 hornblende $^{40}Ar/^{39}Ar$ ages previously reported by **Roy et al. (2007**).

Antarctic Peninsula (AP, 60-75°W, core sites 1-8)

In the AP sector we find a continuous hornblende $^{40}Ar/^{39}Ar$ age spectrum from 0 to ~320 Ma with three major peaks at 14 Ma, 55 Ma and ~90 Ma, and some scattered older grains of ~480-1000 Ma and ~1600-2000 Ma (n=222; **Fig. 3a**). Significantly fewer biotite grains (n=14) were analysed for $^{40}Ar/^{39}Ar$ ages (**Table 1**). Three minor age clusters occur in the 23–83 Ma age interval, with three peak ages of ~27 Ma, ~50 Ma and ~77 Ma (**Fig. 3b**). Two single grains record ages of 360-380 Ma.

Bellingshausen Sea (BS, 75-90°W, core sites 9-16)

In the BS sector a continuous hornblende $^{40}Ar/^{39}Ar$ age spectrum spans from 0–260 Ma, but with a dominant cluster between ~75 and 140 Ma, a peak of ~110 Ma, and one older grain at 510 Ma (n=176; **Fig. 3c**). Biotite $^{40}Ar/^{39}Ar$ ages (n=167) yield a similar age range, predominantly from 0 to ~280 Ma, with the majority of grain ages in the interval between 75 and 135 Ma, and with peaks at ~99 Ma and ~108 Ma. One older grain dates back to 480 Ma (**Fig. 3d**). The finer sand size-fraction (63 − 150µm) of site 13 was picked for biotite grains, and hence the $^{40}Ar/^{39}Ar$ ages for this sample could be influenced by ocean current transport because biotite grains of this size can be affected by relatively weak ocean currents with flow speeds as observed in the Bellingshausen Sea. However, age distribution observed at site 13 shows no pattern deviating from that of other core samples in the BS sector, with the majority of the ages ranging from 94-120 Ma (**Table S1**).

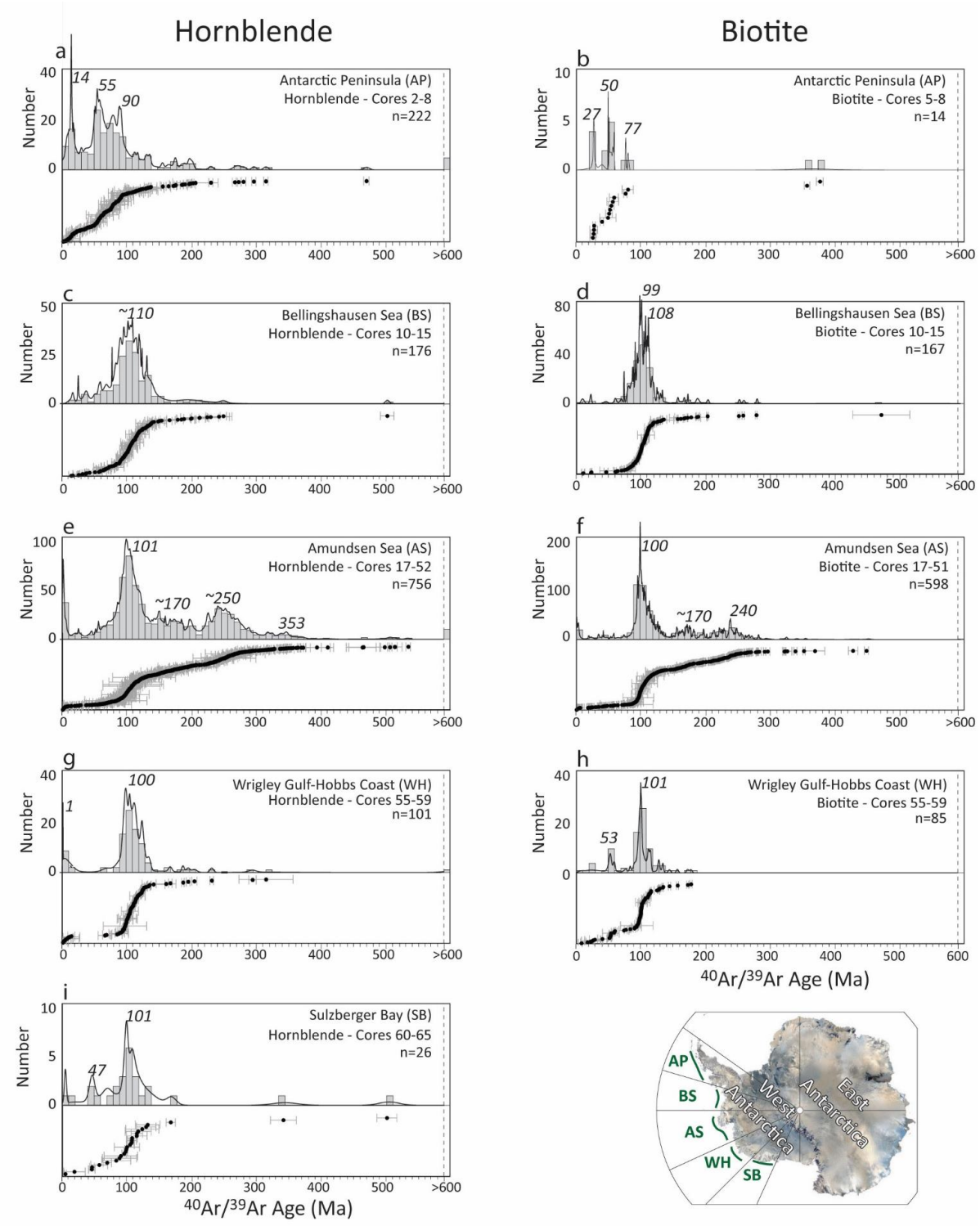

Figure 3: $^{40}Ar/^{39}Ar$ ages of hornblende and biotite grains from five sectors off the Pacific margin of West Antarctica. Histograms are produced using 10 Ma as bin intervals. Probability density plots (ISOPLOT4.15; Ludwig et al., 2003) are superimposed, and individual ages are shown with

uncertainties in the lower panel. Results include previously analysed $^{40}Ar/^{39}Ar$ ages of hornblende grains from Roy et al. (2007) (see Table 1).

Amundsen Sea (AS, 90-125°W, core sites 17-54)

The AS sector is the main focus of this study and a total of 756 hornblende grains and 598 biotite grain ages are reported for this sector. A continuous hornblende $^{40}Ar/^{39}Ar$ age spectrum from 0 to ~380 Ma shows two noticeable peaks at ~101 Ma and ~250 Ma. A significant number of grains with ages ranging from 140 to ~210 Ma are found, which are notably absent from the other sectors. A minor age peak is observed at ~353 Ma. Though significantly smaller in number, older hornblende grains also appear in these sediments (n=20), with age clusters of 400-550 Ma, 640-800 Ma, 1120-1360 Ma, 1700-1850 Ma and 2600-2800 Ma (**Fig. 3e, Appendix S1**). Biotite $^{40}Ar/^{39}Ar$ ages (n=598) spread from 0 to ~300 Ma, with a prominent peak at ~100 Ma, and secondary peaks at ~170 and 240 Ma. Nine older grains yield ages of ~330-375 Ma, ~450 and 890 Ma (**Fig. 3f**). The apparent modern (~0 Ma) age peaks observed in both minerals in the AS sector seem suspicious as the corresponding grains were primarily picked from core 49 situated on the upper continental slope, and are not detected in other sectors (**Fig. 2**). Biotite grains from site 41 were picked from a smaller size-fraction (**Table 2**) and hence could potentially be influenced by ocean current transport due to fast flow speeds detected off the Dotson Ice Shelf (**Kim et al., 2016a**). However, $^{40}Ar/^{39}Ar$ ages from this sample do not reveal any pattern deviating from that of $^{40}Ar/^{39}Ar$ ages in nearby core samples (**Table S1**). We hence consider differential sorting of biotite and hornblende mineral grains of the same size fraction to be negligible in our study area.

Wrigley Gulf-Hobbs Coast (WH, 125-150°W, core sites 55-59)

A total of 101 hornblende ages obtained from the WH sector record well defined $^{40}Ar/^{39}Ar$ ages with populations around 0-20 Ma and 65-140 Ma, and age probability peaks at ~0 Ma and ~100 Ma as

well as three scattered ages of ~210 Ma, 300 Ma and 610 Ma (**Fig. 3g**). Biotite $^{40}Ar/^{39}Ar$ ages (n= 85) cover a similar age range from 0 to ~150 Ma, with some scattered ages of ~180 Ma, but the dominant age probability peak at 101 Ma is slightly older than the one defined by the hornblende grains. A second minor age peak is detected around ~53 Ma, which is absent in the hornblende age spectrum (**Fig. 3h**).

Sulzberger Bay (SB, 150-160°W, cores 60-67)

Most hornblende $^{40}Ar/^{39}Ar$ ages (n= 26) from the SB sector range from 0 to ~135 Ma, and show a well-defined age probability peak at ~100 Ma. Minor age peaks occur at ~48 Ma and ~5 Ma and three individual grains yield ages of ~170 Ma, 350 Ma and 510 Ma (**Fig. 3i**). No biotite grains were picked/analysed from this sector.

5.2. Neodymium and strontium isotope composition of fine-grained detrital sediments

In total, 66 and 54 samples were analysed for their detrital Nd and Sr isotopic composition respectively. The Nd isotope results are expressed as epsilon values (ε_{Nd}), which denotes the deviation from a chondritic value of 0.512638 in parts per 10,000 (**Jacobsen and Wasserburg, 1980**). Neodymium and Sr isotope results from the study of **Roy et al. (2007)** on eight additional distal samples are included in the following results and subsequent discussion (**Table 2**).

Overall, detrital continental margin sediments off West Antarctica have Nd isotopic compositions ranging from -12 to +2 and $^{87}Sr/^{86}Sr$ ratios from 0.7493 to 0.7057 (**Fig. 4, Table 2**). The values are anti-correlated as expected from global trends, and are distinct for individual sectors. The highest Nd isotope values and the lowest Sr isotope ratios are found in the WH sector (ε_{Nd} = -0.5 to 1.3, $^{87}Sr/^{86}Sr$ = 0.7056 to 0.7061), in the westernmost sample from the AS sector (site 54; ε_{Nd} = 0.3) and in the easternmost samples from the AP sector (site 1 and 3-5: ε_{Nd} = 0.9 to 2.2; $^{87}Sr/^{86}Sr$ ~0.7053). The other end of the data range is defined by samples from SB, i.e. offshore from western

Marie Byrd Land **(Fig. 2**), with Nd isotopic compositions of -11.9 to -10.6 and $^{87}Sr/^{86}Sr$ = 0.7411 to 0.7493. Detrital shelf sediments from the AS sector reveal intermediate values, but with distinctly different values in the eastern and western AS. In the eastern AS, lower Nd and higher radiogenic Sr values (ε_{Nd} ~-7.3, $^{87}Sr/^{86}Sr$ ~ 0.7240) are found in a sample taken in front of Pine Island Glacier (site 32, **Table 2, Fig. 2**). Along the eastern flank of the AS sector the isotopic fingerprints of the samples change systematically northwards across the shelf to higher Nd and lower Sr isotopic compositions (site 20: ε_{Nd} ~-3.3, $^{87}Sr/^{86}Sr$ ~ 0.7079). A uniform signature is observed in the western AS sector, where shelf sediments yield Nd and Sr isotopic compositions of ε_{Nd} ~-2.9 to -1.7 and $^{87}Sr/^{86}Sr$ ~0.7082 to 0.7101 (n=17), except sample from site 39 proximal to Dotson Ice Shelf (ε_{Nd} = 0.4; $^{87}Sr/^{86}Sr$ was not measured) and site 51 on the lower continental slope (ε_{Nd} ~-5.5; $^{87}Sr/^{86}Sr$ = 0.7128). Detrital surface sediments from the BS extend from the values recorded in the western AS and on the eastern AS shelf towards lower Nd and higher Sr values, along a steeper slope (ε_{Nd} = -7.3 to -4.2, $^{87}Sr/^{86}Sr$ = 0.7097 to 0.7132, n=8**; Fig. 4**). General anti-correlation of Nd and Sr isotopes in fine-grained detrital sediments off West Antarctica, in addition to the extremely uniform values observed in the western AS from ice proximal to ice distal (ocean) locations, indicate that both isotope systematics are predominantly governed by provenance and not by sedimentary sorting or weathering.

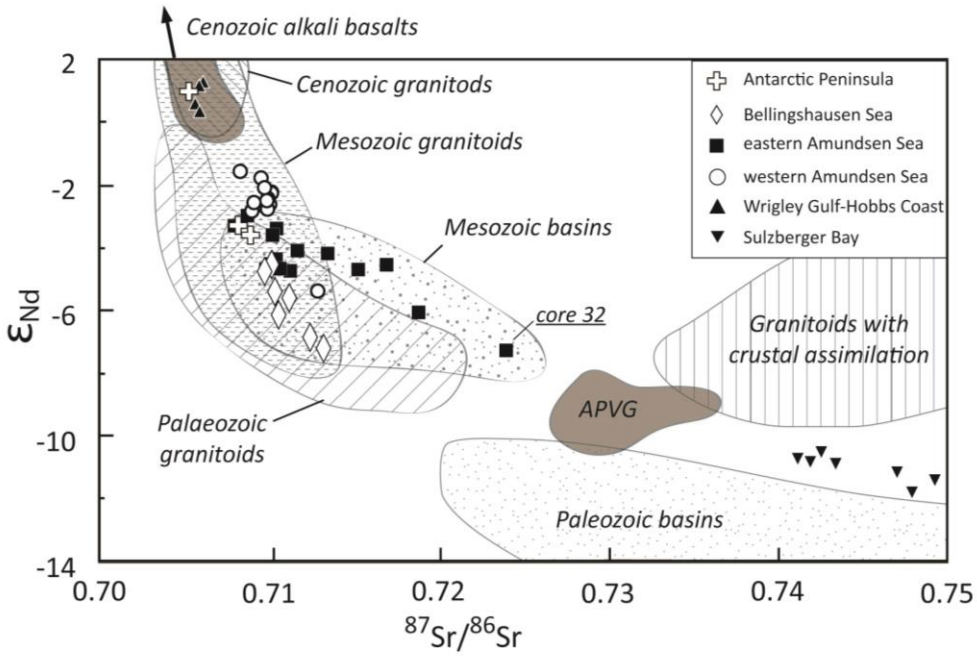

Figure 4: Neodymium and strontium isotopic compositions of detrital surface sediments along the Pacific margin of West Antarctica. Marine sediment data are displayed as symbols according to geographical sectors defined in Table 1 (only samples where both Nd and Sr isotope ratios were measured are shown). Isotopic compositions of major bedrock outcrops on land are compiled from the literature (see Appendix S2) and correspond to the units displayed in Fig. 2 (Note: For simplicity data from high-grade metamorphic rocks are not displayed). APVG = Antarctic Peninsula Volcanic Group.

Table 2: Sr and Nd isotope compositions of the detrital fraction (<63µm) and clay mineral assemblages (<2µm) of surface sediments off West Antarctica

Core Site	Site location	Sector [a]	$^{87}Rb/^{86}Sr$ [b]	$^{87}Sr/^{86}Sr$ (±2 S.E.)	$^{147}Sm/^{144}Nd$ [b]	$^{143}Nd/^{144}Nd$ (±2 S.E.)	ε_{Nd} [d]	± 2 S.D. [c]	T_{DM} (Ma) [d]	Ref. [e]	Ill (%)	Sme (%)	Kln (%)	Chl (%)	Ref. [e]
1	DF86-48*	AP				0.512751 ± 8	2.20	0.36							
2	DF85-53	AP													
3	PD88-111 Grab37*	AP				0.512725 ± 9	1.69	0.36							
4	PD88-111 Grab41*	AP				0.512719 ± 9	1.57	0.36							
5	ELT05-22	AP		0.705281 ± 5	0.1366	0.512685 ± 10	0.92		920	2, 3					
6	DF85-82	AP													
7	ELT05-20	AP		0.708198 ± 7	0.1341	0.512469 ± 18	-3.30		1304	2, 3					
8	PS2524-1	AP	1.423	0.708926 ± 5	0.1179	0.512453 ± 8	-3.61	0.21	1109	1	58	8	0	34	4
9	BC470	BS	1.628	0.710100 ± 4	0.1179	0.512405 ± 8	-4.55	0.28	1185	1					
10	ELT42-09	BS			0.1255	0.512420 ± 9	-4.25		1261	2					
11	BC361	BS	1.706	0.709714 ± 5	0.1160	0.512392 ± 16	-4.80	0.32	1183	1	44	20	5	31	5
12	GC362	BS	1.920	0.711165 ± 5	0.1173	0.512349 ± 6	-5.6	0.29	1267	1	52	19	6	23	5

							4								
13	BC364	BS	1.846	0.713189 ± 5	0.1142	0.512267 ± 6	-7.24	0.30	1353	1	66	7	2	25	5
14	BC369	BS	1.547	0.710320 ± 4	0.1152	0.512359 ± 9	-5.44	0.24	1224	1	46	20	3	30	5
15	BC459	BS	1.399	0.710539 ± 4	0.1136	0.512321 ± 10	-6.18	0.28	1262	1	52	16	6	26	6 (GC372)
16	PS2543-3	BS	1.889	0.712397 ± 5	0.1123	0.512285 ± 7	-6.89	0.21	1301	1	59	14	4	23	4
17	ELT11-19	AS-E		0.707928 ± 6	0.1271	0.512470 ± 10	-3.28		1197	2, 3					
18	ELT11-18	AS-E		0.709790 ± 5	0.1213	0.512399 ± 5	-4.66		1239	2, 3					
19	ELT11-17	AS-E		0.710616 ± 8	0.1257	0.512400 ± 16	-4.64		1299	2, 3					
20	PS58/254-2	AS-E	1.658	0.708704 ± 4	0.1185	0.512486 ± 6	-2.96	0.30	1064	1	33	38	12	17	7
21	PS75/192-2	AS-E	1.726	0.710162 ± 5	0.1127	0.512408 ± 8	-4.49	0.21	1121	1					
22	PS69/255-3	AS-E	1.541	0.709971 ± 5	0.1135	0.512402 ± 8	-4.61	0.24	1139	1	41	27	14	18	7
23	PS69/251-1	AS-E	2.041	0.711226 ± 6	0.1123	0.512396 ± 8	-4.71	0.21	1133	1	41	25	16	18	7
24	DF85-109	AS-E													
25	BC451	AS-E	2.255	0.711652 ± 5	0.1131	0.512429 ± 10	-4.07	0.28	1092	1	46	23	16	14	7

26	BC455	AS-E	1.703	0.710384 ± 5	0.1117	0.512415 ± 9	-4.34	0.28	1099	1	45	24	16	15	7
	repeat[f]			*0.710365 ± 5*		*0.512415 ± 7*	*-4.35*	*0.16*							
27	BC485	AS-E	2.789	0.713436 ± 4	0.1141	0.512425 ± 9	-4.16	0.28	1110	1	46	19	19	15	7
28	DF8596-1	AS-E													
29	PS69/299-1	AS-E	1.193	0.707947 ± 5	0.1118	0.512470 ± 8	-3.28	0.24	1018	1	41	26	7	25	7
30	BC482	AS-E	3.303	0.715235 ± 4	0.1118	0.512399 ± 9	-4.67	0.28	1125	1	44	19	23	15	7
31	BC476	AS-E	3.903	0.718795 ± 6	0.1116	0.512329 ± 10	-6.03	0.28	1226	1	52	16	17	16	7
32	PS75/159-1	AS-E	4.659	0.723959 ± 5	0.1100	0.512267 ± 8	-7.24	0.21	1299	1					
33	PS75/168-1	AS-E	3.557	0.716904 ± 6	0.1096	0.512406 ± 8	-4.52	0.21	1090	1	50	13	21	16	7 (PS69/292-3)
34	BC442	AS-E	1.946	0.710417 ± 4	0.1131	0.512465 ± 9	-3.37	0.28	1039	1	47	18	19	16	7
35	BC443	AS-E	1.712	0.710181 ± 5	0.1135	0.512454 ± 8	-3.58	0.28	1059	1	47	20	18	16	7
36	PS69/281-3	AS-W	2.058	0.709504 ± 6	0.1116	0.512542 ± 8	-1.87	0.28	909	1	42	14	29	15	7
37	NBP07-02*	AS-W				0.512512 ± 8	-2.46	0.32							
38	BC420	AS	2.0	0.710	0.11	0.5125	-	0.2	992	1	4	13	18	22	7

		-W	84	125 ± 5	67	19 ± 6	2.32	9			7				
39	NBP00-01 KC24*	AS-W				0.512660 ± 9	0.43	0.37							
40	BC421	AS-W	2.205	0.710011 ± 5	0.1124	0.512499 ± 8	-2.71	0.28	981	1	43	22	19	16	7
41	BC412	AS-W	2.109	0.709682 ± 5	0.1148	0.512496 ± 9	-2.76	0.28	1008	1	40	21	20	19	7
42	NBP00-01 PC22*	AS-W				0.512517 ± 10	-2.35	0.29							
43	NBP00-01 KC21*	AS-W				0.512495 ± 8	-2.79	0.29							
44	NBP07-02*	AS-W				0.512486 ± 8	-2.97	0.32							
45	PS69/275-2	AS-W	2.446	0.710115 ± 5	0.1144	0.512517 ± 8	-2.35	0.29	973	1	43	20	20	16	7
46	BC407	AS-W	2.275	0.709903 ± 4	0.1134	0.512509 ± 7	-2.52	0.24	975	1	43	18	22	18	7
	repeat			*0.710041 ± 5*		*0.512504 ± 9*	*-2.62*	*0.21*							
47	PS69/283-5	AS-W	2.180	0.709881 ± 4	0.1133	0.512492 ± 7	-2.86	0.20	1000	1	43	20	19	18	7
48	BC431	AS-W	1.746	0.708959 ± 4	0.1136	0.512488 ± 8	-2.92	0.28	1008	1	46	17	19	18	7
49	BC433	AS-W	1.848	0.709845 ± 4	0.1128	0.512505 ± 7	-2.59	0.28	976	1	43	17	21	18	7
50	BC492	AS	1.6	0.709	0.11	0.5125	-	0.2	954	1					

		-W	97	711 ± 5	4	26 ± 7	2.18	9							
51	ELT33-12	AS-W		0.712846 ± 6	0.1188	0.512358 ± 8	-5.46		1272	2, 3					
52	ELT33-11	AS-W		0.709086 ± 6	0.1187	0.512502 ± 10	-2.65		1040	2, 3					
53	PS2545-1	AS-W	1.809	0.708276 ± 7	0.1144	0.512553 ± 8	-1.66	0.21	918	1	39	28	23	10	4
54	NBP00-01 KC17*	WH				0.512653 ± 8	0.29	0.32							
55	NBP99-02 PC21*	WH				0.512610 ± 7	-0.54	0.32							
56	NBP99-02 TC23	WH	1.012	0.705656 ± 5	0.1156	0.512667 ± 10	0.57	0.24	752	1	37	27	20	17	1
57	NBP00-01 PC14	WH	1.045	0.705917 ± 4	0.1155	0.512654 ± 9	0.32	0.24	770	1	37	25	20	18	1
58	PS75/133-1	WH	1.081	0.706122 ± 4	0.1151	0.512703 ± 8	1.26	0.30	693	1	36	28	14	21	1
59	PS75/130-2	WH	0.891	0.705889 ± 4	0.1158	0.512697 ± 5	1.14	0.29	707	1					
60	DF83-III BC28	SB	7.142	0.741188 ± 4	0.1133	0.512085 ± 8	-10.79	0.24	1616	1					
61	NBP96-01 PC12	SB	7.492	0.743425 ± 4	0.1131	0.512077 ± 9	-10.95	0.24	1623	1					
62	NBP96-01 TC13	SB	8.265	0.747045 ± 5	0.1127	0.512063 ± 8	-11.22	0.24	1639	1					
63	NBP99-02	SB				0.512058 ± 7	-1	0.32							

	Grab20						1.31								
64	DF83PC31	SB	8.324	0.747928 ± 5	0.1129	0.512030 ± 8	-11.86	0.24	1691	1					
65	DF83-IIIBC26A	SB	8.010	0.742576 ± 4	0.1119	0.512096 ± 9	-10.58	0.24	1576	1					
66	NBP96-01JTC11	SB	8.224	0.749275 ± 4	0.1118	0.512050 ± 10	-11.47	0.24	1643	1					
	repeat			*0.749534 ± 6*		*0.512633 ± 8*	*-11.52*	*0.16*							
67	DF83-IIIBC33	SB	7.976	0.741931 ± 4	0.1128	0.512080 ± 8	-10.89	0.24	1616	1					

a) see Table 1

b) calculated from elemental compostion of the same sample (Table 3)

c) Standard deviation based on the reproducibility of the $^{143}Nd/^{144}Nd$ ratio of the JNdi standard during each run: 0.512224 ±14 (n=24), 0.512116 ±12 (n=17), 0.512144 ± 12 (n=13), 0.512157 ± 10 (n=12), 0.512106 ± 12 (n=32), 0.512149 ± 11 (n=27) and 0.512142 ± (n=16).

d) Nd model ages relative to present depleted mantle (DM) using a one-stage evolution model: $^{147}Sm/^{144}Nd$= 0.2136; $^{143}Nd/^{144}Nd$=0.51315

e) (1) this study; (2) Roy et al., 2007; (3) Hemming et al., 2007; (4) Hillenbrand et al., 2002; (5) Hillenbrand et al., 2009; (6) Hillenbrand et al., 2010; (7) Ehrmann et al., 2011

f) Repeat values represent full procedural replicats of sample powders (i.e. from digestion, through ion exchange chromatography, to mass spectrometry).

*) Samples denoted with a star were analysed at L-DEO for their Nd isotopic composition using similar methodologies to those described in the main text, but run on a AXIOM MC-ICP-MS (see van de Flierdt et al., 2008, for more details on methodology).

5.3. Trace element composition of fine-grained detrital sediments

Trace element compositions, including full REE patterns, were analysed on the <63μm fraction of 44 detrital seafloor sediment samples. The data are reported in **Table 3** and are illustrated in mid-ocean ridge basalt (MORB)-normalized spider diagrams (**Fig. 5**). Overall, detrital sediments show compositions comparable to Post-Archean Average Shale (PAAS) (**McLennan, 2001**). Some elements, however, deviate from PAAS. Zirconium (Zr) concentrations show considerable scatter (**Fig. 5**), while the elemental ratio of the two high-field strength elements Zr and yttrium (Y) are high in sediments from the WH sector (Zr/Y ~10.5) and low in sediments from the SB sector (Zr/Y ~4) as well as in sediments proximal to Pine Island and Thwaites glaciers (Zr/Y ~5). Similarly, high Sr over thorium (Th) ratios of 25 – 30 are observed in WH, at site 29 on the AS (Sr/Th ~25) and in the AP sector (site 8, Sr/Th ~27), with the latter sector being mostly characterized by very low thorium (**Table 3**). The ratio of Th over scandium (Sc), which generally describes the relative contribution of basic and felsic rocks (**Taylor and McLennan, 2001**), is elevated in the samples from sites 32 and 33 proximal to Pine Island and Thwaites glaciers (1.5-2.0), but low in WH (~0.8-1), sites 8 to 11 from the AP and BS sectors (0.6-0.8) and in one distal sample from site 20 in the AS sector (0.6). Europium anomalies are moderately negative (Eu/Eu* = 0.5-0.9) in most samples, and correlate well with Th/Sc (R^2= 0.67; **Fig. 6**) and Sr/Th ratios (R^2= 0.87) (**Table 3**).

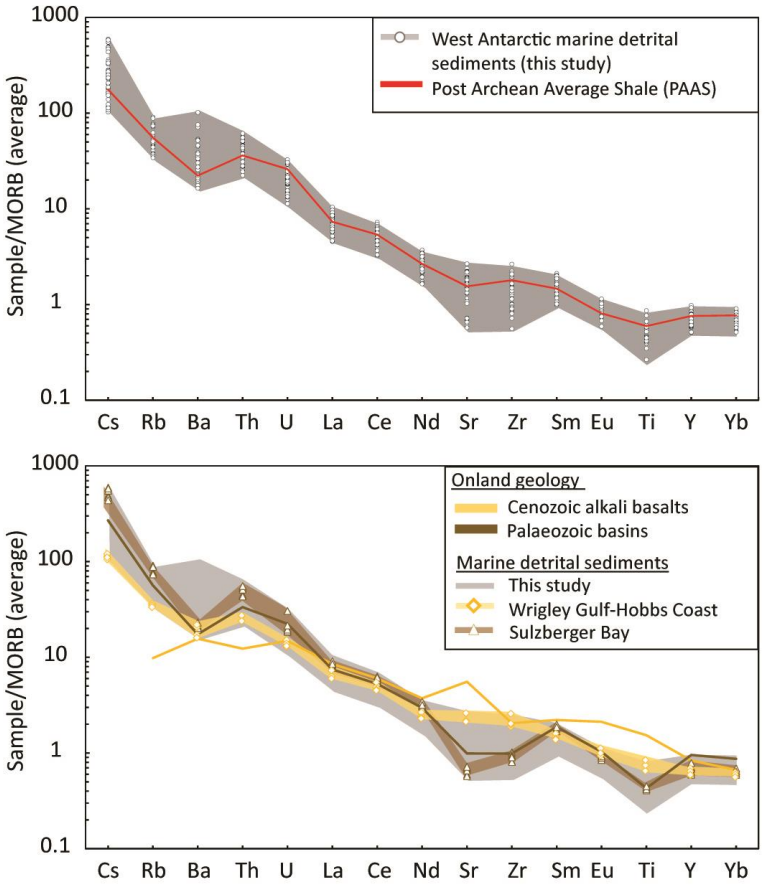

Figure 5: a) Trace element compositions of fine-grained (<63µm) detrital surface sediments along the Pacific margin of West Antarctica, normalized to average mid-ocean ridge basalts and arranged in order of incompatibility (Gale et al., 2013). Individual sample results are indicated by white circles in the upper graphs, while the red line denotes the composition of the Post-Archean Average Shale (PAAS, McLennan, 2001). The grey field denotes marine sediment samples from this study. b) Sediments from the Wrigley Gulf-Hobbs Coast sector are now shown as diamonds connected by a yellow line, and sediments from Sulzberger Bay are shown as triangles connected by a brown line. The grey field denotes samples from the Antarctic Peninsula (AP), Bellingshausen Sea (BS) and Amundsen Sea (AS) sectors. The patterns for these two groups are similar to onland results obtained for Late Cenozoic alkali basalts (yellow line; Futa and LeMasurier, 1983; Hart et al., 1997) and Palaeozoic meta-sedimentary rocks (brown line; Korhonen et al., 2010), respectively.

Table 3: Trace element composition of detrital <63µm surface sediments off West Antarctica (in ppm)

Table 3: Trace element composition of detrital <63µm surface sediments off West Antarctica (in ppm)

Core Site	Site location	Sector(a)	Li	Sc	Ti	V	Cr	Mn	Co	Ni	Cu	Zn	Rb	Sr	Y	Zr	Cs	Ba	La	Ce	Pr	Nd	Sm	Eu	Gd	Tb	Dy	Ho	Er	Yb	Lu	Hf	Pb	Th	U	Sr/Th	Sr/Zr	Zr/Y	Th/Sc	Ce/Ce*(b)	Eu/Eu*(b)
1	DF86-48	AP																																							
2	DF85-53	AP																																							
3	PD88-111 Grab37*	AP																																							
4	PD88-111 Grab41*	AP																																							
5	ELT05-22	AP																																							
6	DF85-82	AP																																							
7	ELT05-20	AP																																							
8	PS2524-1	AP	54	15	4123	108	50	661	12	21	34	137	**122**	**247**	21	84	5	634	22.8	50.6	5.4	**20.9**	**4.1**	0.9	3.5	0.6	3.3	0.7	2.1	1.9	0.3	2.2	11.4	9.0	1.7	27.35	2.95	3.98	0.60	1.05	0.77
9	BC470	BSE	47	14	3954	90	44	542	9	17	16	144	**120**	**213**	23	96	6	966	26.8	57.7	6.1	**23.6**	**4.6**	1.0	3.9	0.6	3.6	0.8	2.2	2.2	0.3	2.6	11.9	11.0	1.9	19.42	2.21	4.26	0.78	1.04	0.71
10	ELT42-09	BSE																																							
11	BC361	BSE	40	15	4115	94	43	612	11	18	23	131	**129**	**218**	22	98	6	883	27.5	59.7	6.0	**23.3**	**4.5**	1.0	3.8	0.6	3.5	0.7	2.1	2.2	0.3	2.8	18.0	11.7	1.8	18.61	2.22	4.45	0.80	1.06	0.73
12	GC362	BSE	40	14	4151	90	42	634	11	22	22	128	**146**	**220**	25	101	6	1131	31.0	65.0	6.7	**25.8**	**5.0**	1.1	4.2	0.7	3.9	0.8	2.3	2.4	0.4	2.7	20.3	13.3	1.9	16.52	2.19	4.01	0.92	1.03	0.70
13	BC364	BSE	19	8	2675	51	31	418	6	16	21	72	**108**	**169**	19	65	3	566	24.3	50.1	5.3	**20.1**	**3.8**	0.8	3.2	0.5	3.0	0.6	1.8	1.9	0.3	1.8	15.1	10.1	1.3	16.73	2.59	3.48	1.20	1.02	0.70
14	BC369	BSE	41	14	4329	85	40	596	10	19	23	125	**133**	**249**	24	108	6	1568	30.7	66.0	6.8	**26.1**	**5.0**	1.1	4.2	0.7	3.8	0.8	2.3	2.2	0.3	3.0	17.0	11.7	1.9	21.23	2.31	4.56	0.84	1.05	0.73
15	BC459	BSE	32	13	4300	74	37	523	8	13	19	95	**118**	**245**	25	116	5	1312	34.3	70.7	7.7	**29.0**	**5.5**	1.1	4.5	0.7	4.0	0.8	2.4	2.5	0.4	3.2	17.1	12.0	2.0	20.40	2.11	4.64	0.93	1.00	0.69
16	PS2543-3	BSE	33	11	3511	70	36	559	10	27	19	101	**148**	**226**	23	96	5	748	32.0	69.7	7.0	**26.8**	**5.0**	1.1	4.1	0.6	3.8	0.8	2.3	2.1	0.3	2.6	24.8	10.2	1.6	22.14	2.36	4.18	0.91	1.07	0.75
17	ELT11-19	ASE-E																																							
18	ELT11-18	ASE-E																																							
19	ELT11-17	ASE-E																																							
20	PS58/254-2	ASE-E	36	19	4528	90	51	546	11	25	105	125	**109**	**190**	19	146	5	646	23.0	52.8	5.2	**19.8**	**3.9**	0.8	3.2	0.5	3.0	0.6	1.8	1.9	0.3	3.4	20.1	10.5	1.5	18.03	1.30	7.71	0.56	1.11	0.72
21	PS75/192-2	ASE-E	38	12	4677	80	41	468	9	15	20	103	**137**	**231**	25	146	6	1025	35.5	76.3	7.8	**29.4**	**5.5**	1.1	4.5	0.7	4.0	0.8	2.4	2.4	0.4	3.7	18.1	13.5	2.2	17.13	1.58	5.83	1.11	1.06	0.69
22	PS69/255-3	ASE-E	38	13	4781	79	45	470	9	17	22	96	**140**	**263**	26	152	6	1343	34.9	76.8	8.1	**30.7**	**5.8**	1.1	4.7	0.7	4.2	0.9	2.6	2.5	0.4	4.2	19.4	14.1	2.4	18.63	1.72	5.90	1.12	1.05	0.67
23	PS69/251-1	ASE-E	39	12	4759	79	41	479	9	16	20	103	**148**	**209**	28	163	7	727	38.4	82.3	8.4	**31.8**	**5.9**	1.1	4.8	0.8	4.4	0.9	2.7	2.5	0.4	4.2	21.0	15.6	2.5	13.45	1.29	5.85	1.30	1.06	0.64
24	DF85-109	ASE-E																																							
25	BC451	ASE-E	42	14	4884	86	49	521	10	19	24	113	**165**	**211**	29	181	9	1032	41.2	90.4	9.3	**34.8**	**6.5**	1.1	5.2	0.8	4.7	1.0	2.8	2.9	0.4	4.6	26.0	19.7	2.8	10.73	1.17	6.29	1.45	1.06	0.60
26	BC455	ASE-E	36	13	4755	81	48	480	9	16	24	101	**144**	**245**	27	178	7	1540	40.1	84.6	8.8	**33.1**	**6.1**	1.1	4.9	0.8	4.4	0.9	2.6	2.6	0.4	4.7	21.0	18.4	2.6	13.35	1.38	6.57	1.42	1.03	0.61
	repeat		*37*	*12*	*4569*	*81*	*45*	*483*	*9*	*15*	*24*	*100*	***142***	***250***	*28*	*195*	*6*	*1514*	*40.3*	*85.7*	*8.8*	***33.4***	***6.2***	*1.2*	*5.1*	*0.8*	*4.6*	*0.9*	*2.7*	*2.7*	*0.4*	*4.9*	*21.8*	*15.0*	*2.5*						
27	BC485	ASE-E	47	14	4924	89	49	544	11	21	27	124	**180**	**187**	32	194	11	979	46.0	98.5	10.1	**37.5**	**7.1**	1.2	5.7	0.9	5.2	1.1	3.1	3.1	0.5	4.8	28.0	22.8	3.5	8.21	0.96	6.08	1.62	1.05	0.57
28	DF85 96-1	ASE-E																																							
29	PS69/299-1	ASE-E	31	13	4393	88	50	564	10	16	18	107	**127**	**308**	21	111	5	662	31.1	65.8	6.9	**26.8**	**4.9**	1.1	4.0	0.6	3.6	0.7	2.1	2.1	0.3	3.0	18.8	12.5	2.0	24.56	2.79	5.15	0.96	1.03	0.76
30	BC482	ASE-E	43	11	4284	74	41	509	9	20	23	102	**159**	**139**	26	144	10	676	38.7	80.3	8.4	**31.6**	**5.8**	1.0	4.6	0.7	4.1	0.9	2.4	2.5	0.4	3.8	24.2	19.5	2.8	7.14	0.97	5.63	1.70	1.02	0.57
31	BC476	ASE-E	50	14	4745	84	54	521	11	23	24	112	**203**	**150**	30	137	12	732	47.0	96.7	10.3	**38.6**	**7.1**	1.2	5.7	0.9	5.0	1.0	3.0	3.0	0.4	3.9	27.6	23.9	3.5	6.30	1.10	4.50	1.67	1.01	0.59
32	PS75/159-1	ASE-E	58	13	4624	81	53	474	10	24	18	101	**213**	**133**	30	134	12	711	44.5	91.9	9.8	**36.8**	**6.7**	1.2	5.5	0.9	5.0	1.0	3.0	2.8	0.4	3.6	27.1	19.6	3.1	6.79	0.99	4.46	1.50	1.01	0.60
33	PS75/168-1	ASE-E	58	13	5404	83	47	506	10	19	15	109	**210**	**171**	36	210	12	615	55.0	113.1	12.0	**44.5**	**8.1**	1.3	6.6	1.0	6.0	1.2	3.5	3.3	0.5	5.1	30.6	24.8	3.6	6.90	0.81	5.84	1.98	1.01	0.54
34	BC442	ASE-E	42	13	5684	90	52	489	11	21	24	117	**151**	**224**	29	219	8	1101	42.7	92.6	9.5	**35.6**	**6.7**	1.2	5.3	0.8	4.8	1.0	2.8	2.9	0.4	5.5	24.2	17.2	2.6	13.07	1.02	7.50	1.28	1.06	0.63
35	BC443	ASE-E	41	14	5319	86	51	507	11	21	35	113	**146**	**247**	29	197	8	2080	40.6	88.7	8.9	**33.7**	**6.3**	1.2	5.2	0.8	4.6	1.0	2.7	2.8	0.4	5.0	22.1	15.7	2.5	15.75	1.26	6.87	1.14	1.07	0.63
36	PS69/281-3	ASE-W	48	13	5832	94	46	574	14	23	19	128	**163**	**230**	34	263	11	598	50.9	104.5	11.1	**41.9**	**7.7**	1.3	6.2	1.0	5.7	1.1	3.2	3.0	0.5	6.4	33.0	19.9	3.1	11.55	0.88	7.68	1.52	1.01	0.58
37	NBP07-02	ASE-W																																							
38	BC420	ASE-W	47	17	6113	119	62	762	16	28	25	134	**152**	**211**	31	200	9	664	41.7	88.7	9.3	**35.3**	**6.8**	1.2	5.5	0.9	5.1	1.1	3.0	3.0	0.4	4.8	28.0	18.7	2.7	11.25	1.05	6.46	1.09	1.03	0.62
39	NBP00-01 KC24	ASE-W																																							
40	BC421	ASE-W	48	16	5613	106	57	608	13	24	28	140	**152**	**200**	28	202	9	641	41.6	87.8	9.1	**34.6**	**6.4**	1.2	5.3	0.8	4.6	0.9	2.7	2.7	0.4	5.0	28.3	19.5	2.8	10.23	0.99	7.09	1.25	1.04	0.61
41	BC412	ASE-W	49	14	5395	111	50	722	14	25	33	141	**146**	**201**	28	179	9	658	40.4	85.6	9.2	**35.2**	**6.7**	1.2	5.4	0.8	4.6	1.0	2.6	2.6	0.4	4.7	32.9	18.5	2.6	10.85	1.12	6.39	1.28	1.02	0.61
42	NBP00-01 KC22	ASE-W																																							
43	NBP00-01 KC21	ASE-W																																							
44	NBP07-02	ASE-W																																							
45	PS69/275-2	ASE-W	57	15	5561	120	53	542	13	26	37	179	**165**	**195**	29	214	11	747	43.5	95.1	9.6	**36.1**	**6.8**	1.2	5.4	0.8	4.8	1.0	2.8	2.7	0.4	5.2	28.8	20.5	3.9	9.52	0.91	7.26	1.33	1.07	0.58
46	BC407	ASE-W	58	15	5815	116	53	687	14	26	27	175	**155**	**198**	28	192	10	622	41.1	90.8	9.4	**36.0**	**6.7**	1.2	5.5	0.9	4.8	1.0	2.8	2.6	0.4	4.7	33.8	17.9	3.1	11.04	1.03	6.74	1.20	1.06	0.60
	repeat		*61*	*15*	*5709*	*116*	*53*	*659*	*14*	*26*	*26*	*170*	***159***	***187***	*28*	*194*	*9*	*597*	*41.8*	*90.2*	*9.1*	***34.7***	***6.5***	*1.2*	*5.3*	*0.8*	*4.7*	*0.9*	*2.7*	*2.6*	*0.4*	*4.6*	*32.9*	*17.1*	*2.9*						
47	PS69/283-5	ASE-W	50	14	5819	101	52	608	13	26	28	149	**152**	**202**	27	211	9	595	40.2	90.2	9.0	**33.9**	**6.4**	1.2	5.1	0.8	4.6	0.9	2.7	2.5	0.4	5.1	30.8	16.8	2.5	12.05	0.96	7.94	1.18	1.09	0.62
48	BC431	ASE-W	43	15	5726	103	53	610	14	24	27	130	**146**	**241**	26	194	8	799	40.1	88.7	8.9	**33.9**	**6.4**	1.2	5.1	0.8	4.4	0.9	2.5	2.6	0.4	4.9	29.4	17.8	2.4	13.59	1.25	7.33	1.17	1.08	0.64
49	BC433	ASE-W	46	15	5503	98	44	592	12	22	41	139	**152**	**238**	29	252	9	2212	42.3	98.4	9.2	**34.6**	**6.5**	1.2	5.2	0.8	4.8	1.0	2.8	2.8	0.4	6.0	24.7	16.9	2.4	14.03	0.94	8.64	1.15	1.15	0.63
50	BC492	ASE-W	43	15	5259	93	47	581	12	22	48	129	**141**	**240**	26	235	8	2972	36.7	88.1	8.1	**30.2**	**5.7**	1.1	4.6	0.7	4.2	0.9	2.5	2.5	0.4	5.7	20.6	14.0	2.1	17.15	1.02	9.18	0.91	1.18	0.65
51	ELT33-12	ASE-W																																							
52	ELT33-11	ASE-W																																							
53	PS2545-1	ASE-W	54	14	5868	98	47	667	14	27	37	160	**146**	**233**	25	174	8	546	36.5	80.2	8.1	**30.7**	**5.8**	1.1	4.7	0.7	4.1	0.8	2.4	2.3	0.3	4.2	27.4	15.1	2.2	15.40	1.34	6.98	1.04	1.07	0.63
54	NBP00-01 KC17	ASE-W																																							
55	NBP99-02 PC21	WG																																							
56	NBP99-02 TC23	WG	25	13	8695	94	64	593	16	25	23	125	**98**	**281**	22	243	4	479	32.3	71.0	7.4	**28.3**	**5.4**	1.3	4.6	0.7	4.1	0.8	2.3	2.1	0.3	5.6	20.7	9.9	1.6	28.42	1.16	10.88	0.77	1.06	0.82
57	NBP00-01 PC14	WG	31	13	7712	91	59	629	14	24	27	126	**103**	**284**	24	237	4	513	34.3	77.1	7.5	**29.0**	**5.5**	1.3	4.7	0.7	4.2	0.8	2.4	2.2	0.3	5.4	24.5	11.3	1.7	25.07	1.20	9.76	0.88	1.10	0.77
58	PS75/133-1	WG	31	11	6716	76	45	600	10	18	16	114	**107**	**287**	26	308	4	653	37.9	82.9	8.5	**32.8**	**6.2**	1.5	5.0	0.8	4.3	0.9	2.4	2.3	0.3	6.9	18.6	11.2	1.8	25.63	0.93	11.82	1.05	1.06	0.82
59	PS75/130-2	WG	32	12	6736	94	52	674	15	24	19	113	**106**	**344**	22	227	4	618	35.3	75.2	7.8	**30.2**	**5.8**	1.3	4.6	0.7	3.9	0.8	2.2	2.1	0.3	4.9	20.0	11.2	1.6	30.79	1.52	10.31	0.92	1.04	0.77
60	DF83-III BC28	SBE	76	15	4522	98	78	380	13	34	22	115	**219**	**89**	26	119	17	588	42.5	88.6	9.6	**36.9**	**6.9**	1.2	5.4	0.8	4.5	0.9	2.6	2.5	0.4	3.2	17.7	17.7	2.2	5.03	0.75	4.61	1.20	1.01	0.60
61	NBP96-01 PC12	SBE	71	15	4516	98	81	378	13	35	21	129	**223**	**87**	26	117	17	617	42.9	90.7	9.8	**37.5**	**7.0**	1.2	5.4	0.8	4.5	0.9	2.6	2.5	0.4	3.2	22.7	18.1	2.3	4.78	0.74	4.49	1.19	1.02	0.60
62	NBP96-01 TC13	SBE	71	15	4302	102	83	365	13	35	22	115	**219**	**77**	23	110	16	593	43.0	89.4	9.7	**37.2**	**6.9**	1.2	5.2	0.7	4.0	0.8	2.3	2.2	0.3	3.0	18.1	18.3	2.3	4.20	0.70	4.77	1.19	1.01	0.59
63	NBP99-02 Grab20	SBE																																							
64	DF83 PC31	SBE	66	14	4100	98	81	329	12	32	22	108	**212**	**74**	23	111	15	568	42.2	88.9	9.6	**36.7**	**6.9**	1.2	5.2	0.8	4.1	0.8	2.3	2.4	0.3	3.1	19.3	17.5	2.2	4.24	0.67	4.76	1.25	1.02	0.61
65	DF83-III BC26A	SBE	81	16	4343	104	81	392	13	32	23	119	**257**	**93**	22	96	20	674	40.3	84.7	9.1	**34.8**	**6.4**	1.1	4.9	0.7	3.9	0.8	2.2	2.1	0.3	2.7	19.5	21.4	2.4	4.35	0.97	4.40	1.35	1.01	0.58
66	NBP96-01 JTC11	SBE	81	16	4474	101	79	374	13	31	22	109	**258**	**91**	25	94	19	620	45.5	95.7	10.7	**40.5**	**7.5**	1.1	5.6	0.8	4.5	0.9	2.5	2.3	0.3	2.7	20.5	21.7	3.6	4.21	0.97	3.75	1.36	1.00	0.54
	repeat		*97*	*15*	*4212*	*101*	*74*	*391*	*12*	*31*	*23*	*113*	***262***	***85***	*29*	*108*	*19*	*592*	*48.2*	*####*	*10.8*	***41.1***	***7.6***	*1.2*	*6.0*	*0.9*	*4.8*	*1.0*	*2.7*	*2.5*	*0.4*	*2.9*	*23.2*	*20.6*	*2.3*						
67	DF83-III BC33	SBE	78	16	4518	101	80	385	13	33	21	119	**254**	**92**	23	106	20	669	44.3	92.2	10.1	**38.2**	**7.1**	1.1	5.3	0.8	4.3	0.9	2.4	2.3	0.4	3.0	17.9	22.4	2.6	4.12	0.88	4.50	1.43	1.00	0.56

6. Provenance of glacial-marine sediments

In this section we evaluate the provenance signature of coarse and fine-grained detrital sediment from the seafloor in conjunction with onshore geochemical (Sr and Nd isotope values) and geochronological data (K-Ar and $^{40}Ar/^{39}Ar$ ages on hornblende, biotite, mica grains and whole rock samples, U/Pb zircon ages, and Rb-Sr whole rock ages) compiled from the literature (**Table S2**). Knowledge of the regional tectonic history of West Antarctica is a prerequisite in order to relate offshore $^{40}Ar/^{39}Ar$ mineral ages to bedrock sources, particularly in areas where $^{40}Ar/^{39}Ar$ cooling ages are scarce and comparison with other geochronological data is required. Overall, offshore $^{40}Ar/^{39}Ar$ ages match those reported for outcrops onland, recording largely the erosion of syn-tectonic Palaeozoic to Cenozoic plutons emplaced onto the former magmatic arc along the Gondwana margin, with distinctive thermal age peaks at ~245 Ma, ~170 Ma, ~100 Ma and 50-90 Ma. Onshore U-Pb ages on zircons on crystalline bedrock are sparse, but fall in the range of our offshore $^{40}Ar/^{39}Ar$ data, reflecting West Antarctica's active margin settings. In addition to the thermochronological ages, fine-grained Sr and Nd isotope and trace element fingerprints from the <63µm sediment fraction record an integrated signal of the erosion of major outcropping lithologies. The observed fingerprint in marine sediments allows to distinguish between glaciomarine sediments supplied by five major source sectors on West Antarctica. The integrated signal allows furthermore to identify erosion of volcanic and sedimentary rocks, which are inherently difficult to detect using hornblende and biotite $^{40}Ar/^{39}Ar$ ages (i.e. 'mineralogical or grain-size bias').

6.1. Antarctic Peninsula (AP)

Provenance of ice-rafted detritus

Outcrops of young Late Cretaceous (<90 Ma) to Cenozoic igneous rocks have been documented on the Antarctic Peninsula, especially along the western coasts of Graham and Palmer

Land and on Alexander Island (**Leat et al., 1995; McCarron and Smellie, 1998; Ryan, 2005; Fig. 2, Appendix S2**), recording the latest stage of the eastward-propagating cessation of ocean crust subduction under the Antarctic plate. Of particular interest are igneous rocks of ~12-14 Ma (particularly of hornblende-bearing mafic dykes), 20-21, 47-68 Ma and ~85 Ma, which crop out along the coast of Marguerite Bay on the west side of the Antarctic Peninsula, and at the northern tip of Alexander Island (**Fig. 2 e.g. Ryan, 2007; Appendix S2**), and which could explain the majority of the mineral grain ages observed in the shelf sediments. The extensively outcropping metasedimentary rocks of Carboniferous to Cretaceous age on Alexander Island are depleted in amphiboles and micas (**Pierce et al., 2014**) and hence not captured in the offshore $^{40}Ar/^{39}Ar$ age record. The signature of these sedimentary rocks is however observed by qualitative petrographic analysis and fine-grained Sr and Nd isotope fingerprints. In particular, site 8 sediments contain quarzitic clasts (quartz, feldspars), fine-grained dark lithic clasts (mudstone?), and lithic clasts with a fine-grained pink matrix. This is consistent with erosion of the meta-sedimentary formation on Alexander Island, which is largely composed of feldspathic sandstone, siltstone and black mudstones (**Burn, 1984**), as well as igneous rocks (lava, tuffs) similar to the Tertiary volcanics present on the island (**Care, 1983**).

Provenance of fine-grained detritus

Outcrops of Cretaceous to Cenozoic plutonic and volcanic (<97 Ma) rocks are characterised by radiogenic Nd and Sr isotopic compositions (ε_{Nd} ~-2 to 5; $^{87}Sr/^{86}Sr$ ~0.703-0.708**; Pankhurst et al., 1988; McCarron and Smellie, 1998; Riley et al., 2001, 2003; Ryan, 2005, Fig. 4, Appendix S2**), which are distinct from Jurassic to Cretaceous granitoids in the Antarctic Peninsula and the Amundsen Sea region (ε_{Nd}: -8 to 0; $^{87}Sr/^{86}Sr$ ~0.703-0.715) (**Fig. 4; Appendix S2**). The Antarctic Peninsula Volcanic Group and/or nearby granitoids hence seem to be the likely source for the fine-grained detritus with relatively radiogenic values observed at site 1-4, most proximal to the Graham Land coast (**Fig. 2; Table 2).** Sites 7 and 8 are located near to the Alexander Island, where extensive occurrences of arkosic sedimentary rocks (**Fig. 2, Doubleday et al., 1993**) are characterized by less radiogenic Nd

isotope values (ε_{Nd}: -8 to -3; Fig. 3; **Adams et al., 2005**). The agreement between onshore data and our new offshore data indicate a local source for the marine sediments in the AP sector. We note, however, that a mixture between the granitic and volcanic rocks, which crop out on Alexander Island, could yield a similar isotopic fingerprint.

6.2. Bellingshausen Sea (BS)

Provenance of ice-rafted detritus

Bedrock exposures along the BS coast are extremely rare (**Fig. 2**) and limited to outcrops of some Cretaceous igneous rocks (Rb-Sr whole rock ages of 113 to 128 Ma; **Pankhurst and Rowley, 1991**) and Miocene-Quaternary volcanic rocks (**Smellie, 1999; Hathway, 2001**). Aeromagnetic investigations detected the 'Pacific Margin Anomaly' in the coastal region flanking the BS, notably in its eastern sector (**Ferraccioli et al., 2006**), which has been linked to mafic and intermediate basement rocks $^{40}Ar/^{39}Ar$ dated at 129-141 Ma by (**Maslanyi and Storey, 1990; Vaughan et al., 1998**). Hornblende and biotite $^{40}Ar/^{39}Ar$ ages, extracted from our marine sediment samples, record a dominant age interval of 74 to ~140 Ma with well-defined age peaks of ~110 Ma and ~99-108 Ma, respectively. Onland source rock candidates for such ages are mid-Cretaceous felsic plutons intruding metasedimentary rocks in eastern Palmer Land (**Fig. 2;** $^{40}Ar/^{39}Ar$ dated to 95-119 Ma; **Vaughan et al., 2012b**), and/or older terranes which have been affected by the amphibolite-grade thermo-metamorphic Palmer Land event at 103-107 Ma (**Wendt et al., 2008; Vaughan et al., 2012a**). We suggest that this Palmer Land thermal event potentially affected large parts of the coast around the Bellingshausen Sea. Supporting evidence for this idea comes from the absence of mafic intrusion ages (i.e. Pacific Margin Anomaly; 129-141 Ma) in the sedimentary record of the eastern BS sector. Furthermore, distinctively different geologies along the eastern and western coasts of the Bellingshausen Sea seem not to be reflected in the iceberg-rafted component of the offshore sediments, which show a narrow range of $^{40}Ar/^{39}Ar$ age populations in both hornblende and biotite grains between sites 11 and 13 indicating regional thermal resetting (**Table S2; Figure 2**).

Provenance of fine-grained detritus

Surface sediments in the BS are characterized by lower Nd isotopic composition for a given $^{87}Sr/^{86}Sr$ value compared to the other sectors (ε_{Nd} = -7.3 to -4.2, $^{87}Sr/^{86}Sr$ = 0.7097 to 0.7132; **Fig. 4**). Volcanic rocks of the Antarctic Peninsula Volcanic Group, situated inland of the BS coast (**Figs. 2, 4**), could provide the less radiogenic Nd isotopic compositions, but are Jurassic in age (~160-190 Ma) and have high $^{87}Sr/^{86}Sr$ values (**Riley et al., 2001**). The Cenozoic alkali basalts have very high Nd and low Sr isotope values and thus are unlikely to explain the observed signature in the shelf sediments (**Fig. 4**). Furthermore, clay mineral data from shelf sediments in the BS sector (**Table 2**) make it unlikely that volcanic source rock from along the BS coast contribute significantly to the observed provenance of the glacial-marine sediments, because enhanced smectite contents (indicative of supply of volcanic detritus) are restricted to samples from the easternmost BS sector along the west coast of Alexander Island (**Hillenbrand et al., 2009b)**. More negative ε_{Nd} values, as well as felsic trace element patterns (high Th/Sc, Eu/Eu* and low Sr/Zr and Zr/Y), are consistent indicators of a more evolved source (e.g. **McLennan et al., 1993**), notably in the western BS sector. This observation is in agreement with the clay mineral composition of marine sediments along the southern coast of the BS (**Hillenbrand et al., 2009b**), which is characterised by high illite and low smectite contents (sites 11 to 12), indicating a granitic or gneissic source (**Fig. 5**). Felsic bedrock in the southern hinterland of the BS has indeed been inferred from aeromagnetic observations, with ilmenite-rich intrusions in the west contrasting with magnetite-rich counterparts to the east responsible for the Pacific Margin Anomaly (**Ferraccioli et al., 2006**).

6.3. Amundsen Sea

Provenance of ice-rafted detritus

Ice-rafted hornblende and biotite grains in sediments from the AS are distinct from other sectors on the Pacific margin of West Antarctica because of the significant presence of $^{40}Ar/^{39}Ar$ ages

> 140 Ma (**Fig. 3e,f**). Predominant hornblende age peaks are ~100-110 Ma, ~140-210 Ma, ~250 Ma and ~350 Ma, and ~100-110 Ma, ~170 and ~240 Ma for biotite grains (**Fig. 7**). Similar age populations have been detected in coastal outcrops of mainly calc-alkaline igneous and metaigneous granitoid rocks around the ASE by using a variety of dating methods (**Pankhurst et al., 1993; 1998; Mukasa and Dalziel, 2000; Kipf et al., 2012; Riley et al., 2017; Appendix S2**).

In detail, sites proximal to the coast reveal a different provenance between the Walgreen Coast in the western AS, and the coast extending from Thurston Island towards Pine Island Bay in the eastern AS (**Fig. 2**). Sites 22 and 24-29 along the eastern AS coast are characterized by a large number of grains with ages from 140-210 Ma, while grains from sites proximal to the Walgreen Coast (sites 38, 40-41 and 45) lack such ages (**Fig. 7**). Ice-rafted debris (IRD) supplied by icebergs calved from of the Abbot and Cosgrove Ice Shelves (**Fig. 2**), as well as from Pine Island and/or Thwaites glaciers (sites31-32) are likely sources for the observed $^{40}Ar/^{39}Ar$ ages of 140-210 Ma. The unique geological signature of the Thurston Island block, with its characteristic Jurassic ages, was already specified by **Pankhurst et al. (1993**), based on biotite and hornblende K-Ar ages (~150 Ma) and is also present in our offshore record.

Peak Cretaceous ages for both hornblende and biotite grains are slightly but distinctively (~10 Ma) different between the eastern and western ASE (Fig. 7). Hornblende and biotite grains supplied from the Walgreen Coast (western ASE) record ages of 108-110 Ma, while erosion along the eastern ASE coast sheds grains with a pronounced ~100 Ma age peak (**Fig. 7**). This difference in mineral age population between the western and eastern Amundsen Sea sectors can be related to the diachronous eastward cessation of subduction, and therefore a progression of calc-alkaline magmatism from Marie Byrd Land towards Thurston Island (**Mukasa and Dalziel, 2000**). Finally, a minor ~353 Ma age peak is visible in ice-rafted hornblende grains, particularly at sites 18, 22 and 25-27 proximal to Thurston Island, but not in biotite grains (**Fig. 2, 7; Appendix S1).** Matching ages can be identified onland from a granodioritic orthogneiss formation cropping out on the eastern side of

Thurston Island, which has been dated by zircon U-Pb to ~349 Ma (**Riley et al., 2017**). Material from these outcrops could either be carried by icebergs into the eastern AS sector via the Antarctic Coastal Current, or similar outcrops could be located below ice streams feeding the Abbot Ice Shelf, which eventually calves into the eastern ASE.

Rocks cropping out along the Walgreen Coast have Cretaceous (~100-130 Ma, zircon U-Pb and $^{40}Ar/^{39}Ar$ plateau) and Late Palaeozoic ages (~250 Ma and ~350-500 Ma, zircon U-Pb) (**Pankhurst et al., 1998; Mukasa and Dalziel, 2000; Kipf et al., 2012**). These ages are mostly found in the grains of the proximal offshore sediments, except for the 350-500 Ma age interval, which may be absent due to the limited onshore occurrence of rocks of that age and the limited amount of grains analysed in the marine sediments.

One striking observation when comparing the geological map (**Fig. 2**) with the marine detrital mineral grain ages (**Fig. 3**) is the notable absence of ages that can be related to outcropping Late Cenozoic alkali basalt volcanoes (e.g. Hudson Mountains, Mount Murphy and Mount Takahe, **Fig. 2**), with the exception of site 49 from the continental slope. Explanations for this observation could either involve the limited extent of such lithologies below the erosive ice drainage compared to the igneous batholith, or the fact that hornblende and biotite grains are not present or are too fine-grained to be detected in the coarse (i.e. >150µm) fraction of marine samples, and hence not reflected in the $^{40}Ar/^{39}Ar$ age spectrum.

Provenance of fine-grained detritus

Similar to the $^{40}Ar/^{39}Ar$ ages of the ice-rafted grains, the Sr and Nd isotopic composition of the fine-grained sediments in the AS can be separated into an eastern and western sub-sector, broadly delimited by the extent of the Pine Island and Cosgrove-Abbot troughs in the East and the Dotson-Getz Trough in the West, which are incised into the continental shelf (**Larter et al., 2014; Figs. 2, 4**). Sediments in the western AS are characterized by a very homogeneous Sr and Nd isotope signature

(ε_{Nd} ~-2.9 to -1.8 and $^{87}Sr/^{86}Sr$ ~0.7082 to 0.7101), which correlates with the isotopic signature of Mesozoic granites and granodiorites observed in coastal outcrops (**Fig. 4, 9**). We note that sites 36 to 45 are located proximal to the Dotson Ice Shelf and various parts of the Getz Ice Shelf along the Walgreen Coast. The glaciers feeding into these ice shelves drain distinct, separate basins, but nevertheless the offshore sediment samples record very similar Sr and Nd isotope fingerprints. Site 39 marks an exception to this general pattern (**Fig. 2, 9**), because it is characterized by distinctively higher ε_{Nd} values, potentially due to a much localised source. Supply of material eroded from Palaeozoic granites seems to be a minor contributor to the fine-grained detritus, similar to what was observed for the IRD fraction from sites in this area.

In the eastern AS, sediment recovered just in front of Pine Island Glacier (site 31) shows a different and distinct radiogenic isotope fingerprint (ε_{Nd} = -7.2; $^{87}Sr/^{86}Sr$ = 0.7240; Table 2). This unradiogenic signature is unlikely to be related to proximal outcropping young volcanic rocks, which have more radiogenic (higher) ε_{Nd} and lower Sr isotope ratios (ε_{Nd} ~5; $^{87}Sr/^{86}Sr$ ~0.703; **Hart et al., 1997**). Seismic reflection and airborne potential field data provide evidence for a mixed bed below Pine Island Glacier, consisting of unconsolidated and consolidated sedimentary strata, basement rocks and igneous intrusives (**Smith et al., 2013**). Rocks similar to the Palaeozoic sedimentary outcrops on western Marie Byrd Land could be one candidate to contribute to the observed signature (**Fig. 4**). Petrographic studies on coarse-grained clasts (>2mm) in seafloor surface sediments in a nearby core (PS75/215-1), however, found a largely granitic source for this IRD (**Lindow et al., 2016**). It is unclear whether the IRD originated from below Pine Island Glacier or from granitic islands cropping out in Pine Island Bay. Overall, given the presence of igneous basement and granitic IRD in shelf sediments proximal to Pine Island Glacier, we suggest that the distinctively low ε_{Nd} values and high $^{87}Sr/^{86}Sr$ ratios in fine-grained detrital sediments at site 32 represent a significant input from evolved granites, which experienced significant crustal assimilation during mantle extraction (**Fig. 4**), or sedimentary infill eroded from this source. Such granites crop out further inland in the Jones Mountains and in the Ellsworth-Whitmore Mountains (**Fig. 2, Pankhurst et al.,**

1993; Millar and Pankhurst, 1987). This interpretation is further supported by trace metal compositions showing low Th/Sc and Eu/Eu* (**Fig. 6**), and high Th/Zr ratios (see **Table 3** for values). Such ratios are indicative of felsic rocks such as evolved granites or granites that encountered more crustal assimilation (e.g. **McLennan et al., 1993**).

Along the eastern flank of the AS sector, ε_{Nd} values become consistently lower with increasing distance from inner Pine Island Bay, while $^{87}Sr/^{86}Sr$ values become higher, and eventually overlap with the composition of the local Mesozoic granites (**Figs. 4, 9**). A logical interpretation of this pattern is increasing input of material from the eastern coast of the ASE (between Thurston Island and Pine Island Glacier), where extensive Mesozoic granites are exposed (**Figs. 4 and 9**).

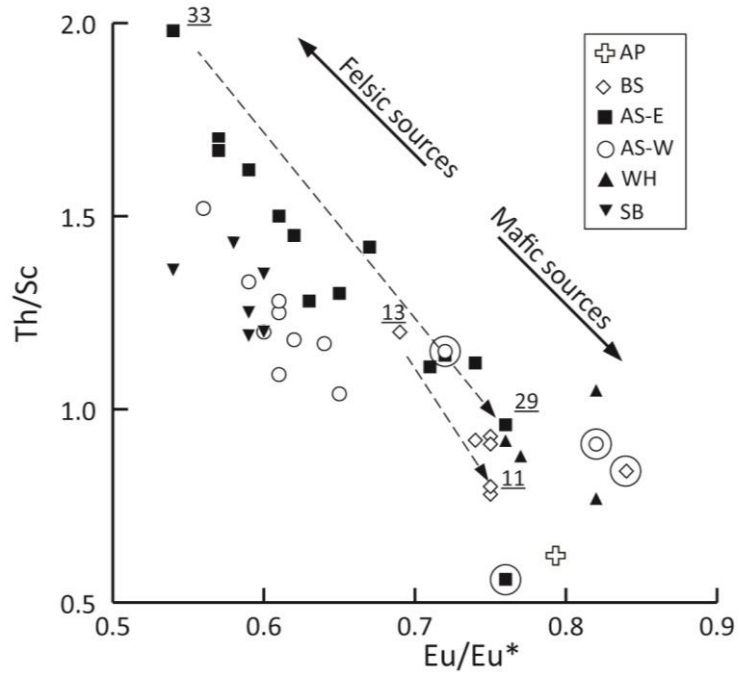

Figure 6: Diagram of Th/Sc vs Eu/Eu* compositions of surface sediments along the Pacific margin of West Antarctica. Circled samples denote sediments with positive cerium anomalies (Ce/Ce*>1.1), indicating minor redox processes affecting the sediments or their sources. Numbers indicate core sites of samples, which are discussed in more detail in the main text. Abbreviations: AP – Antarctic

Peninsula, BS – Bellingshausen Sea, AS-E – eastern Amundsen Sea, AS-W – western Amundsen Sea, WH – Wrigley Gulf – Hobbs Coast, SB – Sulzberger Bay.

6.4. Wrigley Gulf-Hobbs Coast

Provenance of ice-rafted detritus

The Hobbs Coast is characterized by granitoid outcrops with zircon U-Pb ages of ~115 Ma at Mt. Petras (**Figs. 2, 8**), and similar ages elsewhere along the Ruppert Coast in migmatitic, anorogenic, and I-type granitoids (**Mukasa and Dalziel, 2000)**. This age is well reflected in the $^{40}Ar/^{39}Ar$ ages of coarse hornblende and biotite grains in marine sediments from the WH sector with a dominance of ages between 90 and 130 Ma, and slightly younger peak ages of ~100 Ma and ~101 Ma, respectively (**Fig. 3g,h**). Older Palaeozoic granitoids crop out along the Ruppert Coast and in the Ford Ranges. It is however, unlikely that such rocks are present below the drainage basin of the western Getz Ice Shelf, as they are rich in hornblende and biotite grains recording undisturbed K-Ar mineral ages of 324-375 Ma (**Adams, 1987**), which we do not find in the age population of our grains. A secondary biotite $^{40}Ar/^{39}Ar$ age peak of ~53 Ma detected at site 58 is more difficult to explain, as rocks of suitable ages are unknown from the local geology. Previous studies on IRD from sites 58 and 59 have focused on apatite fission track (AFT) thermochronology (**Spiegel et al., 2016**) and found widespread AFT ages of 60 to 80 Ma. AFT thermochronology is based on the analysis of lattice damage caused by the spontaneous fission of radiogenic ^{238}U. This method has a lower closure temperature of ~120°C, and **Spiegel et al. (2016)** correlated AFT ages of 60 to 80 Ma with Cretaceous granitoids, which makes them an unlikely source for ~53 Ma old biotite grains. Basement rocks with (post-) Miocene AFT cooling ages (~20 Ma) on the other hand were interpreted by **Spiegel et al. (2016)** to reflect an unknown source under the Getz Ice Shelf drainage basin. This source is not found in proximal outcrops, but is likely to be composed of granitic and/or diorite material given the petrographic data on IRD (>2mm) from the same site. These rocks could account for our observed ~53 Ma $^{40}Ar/^{39}Ar$ age in the biotite population.

A small number of young hornblende ages (<10 Ma, n=9) are found in the detrital sediments, tracing the erosion of young alkali basalts. Erosion of these volcanic rocks is further confirmed by petrographic IRD analysis carried out by **Spiegel et al. (2016),** revealing the contribution of ~40% from volcanogenic clasts that can be associated with the local alkali basalts. Given the extent of outcropping Cenozoic volcanic rocks in the hinterland of the WH sector (**Fig. 2**), the relative absence of a significant young age peak in our data signifies that these volcanic rocks are likely to contain hornblende and biotite grains that are too small to be detected in coarse marine samples (i.e picked from >150µm fraction).

Provenance of fine-grained detritus

The fine-grained detritus of the WH sector (and site 54 in the western AS, **Fig. 2**) has high ε_{Nd} values and low $^{87}Sr/^{86}Sr$ ratios (Fig. 4), which can be explained by the two major lithologies cropping out along the Hobbs and Ruppert Coasts, the Late Cenozoic alkali basalts and Cretaceous calc-alkaline granites (**Fig. 2**). Mixing calculations between these two end-members suggests a ~30% contribution from alkali basalts and ~70% contribution from Cretaceous granites to the sediments (average Mesozoic granitoids vs. average Late Cenozoic alkali basalts, **Appendix S2**). This assessment is in agreement with the petrographic IRD analysis by **Spiegel et al. (2016)** and further supported by trace element compositions of our detrital sediment samples, which indicate a mixture between a Mesozoic granitic end-member and Cenozoic alkali basalts (**Fig. 4b**). In detail, high Sr/Th (~28) and Zr/Y ratios (~10.5; **Table 3**) and slightly elevated Eu/Eu* ratios relative to the other studied sectors (~0.8) are all consistent with a significant contribution from mafic alkali basalts to the detrital composition of the seafloor sediments.

6.5. Sulzberger Bay

Provenance of ice-rafted debris

During the mid-Cretaceous, rifting of Zealandia from western Marie Byrd Land led to the intrusion of extensive anorogenic granitoids with K-Ar ages of ~98-105 Ma (**Richard et al., 1994; Adams et al., 1995**). These rocks are predominantly exposed in the Ford Ranges and on Edward VII Peninsula, where they crop out alongside Palaeozoic granodiorites (i.e. Ford Granodiorite Suite) and Cambrian-Ordovician metasedimentary rocks (i.e. Swanson Formation) (**Weaver et al., 1992; Adams et al., 1995, Fig. 2**). The Ford Granodiorite Suite contains coarse hornblende and biotite grains with zircon U-Pb and K-Ar hornblende and biotite ages of 320-370 Ma (**Adams, 1987; Pankhurst et al., 1998**). Predominant hornblende $^{40}Ar/^{39}Ar$ ages of 90 to 130 Ma (peak age: ~100 Ma; n=26) in marine sediments in SB indicate limited erosion from the Ford Granodiorite Suite, with the exception of two grains with ages of 347 Ma and 510 Ma (**Appendix S1**). A more likely source for the IRD in the SB sector is hence Edward VII Peninsula (**Fig. 2**). This conclusion seems in contrast to aeromagnetic investigations of the area, which inferred a larger extent for the Ford Granodiorite Suite on Edward VII Peninsula (**Ferraccioli et al., 2002**). Overall, however, our age distribution is in agreement with the ages of local A-type granites, the thermal overprinting ages and the absence of hornblende grains in the sedimentary Swanson Formation (**Adams et al., 1995,** see **Pierce et al. 2014,** for a discussion on durability of hornblende grains in the sedimentary cycle), which crops out extensively on Edward VII Peninsula.

Provenance of fine-grained sediments

In contrast to the IRD signature, low Nd (ε_{Nd}: -11.9 to -10.5) and high Sr isotope values ($^{87}Sr/^{86}Sr$: 0.7411 to 0.7493) in the fine-grained detritus in the SB sector show a strong affinity to the metasedimentary Swanson Formation (ε_{Nd}: -13.4 to -10.5 and $^{87}Sr/^{86}Sr$: 0.7264 to 0.7618) (**Pankhurst et al., 1998; Korhonen et al., 2010**; **Fig. 3**). In detail, Nd isotopic compositions are slightly higher and Nd model ages are slightly younger (~1600 Ma, **Table 2**) than documented for the Swanson

Formation on land (1650-1800 Ma; **Appendix S2**). An additional source is therefore needed to explain the observed signatures, which is readily found in the local A-type granites intruding the Swanson Formation on Edward VII Peninsula (**Weaver et al., 1992**). A mixture between Palaeozoic sediments from the Swanson Formation and Cretaceous anorogenic granitoids in the marine detrital sediments from the SB sector is further suggested by low Sr/Th ratios (4-5) and characteristic low Eu anomalies (Eu/Eu* ~ 0.6), and is consistent with coarse and fine-grained geochemical signatures in marine sediments from the area.

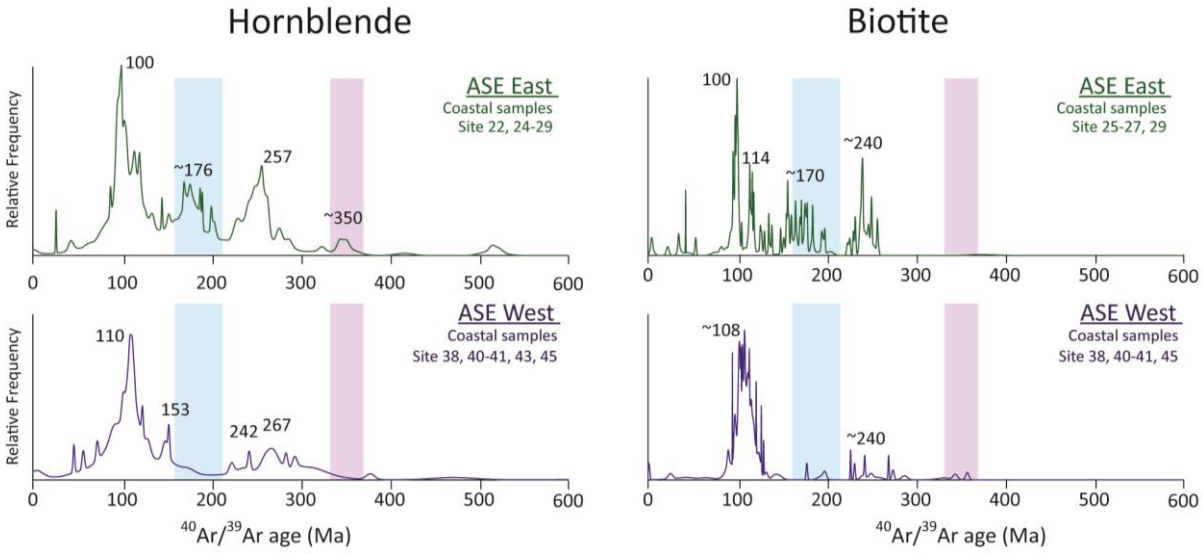

Figure 7: Relative frequency of $^{40}Ar/^{39}Ar$ ages on hornblende and biotite grains from proximal locations in the Amundsen Sea Embayment (ASE). Upper panel displays results for the eastern ASE (sites 22 and 24-29) and lower panel displays results for the western ASE (sites 38, 40-41 and 45). Note the presence of a significant population of hornblende grains with ages of ~140-210 Ma (blue shading) and ~350 Ma (purple shading) in the eastern ASE and their absence from the western ASE.

7. Comparison of different provenance proxies

7.1. $^{40}Ar/^{39}Ar$ ages in hornblende vs biotite grains

Combined analyses of $^{40}Ar/^{39}Ar$ ages from hornblende and biotite grains in detrital sediments allows for more detailed provenance analysis due to the different closure temperatures of both minerals (~550°C and 300°C, respectively). In the case of East Antarctica, partial or total resetting of lower temperature thermochronometers has been observed in several sectors. For example, in detrital sediments from the Wilkes Land sector (90°E to 135°E), a characteristic ~1494 Ma peak age is found in hornblende grains, but is absent from the biotite grains. This observation has been linked to partial resetting of biotite grain ages during the Grenville orogeny (**Pierce et al., 2014**).

In West Antarctica, coastal geology is dominated by Andean-style plutonism of Permian or younger age, resulting in large diorite, granodiorite, monzogranite and syenite intrusions, which in many cases are not overprinted by any major younger tectono-metamorphic events (except for the regional Palmer Land Event at 103-107 Ma). If marine sediment sites are proximal enough to the continental source areas, which carry both large hornblende and biotite grains, as is the case for many of the West Antarctic plutonites, and if the erosional pathway from source to sink does not separate the two mineral phases by differential current sorting, combined biotite-hornblende $^{40}Ar/^{39}Ar$ data sets may be used to broadly support provenance interpretations by inferred cooling rates. We think that a case can be made as large parts of our data set meet these criteria. Overall, probability peaks of hornblende grain ages are similar to or slightly older than those of biotite grains around West Antarctica (**Fig. 3**). Both minerals record a dominant Cretaceous age peak (100-110 Ma) in all sectors, apart from the AP sector (**Fig. 3**). This age interval is particularly well defined in most of the sectors and peak ages between both mineral systems vary by as little as ~2 Ma in the detrital marine sediments (e.g. AS sector; **Fig. 7**). Because magmatic activity has been largely episodic (e.g. **Pankhurst et al., 1993; Leat et al., 1995**), we suggest that these ages point towards regional sources from the same lithological unit (i.e. batholith). Derived cooling rates for the Cretaceous source rocks

would be extremely fast (~>100°C per million years between 550 and 350°C). To our knowledge, there are no detailed investigations on the cooling rates of Cretaceous I-type granitoids from West Antarctica. Concordant ages between zircon U-Pb ages, and reliable $^{40}Ar/^{39}Ar$, K-Ar and Rb-Sr data have nonetheless been observed for intrusive I-type granites on Palmer Land (**Pankhurst and Rowley, 1991; Flowerdew et al., 2005; Vaughan et al., 2012b**). Thermochronological investigations on Cretaceous A-type granites in the Ford Ranges ('Byrd Coast Granites'; **Fig. 2**) have revealed cooling rates of >100°C/Ma, associated with granitic intrusion into the shallow crust (**Richard et al., 1994**). In South America, the emplacement of large Cretaceous plutonic rocks was coeval with the build-up of the Cretaceous batholith on West Antarctica. The mid-Cretaceous plutonic complex in the Coastal Range of central Chile show similar rapid cooling of gabbro to granodiorite suites (93 to 95 Ma based on coupled $^{40}Ar/^{39}Ar$ hornblende, biotite and plagioclase ages), and similar crystallization ages of the same batholith (95-97 Ma; zircon U-Pb ages; (**Parada et al., 2005; Ferrando et al., 2014**). Another comparison can be made for the eastern AS, where detrital hornblende grains yield well-defined ages of ~257 Ma and biotite grains record a younger age of 240 Ma (**Fig. 7**). This age difference would imply an approximate cooling rate of ~15°C per million years for the Permian-Triassic source rocks. This result is consistent with cooling rates of similarly aged dioritic to granodioritic rocks from Thurston Island (~12.5°C/Ma based on K/Ar and $^{40}Ar/^{39}Ar$ on hornblende and biotite; **Pankhurst et al., 1993**) and calc-alkaline diorites of the Median Batholith in New Zealand (~20°C per million years, **Mortimer et al., 1999**), which formed the continuation of the Amundsen Sea province prior to the onset of rifting (**Bradshaw et al., 1997; Vaughan and Storey, 2000**).

Offshore from the Walgreen Coast, pre-Cretaceous (>140 Ma) biotite grains are relatively rare compared to hornblende grains (**Fig. 7**). This observation is explained either by the presence of intermediate to mafic sources which carry more hornblende than biotite (i.e. granodiorite and diorite; **Pierce et al., 2014**), or by thermal resetting of biotite ages during the Cretaceous. Permian diorite and granodiorite outcrops of ~243 Ma and ~283 Ma (zircon U-Pb, **Mukasa and Dalziel, 2000**)

have been identified in the Kohler Range, which is fed by ice streams flowing towards the Walgreen Coast, and could hence indicate a (minor) mineralogical bias towards biotite in the area.

In several locations, a marked distinction between the two chronometers is observed in the offshore record. In addition to the previously mentioned exotic biotite ages of ~53 Ma in the WH sector, hornblende ages of ~350 Ma, which are absent in the biotite record, were found in the eastern AS sector (**Fig. 7**). Comparison with the proximal geology relate these ages to the emplacement of a granodioritic-orthogneiss on Thurston Island (Rb-Sr whole rock: ~309 Ma, **Pankhurst et al., 1993; zircon** U-Pb: ~349 Ma, **Riley et al., 2017**). These gneisses show evidence for realignment and recrystallization of biotite crystals, indicating that a thermal event is likely to have affected the cooling ages of these crystals, possibly during later intrusions of the widespread Permian-Triassic plutonic rocks (~240 Ma).

7.2. Fine-grained sediment provenance derived from radiogenic isotopes and trace elements versus clay mineralogy

Along the Pacific margin of West Antarctica, most of the previous provenance work has focussed on the analysis of mineral assemblages in the clay fraction (<2μm), which was published by **Hillenbrand and Ehrmann (2002**), **Hillenbrand et al. (2003, 2009b)** and **Ehrmann et al. (2011**). In this study, we expanded the existing clay mineral data set by analysing additional samples from the Wrigley Gulf-Hobbs Coast sector (**Table 2**). We here show that the combined study of clay mineralogy and fine-grained sediment fingerprints provides complimentary information on their onshore source.

In the AP and BS sectors, high illite content in shelf sediments (45-70 %) has been found offshore from the eastern tip of Alexander Island, as well as in the western part of the BS sector (**Table 2; Hillenbrand and Ehrmann 2002; Hillenbrand et al., 2003**). The high abundance of illite in these areas was suggested to originate from granitic and gneissic sources. Assumption of a granitic-gneissic source on Alexander Island is based on the presence of plutonic rocks in the eastern part of

the island (i.e. the Rouen Mountains; **Care, 1983**) and the dominance of quartz-mica schistose/gneissic pebbles believed to be derived from the Rouen Mts. in subglacial tills recovered in cores from the nearby shelf **(Kennedy and Anderson, 1989)**. However, erosion of these Tertiary rocks would produce a more radiogenic isotopic fingerprint in the fine-grained material of site 6 than what is observed (ε_{Nd} ~ 2 and $^{87}Sr/^{86}Sr$ ~ 0.705; **McCarron and Smellie, 1998**) (**Fig. 4**). We suggest that the extensively outcropping accretionary sedimentary rocks on Alexander Island (LeMay Formation), which was shown to have high illite content (e.g. **Underwood and Pickering, 1996**) and Nd isotope values of ~ -8 to -3 (**Fig. 4**), are the more likely source rocks for the fine-grained fraction.

The trace element fingerprint (e.g. Th/Sc, Eu/Eu*) of shelf sediments in the BS reveals a mafic eastern sector and a felsic western sector (**Fig. 6**). This finding is confirmed by the clay mineral composition of the sediments that contain up to 66% illite and only 7% smectite in the western part of this sector, while in the eastern part of the sector 44% illite and 20% smectite are found (**Hillenbrand et al, 2009b**). In addition, these observations agree with geophysical surveys, which suggested a felsic composition of the hinterland of the western BS (i.e. Central Domain Eastern Zone; **Ferraccioli et al., 2006**). Shelf sediments further offshore record a mixed signature between these end-members (**Hillenbrand et al, 2009b**), which is consistent with our new data. For example, site 15 (ε_{Nd} = -6.2, Th/Sc = 0.93 and illite = 52%) shows detrital contribution from both end-members (**Table 2, 3**). Based on the clay mineral assemblage in the BS, **Hillenbrand et al. (2003)** proposed sediment material being carried northward by wind- and tide-driven currents without significant influence of the westward-driven coastal current. This fits with our observations, implying a similar sediment transport for the fine-grained sediment (<63µm).

In the AS sector, high kaolinite content in shelf sediments (up to 30 %) has been suggested to originate from pre-Oligocene sedimentary rocks beneath the Pine Island and Thwaites glaciers (**Hillenbrand et al., 2003**; **Ehrmann et al., 2011**), probably sourced from the Byrd Subglacial Basin (**Fig 2**). Such sedimentary rocks do not crop out in the hinterland of the AS (**Fig. 2**), making their

geochemical signature elusive. The comparison between clay mineralogy and the fine-grained geochemistry yields clear correlations between kaolinite content and trace elements (not shown in figures). For example, hafnium (Hf), zirconium (Zr), and Nd exhibit a positive correlation with kaolinite content (R^2= 0.67, 0.62 and 0.62, respectively), while a negative correlation can be observed between kaolinite content and Sr/Zr ratios (R^2= 0.83). In general, kaolinite is associated with chemical weathering of bedrock under warm and humid conditions (**Biscaye, 1965**), and if it is found in Antarctica today, it is assumed to be derived from pre-Oligocene sedimentary strata as it cannot form under glacial conditions (e.g**. Ehrmann et al., 1992**). High Field Strength Elements (HFSEs) such as Zr or Hf, on the other hand, tend to be immobile during chemical weathering and remain in the residues of weathering while lithophile elements (i.e. Sr) are preferentially leached away. Hence, it is tempting to suggest that correlation between kaolinite and Sr/Zr is related to the presence of weathered outcrops in the hinterland. However, we do not observe a relationship between kaolinite and $^{87}Sr/^{86}Sr$ ratios, making glacial weathering a less likely candidate, and instead favour a provenance change as an explanation for Sr concentrations and isotopic compositions.

8. Geochemical signature of ice drainage basins and influence of marine sediment transport

Detailed geochemical characterization of the sediment provenance offshore from individual ice drainage basins gives valuable information on the integrated signature of subglacial geology and dispersal of glacially eroded detritus onto the shelf and further into the deep sea. It also provides the necessary modern day understanding how to use provenance analyses for palaeo-ice sheet reconstructions from marine down-core records (e.g. for East Antarctica; **Cook et al., 2013, 2017; Pierce et al., 2017**). The relatively young geological history of West Antarctica means that individual ice drainage basins will show less pronounced geochemical differences when compared to East Antarctica (e.g. **Pierce et al., 2011, 2014**) or the North Atlantic (**e.g. Hemming, 2004**). For instance,

Pb analyses of K-feldspars grains have been shown to be a valuable tool for distinguishing erosional inputs from West and East Antarctic source terranes (**Flowerdew et al., 2012**). However, Pb isotopic values are remarkably uniform on West Antarctica due to the exclusively mantle-derived sources for the exposed crystalline bedrock (**Mukasa and Dalziel, 2000; Flowerdew et al., 2012**). Our multi-proxy approach nevertheless allows us to distinguish distinct ice drainage basins within West Antarctica as well as sediment transport pathways.

8.1. Coarse-grained detrital sediment signature and potential transport pathways

The modern IRD in the Southern Ocean is supplied by melting of calved icebergs. Ice-rafting has been described as the main mechanism for the transport of coarse detritus from the Antarctic continent to the pelagic realm as ocean currents can only transport finer sediments (e.g. **Diekmann and Kuhn, 1999**). The westward flowing Antarctic Coastal Current is of particular relevance, as it dominates the transport of icebergs in proximity to the coast (e.g. **Stammerjohn et al., 2015; Kim et al., 2016a; Fig. 8**). We find a strong contrast in IRD provenance patterns between the AP and the BS sectors (**Figs. 3, 8**). Relatively young ages observed in the AP sector are sourced from the west coast of the Antarctic Peninsula, where outcrops of magmatic rocks of Late Cretaceous to Cenozoic ages produced by the eastward migration of the active subduction of the (proto-) Pacific plate under West Antarctica during that time are widespread (**Leat et al., 1995**). This can be explained by the fact that most icebergs from the Antarctic Peninsula are deflected northwards into the ACC by cyclonic gyres on the shelf before reaching the BS sector (e.g. **Hofmann et al, 1996; Smith et al., 1999**; **cf. Hillenbrand et al., 2003**) (**Fig. 8**).

In the BS sector, the $^{40}Ar/^{39}Ar$ hornblende and biotite ages are relatively uniform in proximal and distal sediments and record sources with a strong mid-Cretaceous thermo-metamorphic event related to suturing between the western/central domains with the eastern domain of the Antarctic Peninsula (**Fig. 1**). These ages are not found in the AP sector. A large cyclonic gyre in the southern Bellingshausen Sea deflects the coastal current along the eastern flank of Thurston Island (~95°W)

(**Gladstone et al., 2001; Assmann et al., 2005; cf. Hillenbrand et al., 2003**), injecting most of the icebergs into the ACC. Some westward IRD transport may also occur within the Antarctic Coastal Current, but this is difficult to trace due to the ubiquitous nature of mid-Cretaceous thermochronological ages around West Antarctica (**Fig. 8, Appendix S1**).

Most of the outcrops in the AS sector are located around Thurston Island and along the Walgreen Coast, where ice streams are feeding into the Abbott and Cosgrove and the Dotson and Getz ice shelves, respectively (**Fig. 2**). Proximal ice-rafted grains in these two areas show similar mid-Cretaceous and Permian-Triassic ages (~100 Ma and ~250 Ma), but are distinct from the other sectors by the presence of grains with Jurassic ages (140-210 Ma), which mainly occur offshore from the Abbott and Cosgrove ice shelves (**Fig. 7, 8**). Although the numbers of grains analysed in samples just offshore from Pine Island Glacier (n=1) and Thwaites Glacier (n=9) are low, they also include grains of Jurassic ages (**Appendix S1**). This shows that the main source for Jurassic hornblende and biotite grains to the AS sector (and off West Antarctica) originates from the Cosgrove and Abbott ice shelves and from the Pine Island and Thwaites glaciers. In addition, surface currents in the ASE are influenced by the Antarctic Coastal Current. This current is overall weak (~ 1.0 cm s^{-1}) within the embayment, but appears strongest near the coastline (**Assmann et al., 2005; Stammerjohn et al., 2015; Kim et al., 2016a**). We observe Jurassic grains at sites on the continental slope and rise offshore from Dotson-Getz Trough (sites 50-52). We suggest that icebergs that drift generally westwards within the ASE (e.g. **Mazur et al., 2017**) transport the Jurassic grains from the eastern ASE to these locations, which are all situated south of the southern boundary of the ACC (**Figs. 2, 8**).

In general, IRD in samples from the continental slope and rise in the Amundsen Sea shows a larger age population (~30-80 Ma) than IRD on the continental shelf (**Fig. 8**). This feature is particularly pronounced around 70°S latitude. Source areas for grains of this age range could be either the western AP or the Hobbs Coast (sites 58-59) (**Figs. 3, 8**), both of which would require iceberg drift in opposing directions. Support for an AP provenance comes from petrographic

observations on Plio-Pleistocene ice-rafted cobbles at DSDP Leg 35 Site 324 (located offshore from site 17) that show a provenance from Alexander Island (**Tucholke et al., 1976; Veevers and Saeed, 2013**). An argument against a far-travelled signal from the AP, however, is the lack of significant numbers of hornblende and biotite grains of this age range in the BS, as well as the existence of the large gyre in the BS, which carries most of the icebergs north-east towards the ACC (e.g. **Assmann et al., 2005) (Fig. 8)**. Oceanographic observations indicate that sites at around 70°S in the Amundsen Sea are located within the eastward flow of the ACC (**Orsi et al., 1995; Stammerjohn et al., 2015**). This suggests that the source of the ~30-80 Ma old grains at the corresponding sites lies to the west. Indeed, our samples from the Hobbs Coast shelf show a well-defined ~50 Ma age peak, which indicates this area as the potential source for these young detrital grains (**Fig 3h**). The corresponding sites are located proximal to the westernmost Getz Ice Shelf. While the ~54 Ma age is unknown from onshore outcrops, it could represent a hidden source under the ice (cf. **Spiegel et al. 2016)**. At present, icebergs calving from the westernmost Getz Ice Shelf drift westwards with the Antarctic Coastal Current towards the Ross Sea and are injected into the ACC offshore from Sulzberger Bay (**Merino et al., 2016; Tournadre et al., 2016**).

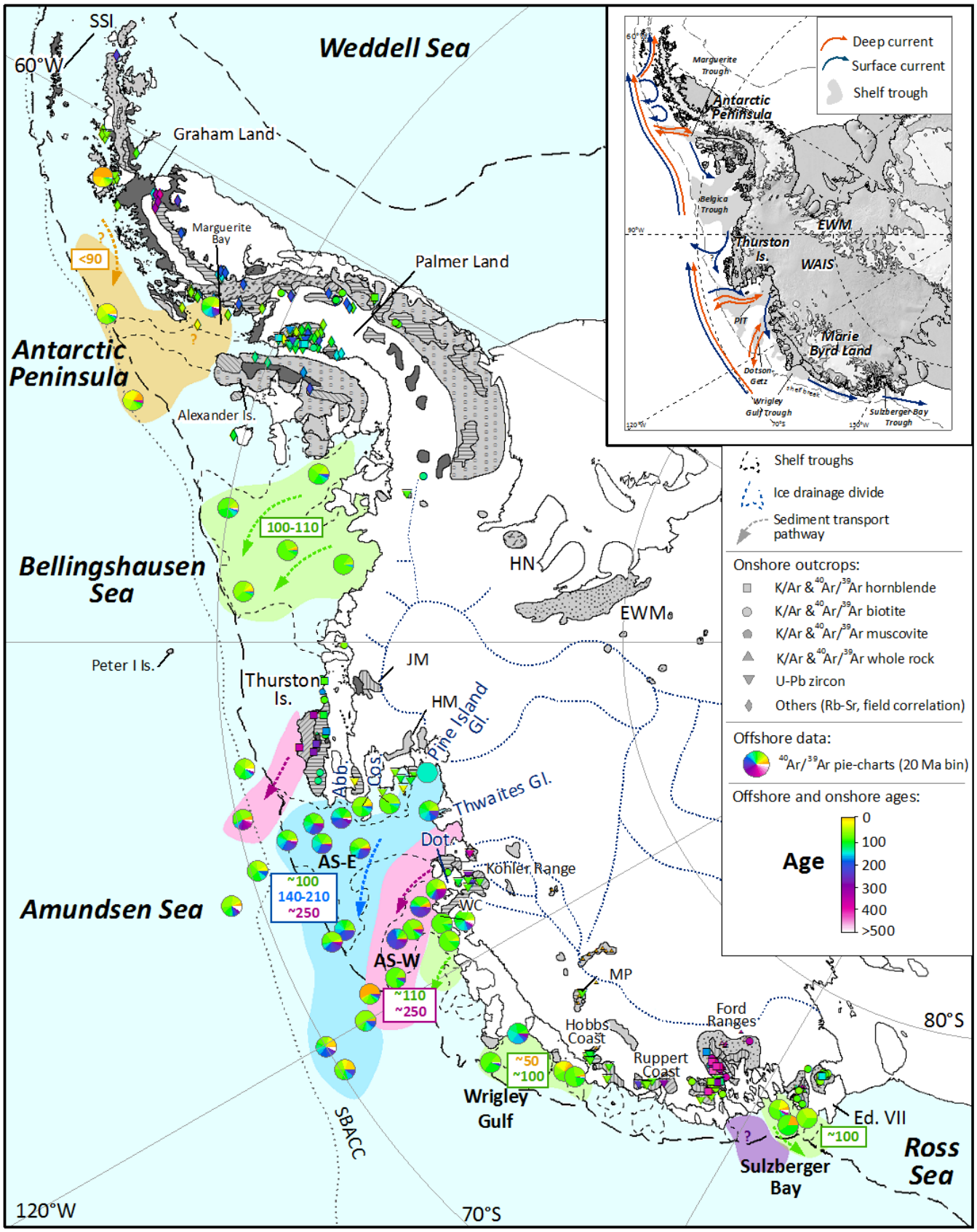

Figure 8: Distribution of thermochronological ages in offshore sediments and terrestrial outcrops of West Antarctica. $^{40}Ar/^{39}Ar$ ages of ice-rafted hornblende and biotite grains are presented as pie charts in 20 Ma increments. Outcrop ages are displayed with different symbols depending on the type of mineral and the method applied (see Appendix S2). Simplified geology is shown in grey-scale after Fig. 2. Thick dashed black lines indicate the approximate location of the shelf break. Coloured dashed arrows and underlying colour field denote major ice-rafted debris transport pathways. Abbreviations and inlet figure are the same as for Fig. 2.

8.2. Fine-grained detrital sediment signature and potential transport pathways

In the modern Southern Ocean, coarse grained terrigenous debris is typically transported by icebergs, which follow wind-driven surface currents. Fine-grained sediments are also transported by these icebergs, but suspended particulates can additionally be transported by meltwater plumes, tidal, thermohaline, and geostrophic currents, as well as gravitational downslope processes such as turbidity currents (e.g. **Aitken and Bell, 1998; Pudsey and Camerlenghi, 1998; Diekmann and Kuhn, 1999**). Similar to the sand provenance signature, the geochemical fingerprint of the studied proximal fine-grained glacial-marine sediments off West Antarctica matches the nearby coastal geology very well, excluding a significant contribution of dust, which plays a more important role for the deposition of fine-grained detritus in the Sub-Antarctic Pacific sector of the Southern Ocean (e.g. **Lamy et al., 2014**). The fingerprint of sediments can be traced offshore, revealing the transport pathway of fine grains across the continental shelves.

In the AP sector, similarities in the radiogenic isotope fingerprint of site 7 on the shelf and site 8 located on the continental rise suggest seaward transport of detrital particles originating from the metasedimentary rocks on Alexander Island (**Table 2, Fig. 9).** Such a transport pathway across the western Antarctic Peninsula continental shelf has been described before for fine-grained terrigenous detritus (**Hillenbrand and Ehrmann, 2002**). In the BS, proximal sites denote felsic and

mafic sources in both its western and eastern parts, consistent with aeromagnetic observations in the area (**Ferraccioli et al., 2006; Bingham et al., 2002**). Following the Belgica palaeo-ice stream Trough northwards, sediments record a mixing signature between these two areas, which has previously been attributed by wind- and tidal-driven currents (**Hillenbrand et al., 2003, 2009**).

A good example of bathymetrically constrained dispersal of fine-grained detritus is observed in the AS sector. Provenance of sediments proximal to the Pine Island and Thwaites glaciers is distinct, pointing to a felsic source or igneous rock with a geochemical signature of enhanced crustal assimilation underneath these two major ice drainage basins. Progressive northward change in sediment provenance along the eastern AS requires that sediment with this distinct fingerprint is transported northwards, and diluted along the way with Palaeozoic-Mesozoic source rocks along the eastern flank of the ASE (**Fig. 9**). The fact that samples from Dotson-Getz Trough show a uniform fine-grained fingerprint indicates that no significant cross shelf transport of fine-grained particles from further east or west occurred, as this would be recognizable in the radiogenic isotope signature of the samples. A candidate for the observed undiluted northward sediment transport is the northward return flow of upwelled Circumpolar Deep Water, after interacting with the base of the ice shelves, as Antarctic Surface Water (**Jenkins et al., 2016**). Observation from autonomous underwater vehicles found melt-laden outflow from ice shelves in the ASE to carry suspended sediment, which is sourced from the sediment-laden base of the ice shelves (**Jenkins et al., 2016; Miles et al, 2016**). This sediment-laden meltwater reaches the mid-depths of the water column and is transported northwards along the bathymetric troughs (e.g. **Kim et al., 2016b**). Release of this suspended particulate matter occurs notably along its main transport pathway, explaining the consistent provenance signatures of fine-grained sediment along the cross-shelf troughs in the ASE.

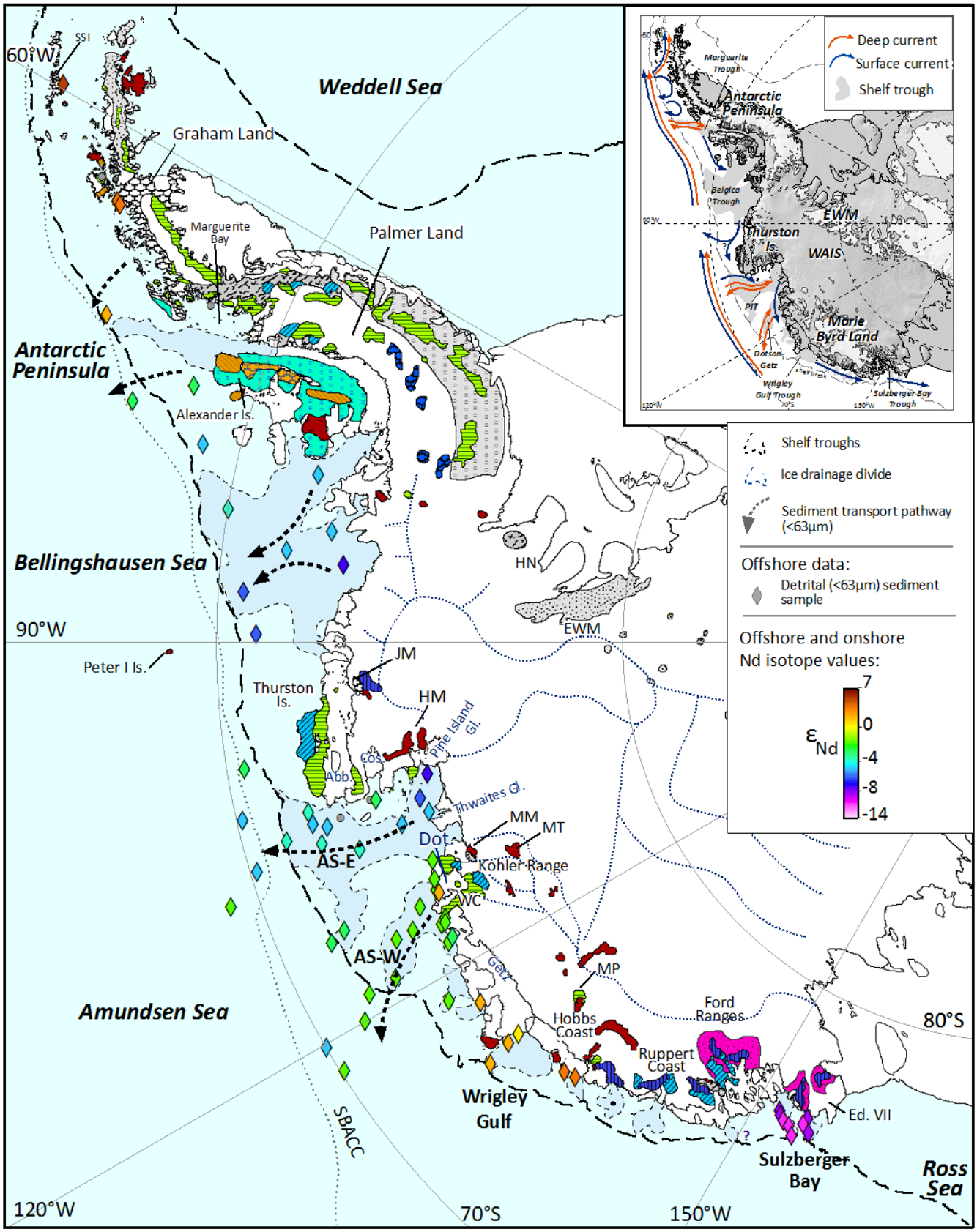

Figure 9: Distribution of Nd isotope composition (ε_{Nd}) in marine sediments and terrestrial rocks. The geology is based on Fig. 2. Note: Colour scheme for outcrops is based on the average Nd isotopic composition of the lithology (see Appendix S2 for data assimilated from the literature). Geological units which could not be assigned a Nd isotope fingerprint are shown in grey. Two different colours were assigned to the Antarctic Peninsula Volcanic Group depending on the regional geochemical variation of these rocks (e.g. Riley et al., 2001, see Table S2 and text). Dashed black lines delineate the approximate location of the shelf break. Black dashed arrows denote major fine-grained (<63um) transport pathways. Abbreviations and inlet figure same as for Fig. 2.

8.3. The geochemical fingerprint of West Antarctic provenance regions in the Pacific sector of the Southern Ocean

An integrated provenance approach allows for a characterization of subglacial sources from individual ice drainage basins along the Pacific margin of West Antarctica. **Figure 10** presents provenance characteristics compiled from our new data set and previously published studies for five different West Antarctic sectors. An erosional source from the Antarctic Peninsula is best identified by a predominance of $^{40}Ar/^{39}Ar$ ages spanning 30-90 Ma in coarse-grained IRD and a very radiogenic fingerprint of fine-grained detrital sediments (ε_{Nd} up to +0.9 and $^{87}Sr/^{86}Sr$ ratios down to 0.705). The only other West Antarctic area that exhibits similar characteristics is the Hobbs Coast, where most biotite and hornblende $^{40}Ar/^{39}Ar$ ages are, however, older (90-140 Ma) and Nd model ages are younger (700 to 770 Ma). Both areas are also relatively far apart from each other, which should not impede their respective identification in down-core studies on marine sediment cores collected proximal to these source regions. The Bellingshausen Sea sector shows a predominance of IRD $^{40}Ar/^{39}Ar$ ages around ~110 Ma, which are similar to those from the Wrigley Gulf-Hobbs Coast sector (~100 Ma), but the fine-grained detritus in the former sector has lower Nd values and higher $^{87}Sr/^{86}Sr$ ratios (ε_{Nd} = -4.3 to -7.2; $^{87}Sr/^{86}Sr$ = 0.710-0.713), as well as significantly older Nd model ages

(1180-1350 Ma). The oldest protolith ages in West Antarctica are indicated by Nd model ages of 1570 to 1700 Ma in Sulzberger Bay, which also stands out by the unradiogenic isotope fingerprint of fine-grained detrital sediments (ε_{Nd} <-10.6; $^{87}Sr/^{86}Sr$ > 0.741).

Finally, a more detailed picture starts emerging for the Amundsen Sea sector, the locus of major glacial ice loss in Antarctica today. While both the eastern and western AS sub-sectors are characterized by hornblende and biotite ages of ~110 Ma and 240-260 Ma, ages of 140 to 210 Ma are more prevalent in the eastern ASE. Furthermore, source rocks to the eastern ASE seem to extend to older Nd model ages (up to 1300 Ma, ε_{Nd} = -7.2) than in the western ASE (900-1000 Ma, ε_{Nd} = -1.7 to -2.9). Further studies are required to reveal whether this observation points to a distinct bedrock source under Pine Island Glacier, a result with major implications for tracing past WAIS retreat and collapse.

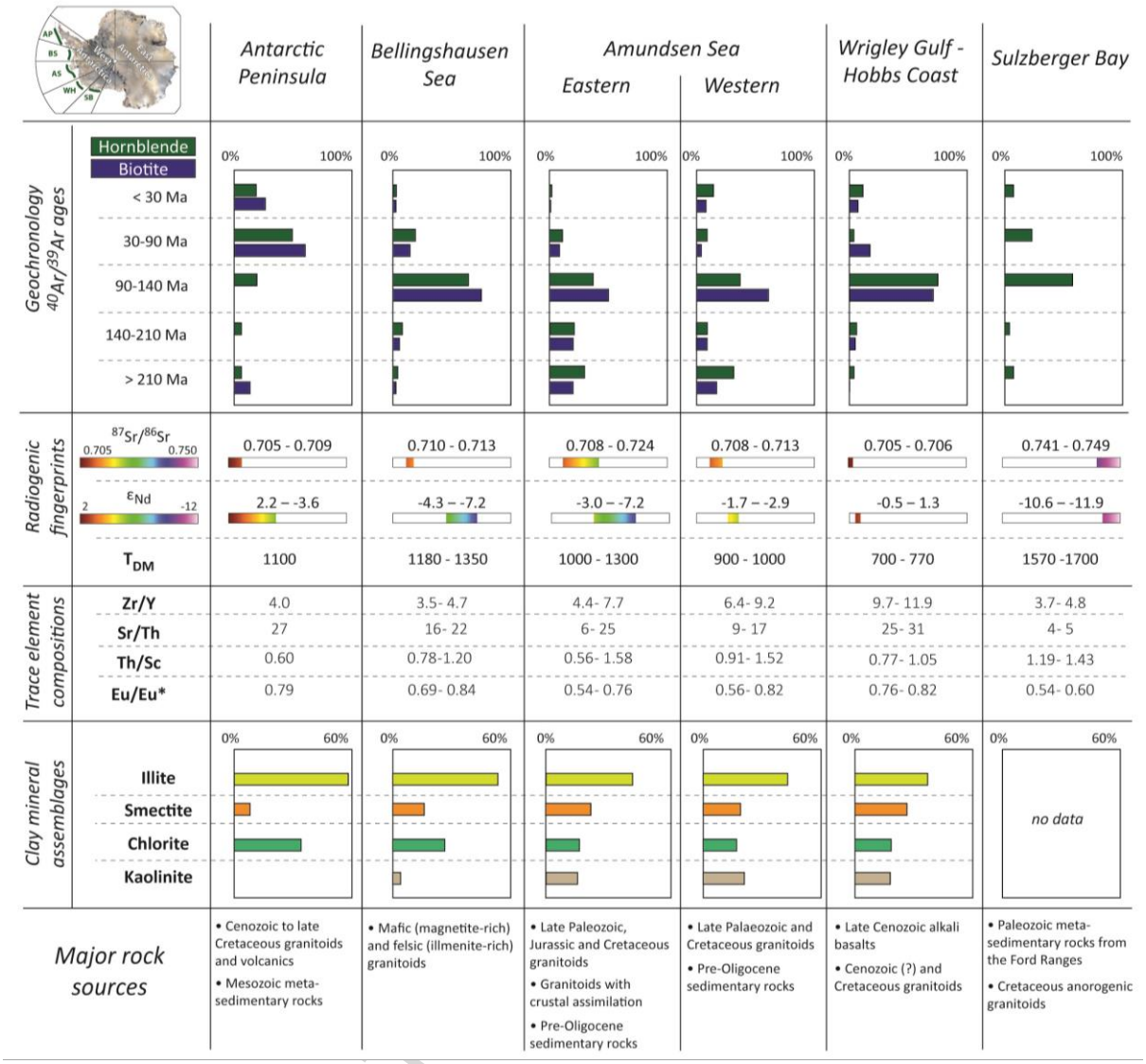

Figure 10: Summary figure of geochemical and clay mineralogical provenance characteristics of different sectors along the Pacific margin of West Antarctica as derived from analyses of detrital marine sediments. Clay mineral assemblages are taken from Hillenbrand and Ehrmann (2002), Hillenbrand et al. (2003, 2009b) and Ehrmann et al. (2011), and major terrestrial rock sources are compiled from the literature (see text for further details).

9. Conclusions

We here report for the first time a detailed geochemical approach to unraveling different provenance sectors along the Pacific margin of West Antarctica. By investigating the fingerprints of

fine-grained terrigenous detritus and coarse-grained ice-rafted debris in ice-sheet proximal to distal marine sediments of Late Holocene age, we draw the following conclusions:

(1) Thermochronological $^{40}Ar/^{39}Ar$ dating on individual mineral grains highlights the Phanerozoic history of West Antarctica. Hornblende and biotite ages can be readily associated with extensively outcropping granites and granodiorites and allow us to distinguish the following sectors: Antarctic Peninsula (~52 and ~74 Ma), Bellingshausen Sea, Wrigley Gulf-Hobbs Coast and Sulzberger Bay sectors (~100-110 Ma) and Amundsen Sea sector (~100-110 Ma and ~140 to 360 Ma). $^{40}Ar/^{39}Ar$ dating of hornblende and biotite grains is less suitable for detecting Late Cenozoic alkali basalts and metasedimentary units around West Antarctica (i.e. mineralogical or grain-size bias).

(2) Strontium (Sr) and neodymium (Nd) isotopic compositions in fine-grained detrital sediments match the coastal geology, and observed geochemical variability can be readily related to genetic and lithological differences in source rocks. Data range from radiogenic values around the (young) Antarctic Peninsula (ε_{Nd} = -3.6 to +0.9; $^{87}Sr/^{86}Sr$ = 0.705-0.709) to less radiogenic values around the Sulzberger Bay, where mantle extraction ages point to a much older protolith (up to 1700 Ma). An exciting finding is a potentially distinct geological source (i.e. Cretaceous granites that experienced extensive crustal assimilation) beneath Pine Island Glacier, which was identified in the radiogenic isotope composition of fine-grained sediments near its calving front. While major Palaeozoic to Mesozoic geological units in West Antarctica are identified in the provenance of the marine sediments, the fine fraction analyses prove particularly useful in detecting Late Cenozoic alkali basalts and metasedimentary rocks, as well as distinguishing A-type granites and granites with pronounced crustal assimilation signatures.

(3) Despite an overall small variation of trace element compositions in marine detrital sediments off West Antarctica, they nevertheless complement isotopic provenance analyses and are broadly indicative of mafic and felsic source rocks. Significant variability within

individual ice drainage basins may prove useful for provenance studies on the local to regional scale, as indicated by contrasting hinterland geology between the eastern and western Bellingshausen Sea, the eastern and western Amundsen Sea embayment, Wrigley Gulf-Hobbs Coast and Sulzberger Bay.

(4) Combined provenance studies on different size fractions of detrital sediments enable monitoring of modern sediment transport pathways. For example, the occurrence of ~140-210 Ma old ice-rafted grains in the western Amundsen Sea sector, which originate from the eastern coast of the Amundsen Sea Embayment, highlights the modern pathway of wind-driven iceberg trajectories within the area. On the other hand, fine-grained sediments can additionally be transported by currents, as exemplified by an evolving radiogenic isotope signature from Pine Island Bay towards the shelf break.

Our study highlights the importance of integrated studies for identifying the geochemical fingerprints of individual ice drainage basins around West Antarctica. Such modern-day studies do not only provide the basis for any attempts to reconstruct ice drainage patterns and ice sheet extent in West Antarctica during the past, but also allow valuable insights into the geology under the ice.

Acknowledgments

P. Simões Pereira acknowledges the Kristian Gerhard Jebsen Foundation for supporting his PhD scholarship. S. Brachfeld and C. Doherty acknowledge support from National Science Foundation grant 0348274. We thank B. Coles and K. Kreissig for their assistance in the lab, W. Ehrmann for analysing the clay mineral assemblages on several samples and T. Riley for constructive discussions. We also thank the shipboard scientific parties, captains, officers and crews of the various expeditions. This research used samples provided by the Antarctic Marine Geology Research Facility (AMGRF) formerly at Florida State University.

References

Adams, C. J., 1987. Geochronology of granite terranes in the Ford Ranges, Marie Byrd Land, West Antarctica. New Zealand Journal of Geology and Geophysics 30, 51-57.

Adams, C. J., Pankhurst, R. J., Maas, R., Millar, I. L., 2005. Nd and Sr isotopic signatures of metasedimentary rocks around the South Pacific margin and implications for their provenance. In: Vaughan A. P. M., Leat P. T. and Pankhurst R. J. (eds). Terrane Processes at the Margins of Gondwana. Geological Society, London, Special Publications 246, 113-141.

Adams, C. J., Seward, D., Weaver, S. D., 1995. Geochronology of Cretaceous granites and metasedimentary basement on Edward VII Peninsula, Marie Byrd Land, West Antarctica. Antarctic Science 7 (3), 265-277.

Aitken, A. E., and Bell, T. J., 1998. Holocene glacimarine sedimentation and macrofossil palaecology in the Canadian High Arctic: environmental controls. Marine Geology 145, 151–171.

Aitken, A. R. A., Young, D. A., Ferraccioli, F., Betts, P. G., Greenbaum, J. S., Richter, T. G., Roberts, J. L., Blankenship, D. D., Siegert, M. J., 2014. The subglacial geology of Wilkes Land, East Antarctica. Geophysical Research Letters 41, 2390-2400.

Arneborg, L., Wåhlin, A. K., Björk, G., Liljebladh, B., Orsi, A. H., 2012. Persistent inflow of warm water onto the central Amundsen shelf. Nature Geoscience 5, 876-880, doi:10.1038/ngeo1644.

Assmann, K. M., Hellmer, H. H., Jacobs, S. S., 2005. Amundsen Sea ice production and transport. Journal of Geophysical Research 110, C12013.

Assmann, K., Jenkins, A., Shoosmith, D., Walker, D., Jacobs, S. S., Nicholls, K., 2013. Variability of circumpolar deep water transport onto the Amundsen Sea continental shelf through a shelf break trough. Journal of Geophysical Research 118, 6603–6620.

Bamber, J. L., Riva, R. E. M., Vermeersen, B. L. A., LeBrocq, A. M., 2009. Reassessment of the potential sea-level rise from a collapse of the West Antarctic Ice Sheet. Science 324, 901–903.

Bayon, G., Burton, K. W., Soulet, G., Vigier, N., Dennielou, B., Etoubleau, J., Ponzevera, E., German, C. R., Nesbitt, R. W., 2009. Hf and Nd isotopes in marine sediments: constraints on global silicate weathering. Earth and Planetary Science Letters 277, 318–326.

Bingham, R. G., Ferraccioli, F., King, E. C., Larter, R. D., Pritchard, H. D., Smith, A. M., Vaughan, D. G., 2002. Inland thinning of West Antarctic Ice Sheet steered along subglacial rifts. Nature 487, 468-471.

Biscaye, P. E., 1965. Mineralogy and sedimentation of recent deep-sea clay in Atlantic Ocean and adjacent seas and oceans. GSA Bulletin 76, 803–832.

Blum, J., and Erel, Y., 1997. Rb-Sr isotope systematics of a granitic soil chronosequence: The importance of biotite weathering. Geochimica et Cosmochimica Acta 61 (15), 3193-3204.

Boger, S. D., 2011. Antarctica — Before and after Gondwana. Gondwana Research 19, 335-371.

Bradschaw, J. D., Pankhurst, R. J., Weaver, S. D., Storey, B. C., Muir, R. J., Ireland, T. R., 1997. New Zealand Superterranes recognized in Marie Byrd Land and Thurston Island. In: Ricci C. A. (eds), The Antarctic Region: Geological Evolution and Processes, 429-436.

Burn, R. W., 1984. The geology of the LeMay Group, Alexander Island. Scientific Report British Antarctic Survey 109.

Burton-Johnson, A., and Riley, T. R., 2015. Autochthonous v. accreted terrane development of continental margins: a revised in situ tectonic history of the Antarctic Peninsula. Journal of the Geological Society 172, 822-835.

Care, B. W., 1983. The petrology of the Rouen Mountains, northern Alexander Island. British Antarctic Survey Bulletin 52, 63–86.

Carvajal, G. K., Wåhlin, A. K., Eriksson, L. E. B., Ulander, L. M. H., 2013. Correlation between synthetic aperture radar surface winds and deep water velocity in the Amundsen Sea, Antarctica. Remote Sensing 5, 4088–4106, doi:10.3390/rs5084088.

Cawood, P. A., 2005. Terra Australis Orogen: Rodinia breakup and development of the Pacific and Iapetus margins of Gondwana during the Neoproterozoic and Paleozoic. Earth-Science Reviews 69, 249-279.

Colville,E. J., Carlson, A. E., Beard, B. L., Hatfield, R. G., Stoner, J. S., Reyes, A. V., Ullman, D. J., 2011. Sr-Nd-Pb Isotope Evidence for Ice-Sheet Presence on Southern Greenland during the Last Interglacial. Science 333 (6042), 620-623.

Cook, C. P., Hemming, S. R., van de Flierdt, T., Pierce Davis, E. L., Williams, T., Galindo, A. L., Jimenez-Espejo, F. J., Escutia, C., 2017. Glacial erosion of East Antarctica in the Pliocene: a comparative study of multiple marine sediment provenance tracers. Chemical Geology (in press).

Cook, C. P., Hill, D. J., van de Flierdt, T., Williams, T., Hemming, S. R., Dolan, A. M., Pierce, E. L., Escutia, C., Harwood, D., Cortese, G., Gonzales, J. J., 2014. Sea surface temperature control on the distribution of far-travelled Southern Ocean ice-rafted detritus during the Pliocene. Paleoceanography 29, doi:10.1002/2014PA002625.

Cook, C. P., van de Flierdt, T., Williams, T., Hemming, S. R., Iwai, M., Kobayashi, M., Jimenez-Espejo F. J., Escutia, C., González, J. J., Khim, B.-K., McKay, R. M., Passchier, S., Bohaty, S., Riesselman, C. R., Tauxe, L., Sugisaki, S., Galindo, A. L., Patterson, M. O., Sangiorgi, F., Pierce, E. L., Brinkhuis, H., IODP Expedition 318 Scientists, 2013. Dynamic behaviour of the East Antarctic ice sheet during Pliocene warmth. Nature Geoscience 6, 765-769.

Cunningham, A. P., Larter, R. D., Barker, P. F., Gohl, K., Nitsche, F. O., 2002. Tectonic evolution of the Pacific margin of Antarctica 2. Structure of Late Cretaceous–early Tertiary plate boundaries in the Bellingshausen Sea from seismic reflection and gravity data. Journal of Geophysical Research: Solid Earth 107 (B12), EPM 6-1 – EPM 6-20, doi: 10.1029/2002JB001897.

Dalrymple, G. B., Alexander, E. C. Jr., Lanphere, M. A., Kraker, G. P., 1981. Irradiation of samples for 40Ar/39Ar dating using the Geological Survey TRIGA reactor. U.S. Geological Survey Professional Paper 1176.

Dalziel, I. W. D., and Elliot, D. H., 1982. West Antarctica: Problem child of Gondwanaland. Tectonics 1 (1), 3-19.

DeConto, R. M., and Pollard, D., 2016. Contribution of Antarctica to past and future sea-level rise. Nature 531, 591-597, doi: 10.1038/nature17145.

Diekmann, B., and Kuhn, G., 1999. Provenance and dispersal of glacial–marine surface sediments in the Weddell Sea and adjoining areas, Antarctica: ice-rafting versus current transport. Marine Geology 158, 209-231.

Doubleday, P. A., Macdonald, D. I. M., Nell, P. A. R., 1993. Sedimentology and structure of the trench-slope to forearc basin transition in the Mesozoic of Alexander Island, Antarctica. Geological Magazine 130 (6), 737-754.

Downing, G. E., Hemming, S. R., Jost, A., Roy, M., 2013. 40Ar/39Ar hornblende provenance clues about Heinrich event 3 (H3). In: Jourdan, F., Mark, D. F. and Verati, C. (eds): Advances in 40Ar/39Ar Dating: from Archaeology to Planetary Sciences, Geological Society, London, Special Publications 378, 245-263.

Ducklow H. W., Wilson, S. E., Post, A. F., Stammerjohn, S. E., Erickson, M., Lee, S.H., Lowry, K. E., Sherrell, R. M., Yager, P. L., 2015. Particle flux on the continental shelf in the Amundsen Sea Polynya and western Antarctic Peninsula. Elem Sci Anth 3, 000046. doi:10.12952/journal.elementa.000046.

Ehrmann, W. U., Hillenbrand, C.-D., Smith, J. A., Graham, A. G. C. Kuhn, G., Larter, R. D., 2011. Provenance changes between recent and glacial-time sediments in the Amundsen Sea embayment, West Antarctica: clay mineral assemblage evidence. Antarctic Science 23 (5), 471-486.

Ehrmann, W. U., Melles, M., Kuhn, G., Grobe, H., 1992. Significance of clay mineral assemblages in the Antarctic Ocean. Marine Geology 107, 249–273.

Eisenhauer, A., Meyer, H., Rachold, V., Tütken, T., Wiegand, B., Hansen, B. T., Spielhagen, R. F., Lindemann, F., Kassens, H., 1999. Grain size separation and sediment mixing in Arctic Ocean sediments: evidence from the strontium isotope systematic. Chemical Geology 158, 173-188.

Farmer, G. L., and Licht, K., 2016. Generation and fate of glacial sediments in the central Transantarctic Mountains based on radiogenic isotopes and implications for reconstructing past ice dynamics. Quaternary Science Reviews 150, 98–109.

Farmer, G. L., Barber, D., Andrews, J., 2003. Provenance of Late Quaternary ice-proximal sediments in the North Atlantic: Nd, Sr and Pb isotopic evidence. Earth and Planetary Science Letters 209, 227-243.

Farmer, G. L., Licht, K., Swope, R. J., Andrews, J., 2006. Isotopic constraints on the provenance of fine-grained sediment in LGM tills from the Ross Embayment, Antarctica. Earth and Planetary Science Letters 249, 90-107.

Ferraccioli, F., Armadillo, E., Jordan, T., Bozzo, E., Corr, H., 2009. Aeromagnetic exploration over the East Antarctic Ice Sheet: A new view of the Wilkes Subglacial Basin. Tectonophysics 478 (1-2), 62-77.

Ferraccioli, F., Bozzo, E., Damaske, D., 2002. Aeromagnetic signatures over western Marie Byrd Land provide insight into magmatic arc basement, mafic magmatism and structure of the Eastern Ross Sea Rift flank. Tectonophysics 347, 139-165.

Ferraccioli, F., Jones, P. C., Vaughan, A. P. M., Leat, P. T., 2006. New aerogeophysical view of the Antarctic Peninsula: More pieces, less puzzle. Geophysical Research Letters 33, L05310.

Ferrando, R., Roperch, P., Morata, D., Arriagada, C., Ruffet, G., Córdova, M. L., 2014. A paleomagnetic and magnetic fabric study of the Illapel Plutonic Complex, Coastal Range, central

Chile: Implications for emplacement mechanism and regional tectonic evolution during the mid-Cretaceous. Journal of South American Earth Science 50, 12-26.

Flowerdew, M. J., Millar, I. L., Vaughan, A. P. M., Pankhurst, R. J., 2005. Age and tectonic significance of the Lassiter Coast Intrusive Suite, eastern Ellsworth Land, Antarctic Peninsula. Antarctic Science 17, 443–452, doi:10.1017/S0954102005002877.

Flowerdew, M. J., Tyrrell, S., Riley, T. R., Whitehouse, M. J., Mulvaney, R., Leat, P. T., Marschall, H. R., 2012. Distinguishing East and West Antarctic sediment sources using the Pb isotope composition of detrital K-feldspar. Chemical Geology 292–293, 88–102, doi:10.1016/j.chemgeo.2011.11.006.

Fretwell, P., et al., 2013. Bedmap2: improved ice bed, surface and thickness datasets for Antarctica. The Cryosphere 7, 375-393.

Futa, K., and LeMasurier, W. E., 1983. Nd and Sr isotopic studies on Cenozoic mafic lavas from West Antarctica - another source for continental alkali basalts. Contributions to Mineralogy and Petrology 83 (1-2), 38-44.

Gale, A., Dalton, C. A., Langmuir, C. H., Su, Y., Schilling, J. G., 2013. The mean composition of ocean ridge basalts. Geochemistry, Geophysics, Geosystems 14 (3), 489–518.

Garçon, M., Chauvel, C., France-Lanord, C., Huyghe, P., Lavé, J., 2013. Continental sedimentary processes decouple Nd and Hf isotopes, Geochimica et Cosmochimica Acta 121, 177-195. doi:10.1016/j.gca.2013.07.027.

Garzanti, E., Andò, S., Vezzoli, G., 2008. Settling-equivalence of detrital minerals and grain-size dependence of sediment composition. Earth and Planetary Science Letters 273, 138–151.

Garzanti, E., Andò, S., Vezzoli, G., 2009. Grain-size dependence of sediment composition and environmental bias in provenance studies. Earth and Planetary Science Letters 277 (3-4), 422-432.

Gladstone, R. M., Bigg, G. R., Nicholls, K. W., 2001. Iceberg trajectory modelling and meltwater injection in the Southern Ocean. Journal of Geophysical Research 106, 19903-19915.

Goldstein, S. L., and Hemming, S. R., 2003. Long-lived isotopic tracers in oceanography, paleoceanography, and ice-sheet dynamics. Treatise on Geochemistry (Oxford, Elsevier, 2003).

Gwiazda, R. H., Hemming, S. R., Broecker, W. S., 1996. Provenance of icebergs during Heinrich event 3 and the contrast to their sources during other Heinrich episodes. Paleoceanography 11 (4), 371-378.

Ha, H. K., Wåhlin, A. K., Kim, T. W., Lee, S.H., Lee, J. H., Lee, H. J., Hong, C. S., Arneborg, L., Björk, G., Kalén, O., 2014. Circulation and Modification of warm deep water on the Central Amundsen Shelf. Journal of Physical Oceanography 44 (5), 1493–1501. http://dx.doi.

org/10.1175/JPO-D-13-0240.1.

Harrison, T. M., 1982. Diffusion of 40Ar in hornblende. Contributions to Mineralogy and Petrology 78 (3), 324-331.

Harrison, T. M., Duncan, I., Dougall, I., 1985. Diffusion of 40Ar in biotite: Temperature, pressure and compositional effects. 49 (11), 2461-2468.

Hart, S. R., Blusztajn, J., LeMasurier, W. E., Rex, D. C., 1997. Hobbs Coast Cenozoic volcanism: Implications for the West Antarctic rift system. Chemical Geology 139 (1-4), 223-248.

Hathway, B., 2001. Sims Island: first data from a Pliocene alkaline volcanic centre in eastern Ellsworth Land. Antarctic Science 13 (1), 87-88.

Hemming, S. R., 2004. Heinrich events: massive late Pleistocene detritus layers of the North Atlantic and their global climate imprint. Reviews of Geophysics, 42, RG1005, doi:10.1029/2003RG000128.

Hemming, S. R., and Hajdas, I., 2003. Ice-rafted detritus evidence from Ar-40/Ar-39 ages of individual hornblende grains for evolution of the eastern margin of the Laurentide ice sheet since 43 C-14 ky. Quaternary International 99, 29-43.

Hemming, S. R., Broecker, W. S., Sharp, W. D., Bond, G. C., Gwiazda, R. H., McManus, J. F., Klas, M., Hajdas, I., 1998. Provenance of Heinrich layers in core V28-82, northeastern Atlantic: Ar-40/Ar-39 ages of ice-rafted hornblende, Pb isotopes in feldspar grains, and Nd-Sr-Pb isotopes in the fine sediment fraction. Earth and Planetary Science Letters 164 (1-2), 317-333.

Hemming, S. R., van de Flierdt, T., Goldstein, S. L., Franzese, A. M., Roy, M., Gastineau, G., Landrot, G., 2007. Strontium isotope tracing of terrigenous sediment dispersal in the Antarctic Circumpolar Current: Implications for constraining frontal positions. Geochemistry, Geophysics, Geosystems 8 (6).

Hillenbrand, C.-D., and Ehrmann, W., 2002. Distribution of clay minerals in drift sediments on the continental rise west of the Antarctic Peninsula, ODP Leg 178, Sites 1095 and 1096. In: Barker, P. F., Camerlenghi, A., Acton, G. D., Ramsay, A. T. S. (Eds.), Proc. ODP Sci. Results, 178, pp. 1 – 29. (CD-ROM). Available from: Ocean Drilling Program, Texas A&M University, College Station, TX 77845-9547, U.S.A.

Hillenbrand, C.-D., Ehrmann, W., Larter, R. D., Benetti, S., Dowdeswell, J. A., Ó Cofaigh, C., Graham, A. G. C., Grobe, H., 2009b. Clay mineral provenance of sediments in the southern Bellingshausen Sea reveals drainage changes of the West Antarctic Ice Sheet during the Late Quaternary. Marine Geology 265 (1-2), 1-18.

Hillenbrand, C.-D., Fütterer, D. K., Grobe, H., Frederichs, T., 2002. No evidence for a Pleistocene collapse of the West Antarctic Ice Sheet from continental margin sediments recovered in the Amundsen Sea. Geo-Marine Letters 22, 51–59.

Hillenbrand, C.-D., Grobe, H., Diekmann, B., Kuhn, G., Fütterer, D. K., 2003. Distribution of clay minerals and proxies for productivity in surface sediments of the Bellingshausen and Amundsen seas (West Antarctica) - Relation to modern environmental conditions. Marine Geology 193, 253-271.

Hillenbrand, C.-D., Kuhn, G., Frederichs, T., 2009a. Record of a Mid-Pleistocene depositional anomaly in West Antarctic continental margin sediments: an indicator for ice-sheet collapse? Quaternary Science Reviews 28, 1147-1159.

Hillenbrand, C.-D., Kuhn, G., Smith, J. A., Gohl, K., Graham, A. G. C., Larter, R. D., Klages, J. P., Downey, R., Moreton, S. G., Forwick, M., Vaughan, D. G., 2013. Grounding-line retreat of the West Antarctic Ice Sheet from inner Pine Island Bay. Geology 41 (1), 35-38, doi: 10.1130/G33469.1.

Hillenbrand, C.-D., Larter, R. D., Dowdeswell, J. A., Ehrmann, W., Ó Cofaigh, C., Benetti, S., Graham, A. G. C., Grobe, H., 2010a. The sedimentary legacy of a palaeo-ice stream on the shelf of the southern Bellingshausen Sea: Clues to West Antarctic glacial history during the Late Quaternary. Quaternary Science Reviews 29 (19-20), 2741-2763.

Hillenbrand, C.-D., Smith, J. A., Hodell, D. A., Greaves, M., Poole, C. R., Kender, S., Williams, M., Andersen, T. J., Jernas, P. E., Elderfield, H., Klages, J. P., Roberts, S. J., Gohl, K., Larter, R. D., Kuhn, G., 2017. West Antarctic Ice Sheet retreat drive by Holocene warm water intrusions. Nature 547, 43-48.

Hillenbrand, C.-D., Smith, J. A., Kuhn, G., Esper, O., Gersonde, R., Larter, R. D., Maher, B., Moreton, S. G., Shimmield, T. M., Korte, M., 2010b. Age assignment of a diatomaceous ooze deposited in the western Amundsen Sea Embayment after the Last Glacial Maximum. Journal of Quaternary Science, 25, 280-295.

Hofmann, E. E., Klinck, J. M., Lascara, C. M., Smith, D. A., 1996. Water Mass Distribution and Circulation West of the Antarctic Peninsula and Including Bransfield Strait, in: Ross, R. M., Hofmann, E. E., and Quetin, L. B. (eds.), Foundations for Ecological Research West of the Antarctic Peninsula, Antarctic Research Series, American Geophysical Union, Washington, D.C., 61–81.

Hole, M. J., and LeMasurier, W. E., 1994. Tectonic controls on the geochemical compositions of Cenozoic mafic alkaline volcanic rocks from West Antarctica. Contributions to Mineralogy and Petrology 117 (2), 187-202.

Holland, P. R., Jenkins, A., Holland, D. M., 2010. Ice and ocean processes in the Bellingshausen Sea, Antarctica, Journal of Geophysical Research 115, C05020, doi:10.1029/2008JC005219, 2010.

Jacobs, S. S., Giulivi, C., Dutrieux, P., Rignot, E., Nitsche, F., Mouginot, J., 2013. Getz ice shelf melting response to changes in ocean forcing. Journal of Geophysical Research 118, 4152–4168, doi:10.1002/jgrc.20298.

Jacobs, S. S., Jenkins, A., Giulivi, C. F., Dutrieux, P., 2011. Stronger ocean circulation and increased melting under Pine Island Glacier ice shelf. Nature Geoscience 4, 519-523.

Jacobsen, S. B., and Wasserburg, G. J., 1980. Sm–Nd isotopic evolution of chondrites. Earth and Planetary Science Letters 50, 139-155.

Jenkins, A., Dutrieux, P., Jacobs, S. S., McPhail, S. D., Perrett, J. R., Webb, A. T., White, D., 2010. Observations beneath Pine Island Glacier in West Antarctica and implications for its retreat. Nature Geoscience 3 (7), 468-472.

Jenkins, A., Dutrieux, P., Jacobs, S. S., Steig, E. J., Gudmundsson, G. H., Smith, J. A., Heywood, E. J., 2016. Decadal ocean forcing and Antarctic ice sheet response: Lessons from the Amundsen Sea. Oceanography 29 (4), 106-117.

Jordan, T. A., Ferraccioli, F., Armadillo E., Bozzo, E., 2013a. Crustal architecture of the Wilkes Subglacial Basin in East Antarctica, as revealed from airborne gravity data. Tectonophysics 585, 196-206.

Jordan, T. A., Ferraccioli, F., Ross, N., Corr, H. F. J., Leat, P. T., Bingham, R. G., Rippin, D. M., le Brocq, A., Siegert, M. J., 2013b. Inland extent of the Weddell Sea Rift imaged by new aerogeophysical data. Tectonophysics 585, 137-160.

Joughin, I., and Alley, R., 2011. Stability of the West Antarctic ice sheet in a warming world. Nature Geoscience 4, 506-513.

Joughin, I., Smith, B. E., Medley, B., 2014. Marine Ice Sheet Collapse Potentially Under Way for the Thwaites Glacier Basin, West Antarctica. Science 344, 735.

Katz, R. F., and Worster, M. G., 2010. Stability of ice-sheet grounding lines. Proceedings of the Royal Society A-Mathematical Physical and Engineering Sciences. 466 (2118), 1597-1620.

Kennedy, D. S., and Anderson, J. B., 1989. Glacial-marine sedimentation and Quaternary glacial history of Marguerite Bay, Antarctic Peninsula. Quaternary Research 31 (2), 255-276.

Kim, C.-S., Kim, T.-W., Cho, K.-H., Ha, H. K., Lee, S.H., Kim, H.-C., Lee, J.-H., 2016a. Variability of the Antarctic Coastal Current in the Amundsen Sea. Estuarine, Coastal and Shelf Science 181, 123-133, http://dx.doi.org/10.1016/j.ecss.2016.08.004.

Kim, I., Hahm, D., Rhe, T. S., Kim, T. W., Kim, C.-S., Lee, S. H., 2016b. The distribution of glacial meltwater in the Amundsen Sea, Antarctica, revealed by dissolved helium and neon. Journal of Geophysical Research: Oceans 121, 1654-1666.

Kim, M., Hwang, J., Kim, H., Kim, D., Yang, E., Ducklow, H. W., La, H. S., Lee, S.H., Park, J., Lee, S.H., 2015. Sinking particle flux in the sea ice zone of the Amundsen Shelf, Antarctica. Deep-Sea Research I 101, 110-117. https://doi.org/10.1016/j.dsr.2015.04.002.

Kipf, A., Mortimer, N., Werner, R., Gohl, K., van de Bogaard, P., Hauff, F., Hoernle, K., 2012. Granitoids and dykes of the Pine Island Bay region, West Antarctica. Antarctic Science 24 (5), 473-484, doi:10.1017/S0954102012000259.

Komar, P. D., Baba, J., Cui, B., 1984. Grain-size analyses of mica within sediments and the hydraulic equivalence of mica and quartz. Journal of sedimentary petrology. 54, 1379–1391.

Korhonen, F. J., Saito, S., Brown, M., Siddoway, C. S., Day, J. M. D., 2010. Multiple Generations of Granite in the Fosdick Mountains, Marie Byrd Land, West Antarctica: Implications for Polyphase Intracrustal Differentiation in a Continental Margin Setting. Journal of Petrology 51 (3), 627-670.

Kuiper, K. F., Deino, A., Hilgen, F. J., Krijgsman, W., Renne, P. R., Wijbrans, J. R., 2008. Synchronizing Rock Clocks of Earth History. Science 320 (5875), 500-504.

Lamy, F., Gersonde, R., Winckler, G., Esper, O., Jaeschke, A., Kuhn, G., Ullermann, J., Martinez-Garcia, A., Lambert, F., Kilian, R., 2014. Increased Dust Deposition in the Pacific Southern Ocean During Glacial Periods. Science 343, 403-407.

Larter, R. D., and Barker, P. F., 1991. Effects of ridge crest-trench interaction on Antarctic-Phoenix Spreading: Forces on a young subducting plate. Journal of Geophysical Research: Solid Earth 96 (B12), 19’583-19’607.

Larter, R. D., Cunningham, A. P., Barker, P. F., Gohl, K., Nitsche F. O., 2002. Tectonic evolution of the Pacific margin of Antarctica 1. Late Cretaceous tectonic reconstructions. Journal of Geophysical Research: Solid Earth 107 (B12), EPM 5-1 – EPM 5-19, doi:10.1029/2000JB000052.

Larter, R. D., et al., 2014. Reconstruction of changes in the Amundsen Sea and Bellingshausen Sea sector of the West Antarctic Ice Sheet since the Last Glacial Maximum. Quaternary Science Reviews 100, 55-86.

Leat, P. T., Scarrow, J. H., Millar, I. L., 1995. On the Antarctic Peninsula batholith. Geological Magazine 32 (4), 3990412.

Lee, J.-Y., Marti, K., Severinghaus, J. P., Kawamura, K., Yoo H.-S., Lee, J. B., Kim J. S., 2006. A redetermination of the isotopic abundances of atmospheric Ar. Geochimica et Cosmochimica Acta 70 (17), 4507-4512.

LeMasurier, W. E., and Rex, D. C., 1991, The Marie Byrd Land volcanic province and its relation to the Cainozoic West Antarctic rift system, in Tingey, R. J., ed., The geology of Antarctica: New York, Oxford University Press, p. 249–284.

Licht, K. J., and Hemming, S. R., 2017. Analysis of Antarctic glacigenic sediment provenance through geochemical and petrologic applications. Quaternary Science Reviews 164, 1-24.

Licht, K. J., and Palmer, E. F., 2013. Erosion and transport by Byrd Glacier, Antarctica during the Last Glacial Maximum. Quaternary Science Reviews 62, 32-48.

Licht, K. J., Hennessy, A. J., Welke, B. M., 2014. The U-Pb detrital zircon signature of West Antarctic ice stream tills in the Ross embayment, with implications for Last Glacial Maximum ice flow reconstructions. Antarctic Science 26 (6), 687-697.

Lindow, J., Kamp, P. J. J., Mukasa, S. B., Kleber, M., Lisker, F., Gohl, K., Kuhn, G., Spiegel, C., 2016. Exhumation history along the eastern Amundsen Sea coast, West Antarctica, revealed by low-temperature thermochronology. Tectonophysics 35, 2239-2257.

Ludwig, K. R., 2003. Isoplot 3.00: A Geochronological Toolkit for Microsoft Excel , Berkeley Geochronology Center, Berkeley, CA.

Maslanyj, M. P., and Storey, B. C., 1990. Regional Aeromagnetic Anomalies in Ellsworth Land: Crustal structure and Mesozoic microplate boundaries within West Antarctica. Tectonics 9 (6), 1515-1532.

Mazur, A. K., Wåhlin, A. K., Krężel, A., 2017. An object-based SAR image iceberg detection algorithm applied to the Amundsen Sea. Remote Sensing of Environment 189, 67-83.

McCarron, J. J., and Smellie, J. L., 1998. Tectonic implications of fore-arc magmatism and generation of high-magnesian andesites: Alexander Island, Antarctica. Journal of the Geological Society, London 155, 269-280.

McCave, I. N., Thornalley, D. J. R., Hall, I. R., 2017. Relation of sortable silt grain-size to deep-sea current speeds: Calibration of the 'Mud Current Meter'. Deep-Sea Research I 127, 1-12.

McLennan, S. M., 2001. Relationships between the trace element composition of sedimentary rocks and upper continental crust. Geochemistry, Geophysics, Geosystems 2 (4), doi:10.1029/2000GC000109.

McLennan, S. M., Hemming, S. R., McDaniel, D. K., Hanson, G. N., 1993. Geochemical approaches to sedimentation, provenance and tectonics. In: Johnsson M. J., and Basu, A. (eds), Processes Controlling the Composition of Clastic Sediments. Geological Society of America Special Paper 284.

Merino, N., Le Sommer, J., Durand, G., Jourdain, N. C., Madec, G., Mathiot, P., Tournadre, J., 2016. Antarctic icebergs melt over the Southern Ocean: Climatology and impact on sea ice. Ocean Modelling 104, 99-110.

Miles, T., Lee, S.H., Wåhlin, A., Ha, H. K., Kim, T. W., Assmann, K. M., Schofield, O., 2016. Glider observations of the Dotson Ice Shelf outflow. Deep-Sea Research II 123, 16-29.

Millar, I. L., and Pankhurst, R. J., 1987. Rb-Sr geochronology of the region between the Antarctic Peninsula and the Transantarctic Mountains: Haag Nunataks and Mesozoic granitoids. Geophysical Monograph Series 40, 151-160.

Millar, I. L., Pankhurst, R. J., Fanning, C. M., 2002. Basement chronology of the Antarctic Peninsula: recurrent magmatism and anatexis in the Palaeozoic Gondwana Margin. Journal of the Geological Society, London 159, 145-157.

Mortimer, N., Gans, P., Calvert, A., Walker, N., 1999. Geology and thermochronometry of the east edge of the Median Batholith (Median Tectonic Zone): a new perspective on Permian to Cretaceous crustal growth of New Zealand. The Island Arc 8, 404-425.

Mouginot, J., Rignot, E., Scheuchl, B., 2014. Sustained increase in ice discharge from the Amundsen Sea Embayment, West Antarctica, from 1973 to 2013. Geophysical Research Letters 41, 1576–1584.

Mukasa, S. B., and Dalziel, I. W. D., 2000. Marie Byrd Land,West Antarctica: Evolution of Gondwana's Pacific margin constrained by zircon U-Pb geochronology and feldspar common-Pb isotopic compositions. GSA Bulletin 112 (4), 611-627.

Murphy, E. J., Hofmann, E. E., Watkins, J. L., Johnston, N. M., Piñones, A., Ballerini, T., Hill, S. L., Trathan, P. N., Tarling, G. A., Cavanagh, R. A., Young, E. F., Thorpe, S. E., Fretwell, P., 2013. Comparison of the structure and function of Southern Ocean regional ecosystems: the Antarctic Peninsula and South Georgia. Journal of Marine Systems 109, 22–42.

Naish, T., et al., 2009. Obliquity-paced Pliocene West Antarctic Ice Sheet oscillations. Nature 458, 322-328.

Oppenheimer, M., 1998. Global warming and the stability of the West Antarctic Ice Sheet. Nature 393, 325-332.

Orsi, A. H., Whitworth, T., Nowlin, W. D., 1995. On the meridional extent and fronts of the Antarctic Circumpolar Current. Deep-Sea Research Part I-Oceanographic Research Papers 42 (5), 641-673.

Pankhurst, R. J., and Rowley, P. D., 1991. Rb-Sr study of Cretaceous plutons from southern Antarctic Peninsula and eastern Ellsworth Land, Antarctica. In: Thomson, M. R. A., Crame, J. A. and Thomson, J. W. (eds), Geological Evolution of Antarctica. Cambridge University Press, 1991.

Pankhurst, R. J., Hole, M. J., Brook, M., 1988. Isotope evidence for the origin of Andean granites. Royal Society of Edinburgh Transactions: Earth Sciences 79, 123-133.

Pankhurst, R. J., Millar, I. L., Grunow, A. M., Storey, B. C., 1993. The Pre-Cenozoic Magmatic History of the Thurston Island Crustal Block, West Antarctica. Journal of Geophysical Research 98 (B7), 11'835-11'849.

Pankhurst, R. J., Riley, T. R., Fanning, C. M., Kelley, S. P., 2000. Episodic Silicic Volcanism in Patagonia and the Antarctic Peninsula: Chronology of Magmatism Associated with the Break-up of Gondwana. Journal of Petrology 41 (5), 605-625.

Pankhurst, R. J., Weaver, S. D., Bradshaw, J. D., Storey, B. C., Ireland, T. R., 1998. Geochronology and geochemistry of pre-Jurassic superterranes in Marie Byrd Land, Antarctica. Journal of Geophysical Research: Solid Earth 103 (B2), 2529-2547.

Parada, M. A., Féraud, G., Fuentes, F., Aguirre, L., Morata, D., Larrondo, P., 2005. Ages and cooling history of the Early Cretaceous Caleu pluton: testimony of a switch from a rifted to a compressional continental margin in central Chile, Journal of the Geological Society of London 162, 273-287.

Payne, A. J., Vieli, A., Shepherd A. P., Wingham D. J., Rignot E., 2004. Recent dramatic thinning of largest West Antarctic ice stream triggered by oceans, Geophysical Research Letters., 31, L23401, doi:10.1029/2004GL021284.

Peck, V. L., Hall, I. R., Zahn, R., Grousset, F., Hemming, S. R., Scourse, J. D., 2007. The relationship of Heinrich events and their European precursors over the past 60 ka BP: a multi-proxy ice-rafted debris provenance study in the North East Atlantic. Quaternary Science Reviews 26 (7-8), 862-875.

Pierce, E. L., Hemming, S. R., Williams, T., van de Flierdt, T., Thomson, S. N., Reiners, P. W., Gehrels G. E., Brachfeld, S. A., Goldstein, S. L., 2014. A comparison of detrital U–Pb zircon, 40Ar/39Ar hornblende, 40Ar/39Ar biotite ages in marine sediments off East Antarctica: Implications for the geology of subglacial terrains and provenance studies. Earth-Science Reviews 138, 156-178.

Pierce, E. L., van de Flierdt, T., Williams, T., Hemming, S. R., Cook, C. P., Passchier, S., 2017. Evidence for a dynamic East Antarctic ice sheet during the mid-Miocene climate transition. Earth and Planetary Science Letters 478, 1-13. https://doi.org/10.1016/j.epsl.2017.08.011.

Pierce, E. L., Williams, T., van de Flierdt, T., Hemming, S. R., Goldstein, S. L., Brachfeld, S. A., 2011. Characterizing the sediment provenance of East Antarctica's weak underbelly: The Aurora and Wilkes sub-glacial basins. Paleoceanography 26, doi:10.1029/2011PA002127.

Pin, C., and Bassin, C., 1992. Evaluation of a strontium-specific extraction chromatographic method for isotopic analysis in geological-materials. Analytica Chimica Acta 269 (2), 249-255.

Pin, C., and Zalduegui, J. F. S., 1997. Sequential separation of light rare-earth elements, thorium and uranium by miniaturized extraction chromatography: Application to isotopic analyses of silicate rocks. Analytica Chimica Acta 339 (1-2), 79-89.

Pollard, D., and DeConto, R. M., 2009. Modelling West Antarctic Ice Sheet growth and collapse through the past five million years. Nature 458, 329-332.

Pritchard, H. D., Arthern, R. J., Vaughan, D. G., Edwards, L. A., 2009. Extensive dynamic thinning on the margins of the Greenland and Antarctic ice sheets. Nature 461, 971-975.

Pritchard, H. D., Ligtenberg, S., Fricker, H., Vaughan, D., van den Broeke, M. R., Padman, L., 2012. Antarctic ice-sheet loss driven by basal melting of ice shelves. Nature 484 (7395), 502–505.

Pudsey, C. J., and Camerlenghi, A., 1998. Glacial–interglacial deposition on a sediment drift on the Pacific margin of the Antarctic Peninsula. Antarctic Science 10 (3), 286-308.

Randall-Goodwin, E., Meredith, M. P., Jenkins, A., Yager, P. L., Sherrell, R. M., Abrahamsen, E. P., Guerrero, R., Yuan, X., Mortlock, R. A., Gavahan, K., Alderkamp, A.-C., Ducklow, H., Robertson, R., Stammerjohn, S. E., 2015. Freshwater distributions and water mass structure in the Amundsen Sea Polynya region, Antarctica, Elem Sci Anth 3 (1), 000065. doi: 10.12952/journal.elementa.000065.

Reyes, A. V., Carlson, A. E., Beard, B. L., Hatfield, R. G., Stoner, J. S., Winsor, K., Welke, B., Ullman, D. J., 2014. South Greenland ice-sheet collapse during Marine Isotope Stage 11. Nature 510, 525-528.

Richard, S. M., Smith, C. H., Kimbrough, D. L., Fitzgerald, P. G., Luyendyk, B. P., McWilliams, M. O., 1994. Cooling History of the Northern Ford Ranges, Marie Byrd Land, West Antarctica. Tectonics 13 (4), 837-857.

Rickli, J., Gutjahr, M., Vance, D., Fischer Gödde, M., Hillenbrand, C.-D., Kuhn, G., 2014. Neodymium and hafnium boundary contributions to seawater along the West Antarctic continental margin. Earth and Planetary Science Letters 394, 99-110.

Rignot, E., and Jacobs, S. S., 2002. Rapid Bottom Melting Widespread near Antarctic Ice Sheet Grounding Lines. Science 296, 2020-2023.

Rignot, E., Bamber, J. L., van den Broeke, M. R., Davis, C., Li, Y., van de Berg, W. J., van Meijgaard, E., 2008. Recent Antarctic ice mass loss from radar interferometry and regional climate modelling. Nature Geoscience 1, 106-110.

Rignot, E., Mouginot, J., Morlighem, M., Seroussi, H., Scheuchl, B., 2014. Widespread, rapid grounding line retreat of Pine Island, Thwaites, Smith, and Kohler glaciers, West Antarctica, from 1992 to 2011. Geophysical Research Letters 41, 3'502-3'509.

Riley, T. R., Flowerdew, M. J., Pankhurst, R. J., Leat, P. T., Millar, I. L., Fanning, C. M., Whitehouse, M. J., 2017. A revised geochronology of Thurston Island, West Antarctica, and correlations along the proto-Pacific margin of Gondwana. Antarctic Science 29 (1), 47-60.

Riley, T. R., Leat, P. T., Kelley, S. P., Millar, I. L., Thirlwall, M. F., 2003. Thinning of the Antarctic Peninsula lithosphere through the Mesozoic: evidence from Middle Jurassic basaltic lavas. Lithos 67 (3-4), 163-179.

Riley, T. R., Leat, P. T., Pankhurst, R. J., Harris, C., 2001. Origins of Large Volume Rhyolitic Volcanism in the Antarctic Peninsula and Patagonia by Crustal Melting. Journal of Petrology 42 (6), 1043-1065.

Roy, M., van de Flierdt, T., Hemming, S. R., Goldstein, S. L., 2007. (40)Ar/(39)Ar ages of hornblende grains and bulk Sm/Nd isotopes of circum-Antarctic glacio-marine sediments: Implications for sediment provenance in the Southern Ocean. Chemical Geology 244 (3-4), 507-519.

Rutberg, R. L., Hemming, S. R., Goldstein, S. L., 2000. Reduced North Atlantic Deep Water flux to the glacial Southern Ocean inferred from neodymium isotope ratios. Nature, 405, 935-938.

Ryan, C. J., 2005. Mesozoic to Cenozoic igneous rocks from Northwestern Graham Land: constraints on the tectonomagmatic evolution of the Antarctic Peninsula. PhD thesis, University of Brighton.

Scherer, R. P., Aldahan, A., Tulaczyk, S., Possnert, G., Engelhardt, H., Kamb, B., 1998. Pleistocene Collapse of the West Antarctic Ice Sheet. Science 281 (5373), 82-85.

Schoof, C., 2007. Ice sheet grounding line dynamics: Steady states, stability, and hysteresis. Journal of Geophysical Research 112, 133-138.

Shepherd, A., et al., 2012. A reconciled estimate of ice-sheet mass balance. Science, 338, 1183–1189.

Smellie, J. L., 1999. Lithostratigraphy of Miocene-Recent, alkaline volcanic fields in the Antarctic Peninsula and eastern Ellsworth Land. Antarctic Science 11 (3), 362-378.

Smith, A. M., Jordan, T. A., Ferraccili, F., Bingham, R. G., 2013. Influence of subglacial conditions on ice stream dynamics: Seismic and potential field data from Pine Island Glacier, West Antarctica. Journal of Geophysical Research: Solid Earth 118, 1471-1482.

Smith, A. M., Vaughan, D. G., Doake, C. S. M., Johnson, A. C., 1999. Surface Lowering of the Ice Ramp at Rothera Point, Antarctic Peninsula, in Response to Regional Climate Change, Annals of Glaciology 27, 113–118.

Smith, J. A., Andersen, T. J., Shortt, M., Gaffney, A. M., Truffer, M., Stanton, T. P., Bindschadler, R., Dutrieux, P., Jenkins, A., 2017. Sub-ice-shelf sediments record history of twentieth-century retreat of Pine Island Glacier. Nature 541, 77-80.

Smith, J. A., Hillenbrand, C.-D., Kuhn, G., Klages, J. P., Graham A. G. C., 2014. New constraints on the timing of West Antarctic Ice Sheet retreat in the eastern Amundsen Sea since the Last Glacial Maximum. Global and Planetary Change 122, 224-237.

Smith, J. A., Hillenbrand, C.-D., Kuhn, G., Larter, R. D., Graham, A. G. C., Ehrmann, W., Moreton, S. G., Forwick, M., 2011. Deglacial history of the West Antarctic Ice Sheet in the western Amundsen Sea Embayment. Quaternary Science Reviews 30, 488-505.

Sokolov, S., and Rintoul, S. R., 2009. Circumpolar structure and distribution of the Antarctic Circumpolar Current fronts: 1. Mean circumpolar paths. Journal of Geophysical Research 114, C11018, doi: 10.1029/2008JC005108.

Spiegel, C., Lindow, J., Kamp, P. J. J., Meisel, O., Mukasa, S. B., Lisker, F., Kuhn, G., Gohl, K., 2016. Tectonomorphic evolution of Marie Byrd Land – Implications for Cenozoic rifting activity and onset of West Antarctic glaciation. Global and Planetary Change 145, 98-115.

Stammerjohn, S. E., Maksym, T., Massom, R. A. A., Lowry, K. E., Arrigo, K. R., Yuan, X., Raphael, M., Randall-Goodwin, E., Sherrell, R. M., Yager, P. L., 2015. Seasonal sea ice changes in the Amundsen Sea, Antarctica, over the period of 1979–2014. Elem Sci Anth 3, doi:10.12952/journal.elementa.000055.

Storey, B. C., Dalziel, I. W. D., Garrett, S. W., Grunow, A. M, Pankhurst, R. J., Vennum, W. R., 1988. West Antarctica in Gondwanaland: Crustal blocks, reconstruction and breakup processes. Tectonophysics 155, 381-390.

Storey, B. C., Vaughan, A. P. M., Millar, I. L., 1996. Geodynamic evolution of the Antarctic Peninsula during Mesozoic times and its bearing on Weddell Sea history. Geological Society, London, Special Publications 108, 87-103.

Struve, T., van de Flierdt T., Burke, A., Robinson, L. F., Hammond, S. J., Crocket, K. C., Bradtmiller, L. I., Auro, M. E., Mohamed, K. J., White, N. J., 2016. Neodymium isotopes and concentrations in aragonitic scleractinian cold-water coral skeletons - Modern calibration and evaluation of palaeo-applications. Chemical Geology 453, 146-168.

Tanaka, T., Togashi, S., Kamioka, H., Amakawa, H., Kagami, H., Hamamoto, T., Yuhara, M., Orihashi, Y., Yoneda, S., Shimizu, H., Kunimaru, T., Takahashi, K., Yanagi, T., Nakano, T., Fujimaki, H., Shinjo, R., Asahara, Y., Tanimizu, M., Dragusanu, C., 2000. JNdi-1: a neodymium isotopic reference in consistency with LaJolla neodymium. Chemical Geology 168 (3-4), 279-281.

Taylor, S. R., and McLennan, S. M., 1995. The geochemical evolution of the continental crust. Reviews of Geophysics 33 (2), 241-265.

Taylor, S. R., and McLennan, S. M., 2001. Chemical composition and element distribution in the Earth's crust. In: Encyclopedia of Physical Science and Technology, New York: Academic Press.

The RAISED Consortium, et al., 2014. A community-based geological reconstruction of Antarctic Ice Sheet deglaciation since the Last Glacial Maximum. Quaternary Science Reviews 100, 1-9.

Thoma, M., Jenkins, A., Holland, D., Jacobs, S., 2008. Modelling Circumpolar Deep Water intrusions on the Amundsen Sea continental shelf, Antarctica, Geophysical Research Letters 35, L18602. doi:10.1029/2008GL034939.

Tournadre, J., Bouhier, N., Girard-Ardhuin, F., Rémy, F., 2016. Antarctic icebergs distribution 1992–2014. Journal Geophysical Research 121 (1), 327-349.

Tucholke, B. E., Hollister, C. D., Weaver, F. M., Vennum, W. R., 1976. Continental rise and abyssal plain sedimentation in the Southeast Pacific Basin — leg 35 Deep Sea Drilling Project. In: Hollister, C. D., Craddock, C., et al. (eds.), Initial Reports of the Deep Sea Drilling Project 35, 291-300.

Turner, J., Orr, A., Gudmundsson, G. H., Jenkins, A., Bingham, R. G., Hillenbrand, C.-D., Bracegirdle, T. J., 2017. Atmosphere-ocean-ice interactions in the Amundsen Sea Embayment, West Antarctica. Reviews of Geophysics 55, doi:10.1002/2016RG000532.

Underwood, M. B., and Pickering, K. T., 1996. Clay-mineral provenance, sediment dispersal patterns, and mudrock diagenesis in the Nankai accretionary prism, southwest Japan. Clays and Clay Minerals 44 (3), 339-356.

van de Flierdt, T., Hemming, S. R., Goldstein, S. L., Gehrels, G., Cox, S. E., 2008. Evidence against a young volcanic origin of the Gamburtsev Subglacial Mountains, Antarctica. Geophysical Research Letters: Solid Earth 35 (21), L21303, doi: 10.1029/2008GL035564.

van de Flierdt, T., Goldstein, S. L., Hemming, S. R., Roy, M., Frank, M., Halliday, A. N., 2007. Global neodymium-hafnium isotope systematics – revisited. Earth and Planetary Science Letters 259 (3-4), 432-441.

Vaughan, A. P. M., and Storey, B. C., 2000. The eastern Palmer Land shear zone: a new terrane accretion model for the Mesozoic development of the Antarctic Peninsula. Journal of the Geological Society 157, 1243-1256.

Vaughan, A. P. M., Eagles, G., Flowerdew, M. J., 2012a. Evidence for a two-phase Palmer Land event from crosscutting structural relationships and emplacement timing of the Lassiter Coast Intrusive Suite, Antarctic Peninsula: Implications for mid-Cretaceous Southern Ocean plate configuration. Tectonics 31, TC1010.

Vaughan, A. P. M., Storey, B. C., Kelley, S. P., Barry, T. L., Curtis, M. L., 2012b. Synkinematic emplacement of Lassiter Coast Intrusive Suite plutons during the Palmer Land Event: evidence for mid-Cretaceous sinistral transpression at the Beaumont Glacier in eastern Palmer Land. Journal of the Geological Society 169, 759-771.

Vaughan, A. P. M., Wareham, C. D., Johnson, A. C., Kelley, S. P., 1998. A Lower Cretaceous, syn-extensional magmatic source for a linear belt of positive magnetic anomalies: the Pacific Margin Anomaly (PMA), western Palmer Land, Antarctica. Earth and Planetary Science Letters 158, 143-155.

Vaughan, D. G., Barnes, D. K. A., Fretwell, P. T., Bingham, R. G., 2011. Potential seaways across West Antarctica. Geochemistry, Geophysics, Geosystems 12 (10), Q10004, doi:10.1029/2011GC003688.

Veevers, J. J., and Saeed, A., 2013. Age and composition of Antarctic sub-glacial bedrock reflected by detrital zircons, erratics, and recycled microfossils in the Ellsworth Land–Antarctic Peninsula–Weddell Sea–Dronning Maud Land sector (240°E–0°–015°E). Gondwana Research 23, 296-332.

Wåhlin, A. K., Kalén, O., Arneborg, L., Björk, G., Carvajal, G. K., Ha, H. K., Kim, T. W., Lee, S.H., Stranne, C., 2013. Variability of warm deep water inflow in a submarine trough on the Amundsen Sea shelf, Journal of Physical Oceanography 43, 2054–2070.

Wåhlin, A. K., Kalén, O., Assmann, K., Darelius, E., Ha, H. K., Lee, S.H., 2016. Sub-inertial oscillations on the central Amundsen Shelf, Journal of Physical Oceanography 46 (9), 2573-2582, https://doi.org/10.1175/JPO-D-14-0257.1

Wåhlin, A. K., Muench, R. D., Arneborg, L., Björk, G., Ha, H. K., Lee, S. H., Alsén, H., 2012. Some implications of Ekman layer dynamics for cross-shelf exchange in the Amundsen Sea. Journal of Physical Oceanography 42 (9), 1461-1474.

Wåhlin, A. K., Yuan, X., Björk, G., Nohr, C., 2010. Inflow of warm Circumpolar Deep Water in the Central Amundsen Shelf, Journal of Physical Oceanography 40 (6), 1427–1434.

Walker, D. P., Brandon, M. A., Jenkins, A., Allen, J. T., Dowdeswell, J. A., Evans, J., 2007. Oceanic heat transport onto the Amundsen Sea shelf through a submarine glacial trough. Geophysical Research Letters 34, L02602.

Walker, D. P., Jenkins, A., Assmann, K., Shoosmith, D. R., Brandon, M. A., 2013. Oceanographic observations at the shelf break of the Amundsen Sea, Antarctica. Journal of Geophysical Research: Oceans 118, 2906-2918.

Walter, H. J., Hegner, E., Diekmann, B., Kuhn, G., Rutgers van der Loeff, M. M., 2000. Provenance and transport of terrigenous sediment in the South Atlantic Ocean and their relations to glacial and interglacial cycles: Nd and Sr isotopic evidence. Geochimica et Cosmochimica Acta 64 (22), 3814-3827.

Weaver, S. D., Adams, C. J., Pankhurst, R. J., Gibson, I. L., 1992. Granites of Edward VII Peninsula, Marie Byrd Land: anorogenic magmatism related to Antarctic-New Zealand rifting. Transactions of the Royal Society of Edinburgh: Earth Sciences 83 (1-2), 281-290.

Weis, D., Kieffer, B., Maerschalk, C., Barling, J., de Jong, J., Williams, G. A., Hanano, D., Pretorius, W., Mattielli, N., Scoates, J. S., Goolaerts, A., Friedman, R. M., Mahoney, J. B., 2006. High-precision isotopic characterization of USGS reference materials by TIMS and MC-ICP-MS. Geochemistry, Geophysics, Geosystems 7 (8). doi:10.1029/2006GC001283.

Welke, B., Licht, K., Hennessy, A., Hemming, S. R., Pierce Davis, E. L., Kassab, C., 2016. Applications of detrital geochronology and thermochronology from glacial deposits to the Paleozoic and Mesozoic thermal history of the Ross Embayment, Antarctica. Geochemistry, Geophysics, Geosystems 17, 2762-2780.

Wendt, A. S., Vaughan, A. P. M., Tate, A., 2008. Metamorphic rocks in the Antarctic Peninsula region. Geological Magazine 145 (5), 1-22.

Williams, T., van de Flierdt, T., Hemming, S. R., Chung, E., Roy, M., Goldstein, S. L., 2010. Evidence for iceberg armadas from East Antarctica in the Southern Ocean during the late Miocene and early Pliocene. Earth and Planetary Science Letters 290 (3-4), 351-361.

Wise, M. G., Dowdeswell, J. A., Jakobsson, M., Larter, R. D., 2017. Evidence of marine ice-cliff instability in Pine Island Bay from iceberg-keel plough marks. Nature 550, 506, doi: 10.1038/nature24458.

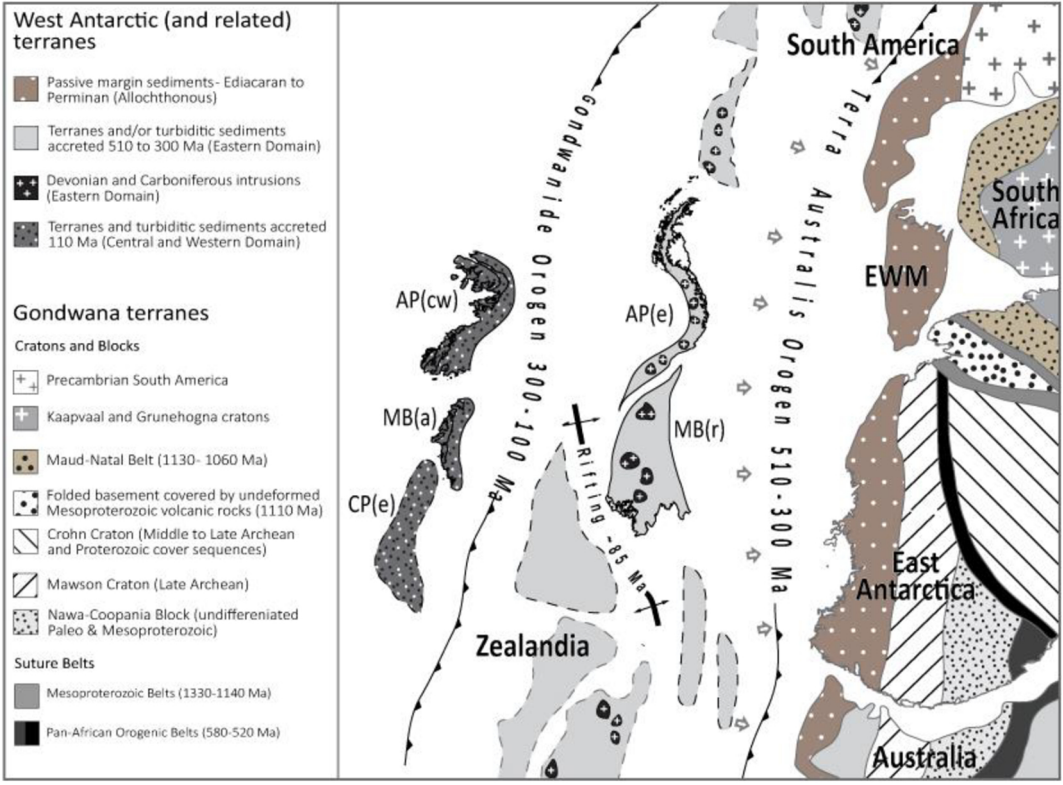
West Antarctic (and related) terranes
Passive margin sediments- Ediacaran to Perminan (Allochthonous)
Terranes and/or turbiditic sediments accreted 510 to 300 Ma (Eastern Domain)
Devonian and Carboniferous intrusions (Eastern Domain)
Terranes and turbiditic sediments accreted 110 Ma (Central and Western Domain)
Gondwana terranes
Cratons and Blocks
Precambrian South America
Kaapvaal and Grunehogna cratons
Maud-Natal Belt (1130- 1060 Ma)
Folded basement covered by undeformed Mesoproterozoic volcanic rocks (1110 Ma)
Crohn Craton (Middle to Late Archean and Proterozoic cover sequences)
Mawson Craton (Late Archean)
Nawa-Coopania Block (undifferenciated Paleo & Mesoproterozoic)
Suture Belts
Mesoproterozoic Belts (1330-1140 Ma)
Pan-African Orogenic Belts (580-520 Ma)
South America
South Africa
EWM
East Antarctica
Australia
Zealandia
AP(cw)
AP(e)
MB(a)
MB(r)
CP(e)
Rifting ~85 Ma
Gondwanide Orogen 300-100 Ma
Terra Australis Orogen 510-300 Ma

Figure 1

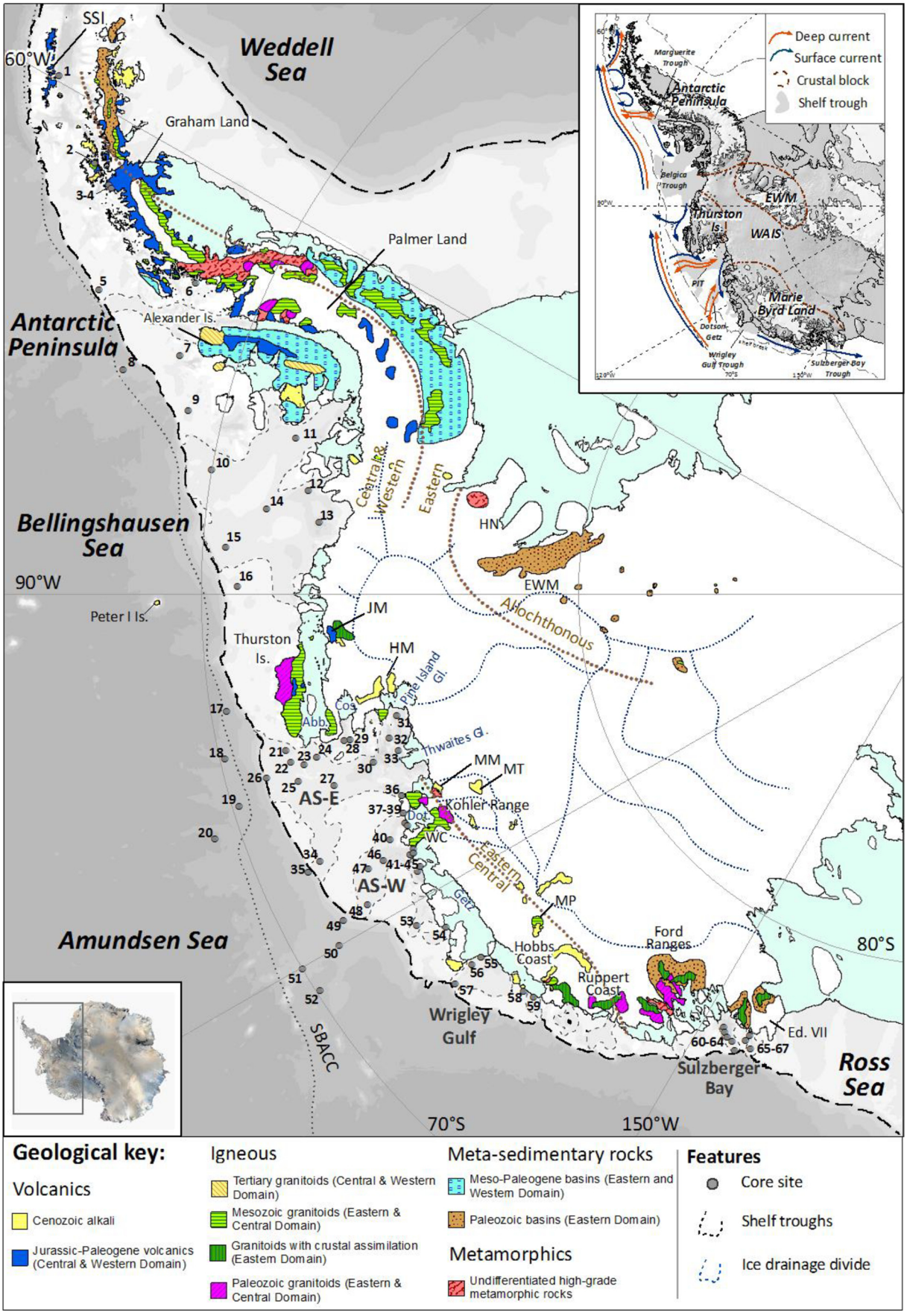
Weddell Sea
Graham Land
Palmer Land
Antarctic Peninsula
Alexander Is.
SSI
60°W
Bellingshausen Sea
90°W
Peter I Is.
Thurston Is.
Amundsen Sea
Central & Western
Eastern
HN
EWM
Allochthonous
JM
HM
Pine Island Gl.
Abb
Cos
Thwaites Gl.
MM
MT
Kohler Range
Dot
WC
AS-E
AS-W
Eastern Central
Getz
MP
Hobbs Coast
Ruppert Coast
Ford Ranges
Wrigley Gulf
SBACC
Ed. VII
Sulzberger Bay
Ross Sea
80°S
70°S
150°W
Deep current
Surface current
Crustal block
Shelf trough
Marguerite Trough
Antarctic Peninsula
Belgica Trough
Thurston Is.
EWM
WAIS
PIT
Marie Byrd Land
Dotson
Getz
Wrigley Gulf Trough
Sulzberger Bay Trough
Geological key:
Volcanics
Cenozoic alkali
Jurassic-Paleogene volcanics (Central & Western Domain)
Igneous
Tertiary granitoids (Central & Western Domain)
Mesozoic granitoids (Eastern & Central Domain)
Granitoids with crustal assimilation (Eastern Domain)
Paleozoic granitoids (Eastern & Central Domain)
Meta-sedimentary rocks
Meso-Paleogene basins (Eastern and Western Domain)
Paleozoic basins (Eastern Domain)
Metamorphics
Undifferentiated high-grade metamorphic rocks
Features
Core site
Shelf troughs
Ice drainage divide

Figure 2

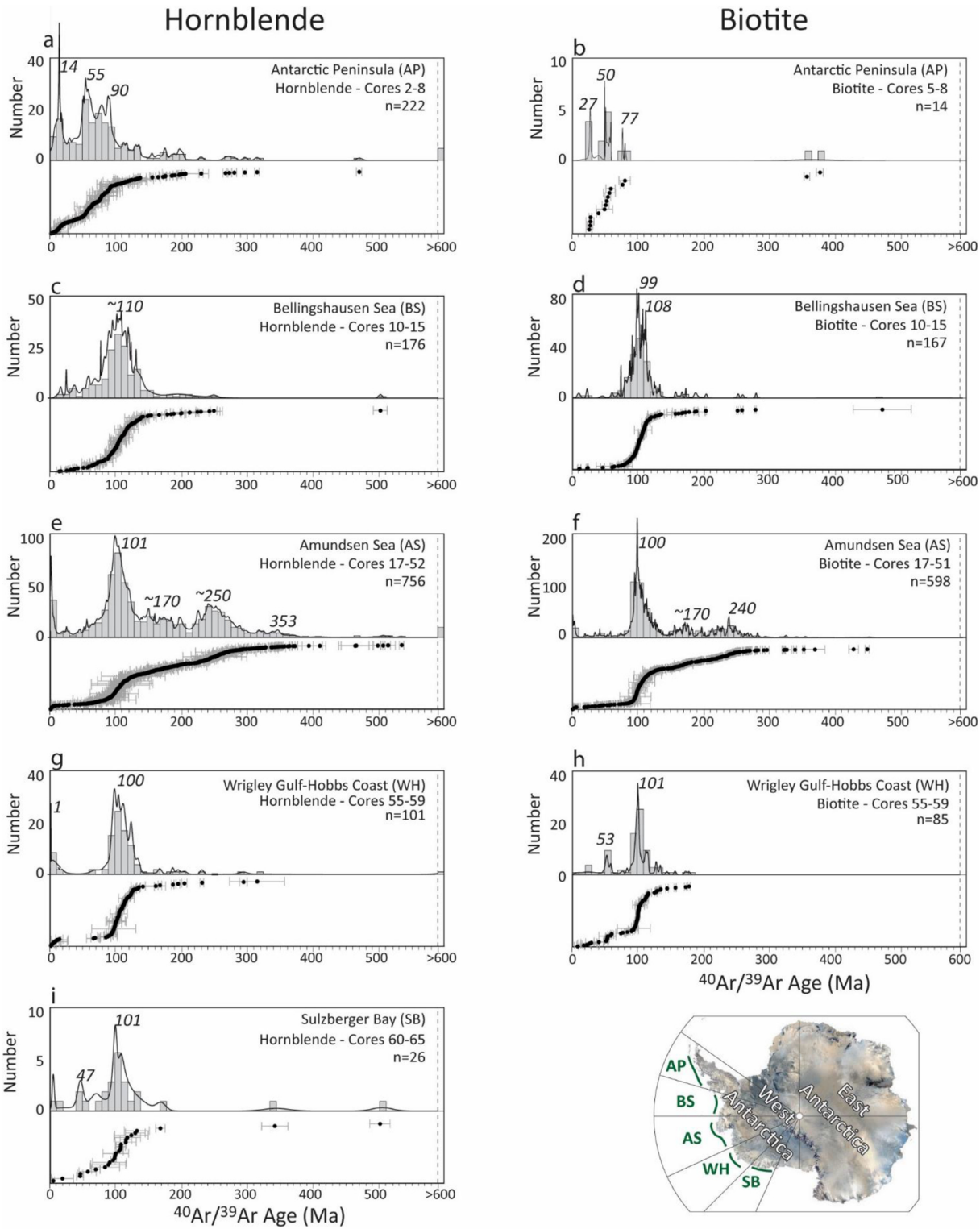
Hornblende
Biotite
a
Antarctic Peninsula (AP)
Hornblende - Cores 2-8
n=222
14
55
90
b
Antarctic Peninsula (AP)
Biotite - Cores 5-8
n=14
50
27
77
c
Bellingshausen Sea (BS)
Hornblende - Cores 10-15
n=176
~110
d
Bellingshausen Sea (BS)
Biotite - Cores 10-15
n=167
99
108
e
Amundsen Sea (AS)
Hornblende - Cores 17-52
n=756
101
~170
~250
353
f
Amundsen Sea (AS)
Biotite - Cores 17-51
n=598
100
~170
240
g
Wrigley Gulf-Hobbs Coast (WH)
Hornblende - Cores 55-59
n=101
100
1
h
Wrigley Gulf-Hobbs Coast (WH)
Biotite - Cores 55-59
n=85
101
53
i
Sulzberger Bay (SB)
Hornblende - Cores 60-65
n=26
101
47
Number
0
100
200
300
400
500
>600
600
$^{40}Ar/^{39}Ar$ Age (Ma)
AP
BS
AS
WH
SB
West Antarctica
East Antarctica

Figure 3

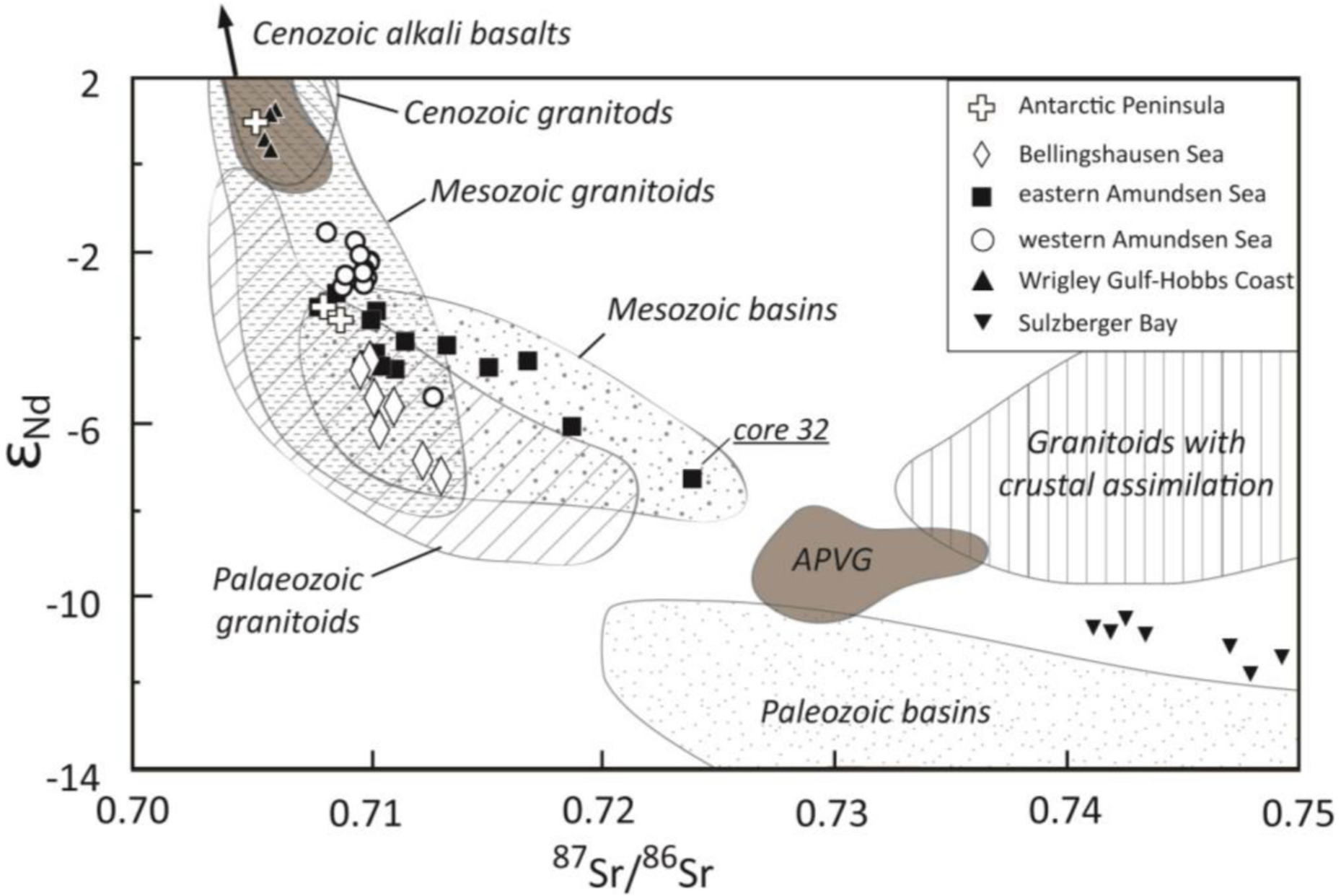
Cenozoic alkali basalts
Cenozoic granitods
Mesozoic granitoids
Mesozoic basins
core 32
Palaeozoic granitoids
APVG
Granitoids with crustal assimilation
Paleozoic basins
Antarctic Peninsula
Bellingshausen Sea
eastern Amundsen Sea
western Amundsen Sea
Wrigley Gulf-Hobbs Coast
Sulzberger Bay
εNd
2
-2
-6
-10
-14
0.70
0.71
0.72
0.73
0.74
0.75
87Sr/86Sr

Figure 4

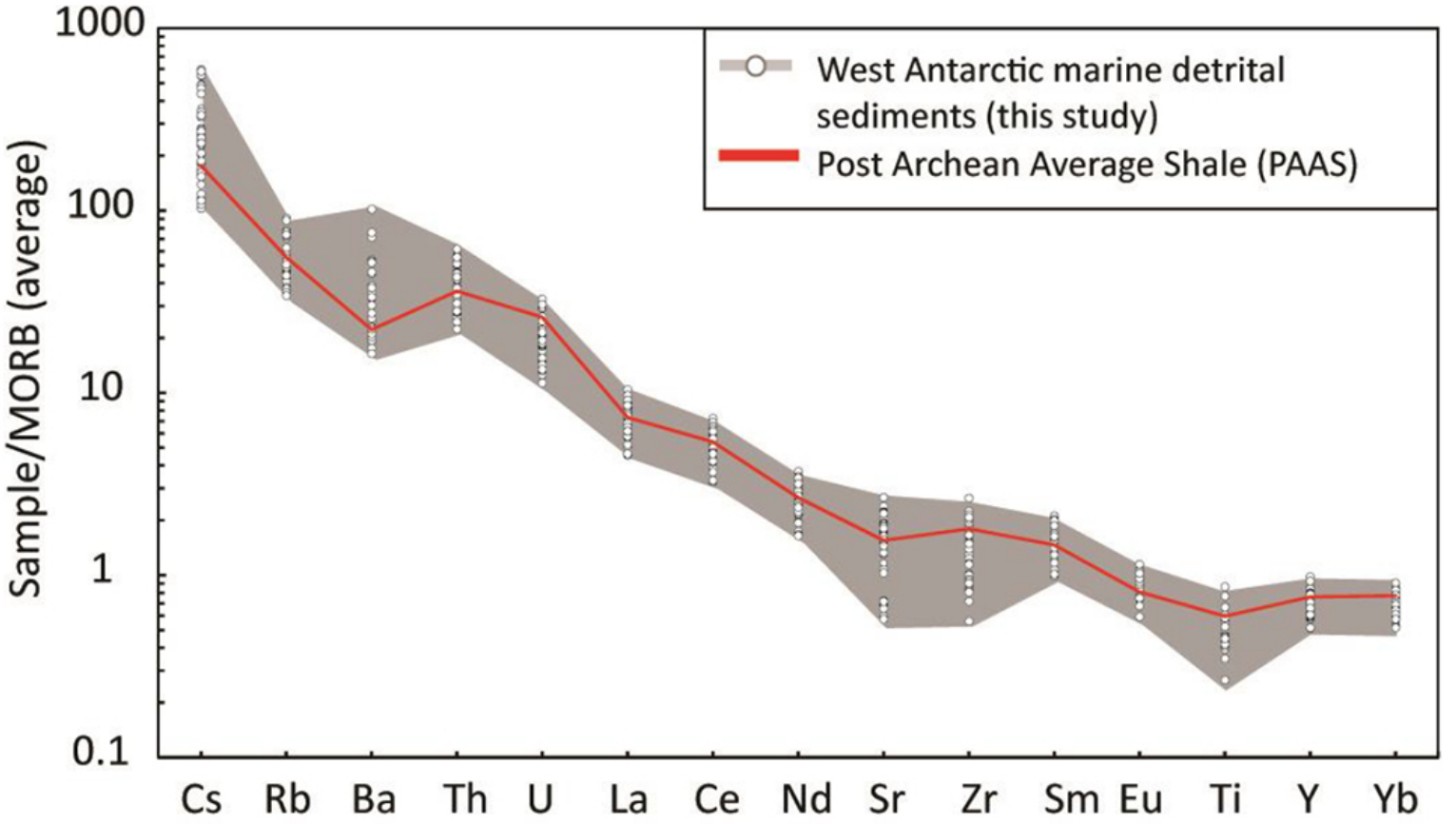
1000
100
10
1
0.1
Sample/MORB (average)
West Antarctic marine detrital sediments (this study)
Post Archean Average Shale (PAAS)
Cs Rb Ba Th U La Ce Nd Sr Zr Sm Eu Ti Y Yb

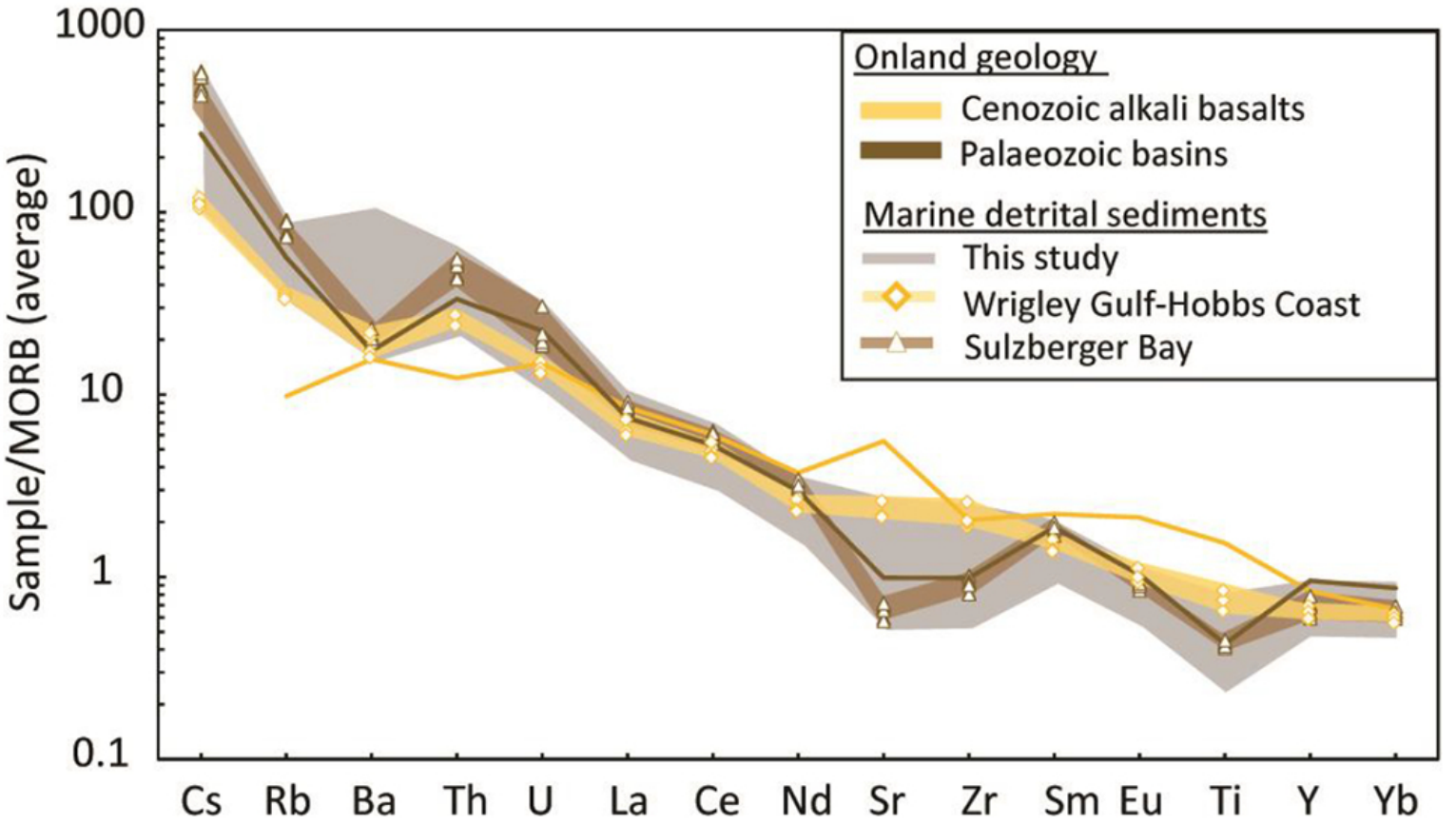
1000
100
10
1
0.1
Sample/MORB (average)
Onland geology
Cenozoic alkali basalts
Palaeozoic basins
Marine detrital sediments
This study
Wrigley Gulf-Hobbs Coast
Sulzberger Bay
Cs Rb Ba Th U La Ce Nd Sr Zr Sm Eu Ti Y Yb

Figure 5

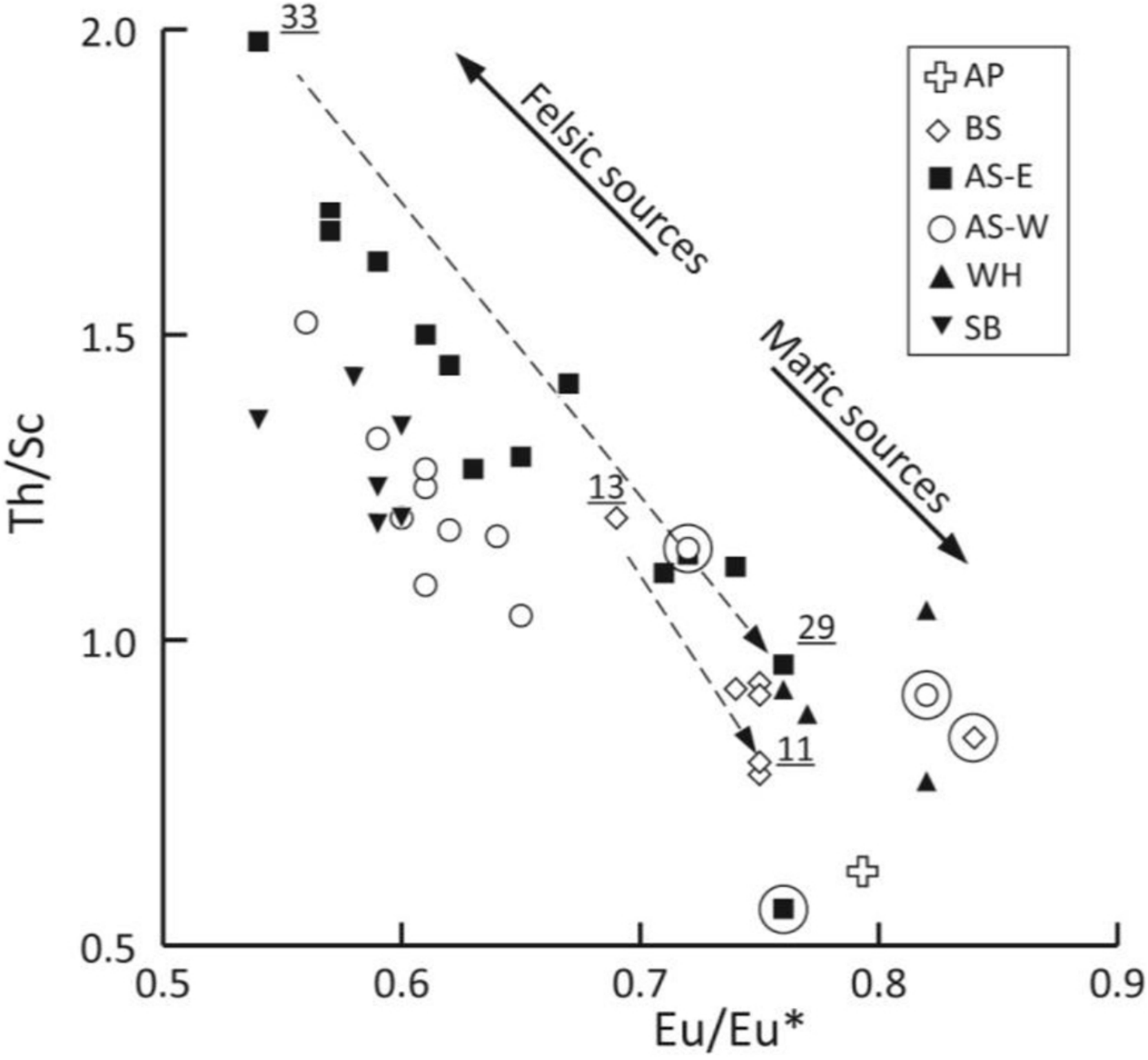
2.0
1.5
1.0
0.5
Th/Sc
0.5
0.6
0.7
0.8
0.9
Eu/Eu*
33
13
29
11
Felsic sources
Mafic sources
AP
BS
AS-E
AS-W
WH
SB

Figure 6

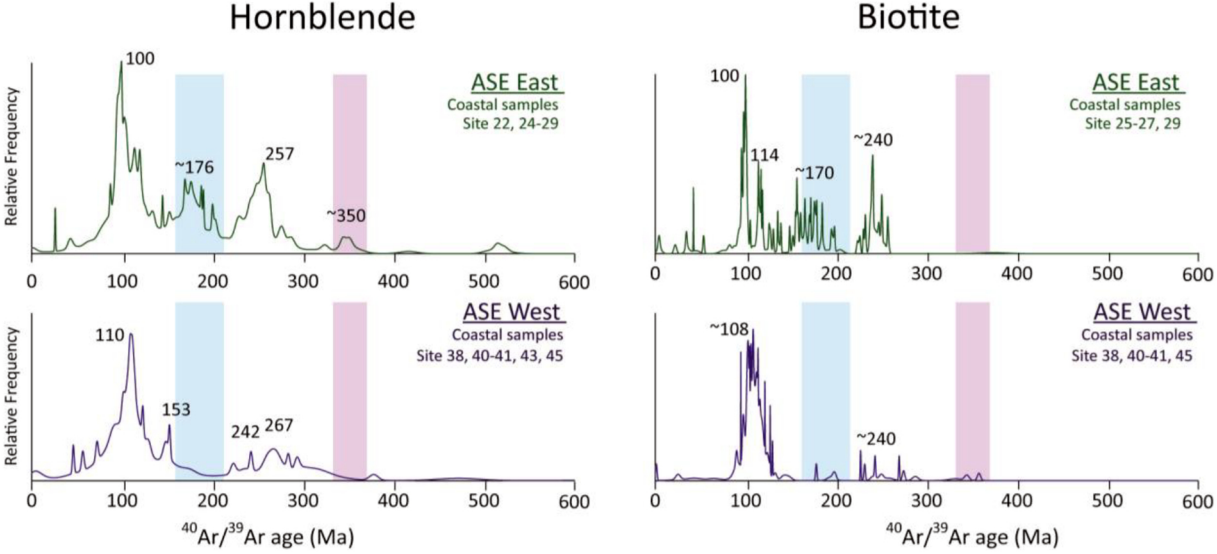
Hornblende
Biotite
ASE East
Coastal samples
Site 22, 24-29
ASE East
Coastal samples
Site 25-27, 29
ASE West
Coastal samples
Site 38, 40-41, 43, 45
ASE West
Coastal samples
Site 38, 40-41, 45
Relative Frequency
Relative Frequency
100
~176
257
~350
100
114
~170
~240
110
153
242
267
~108
~240
0
100
200
300
400
500
600
40Ar/39Ar age (Ma)
40Ar/39Ar age (Ma)

Figure 7

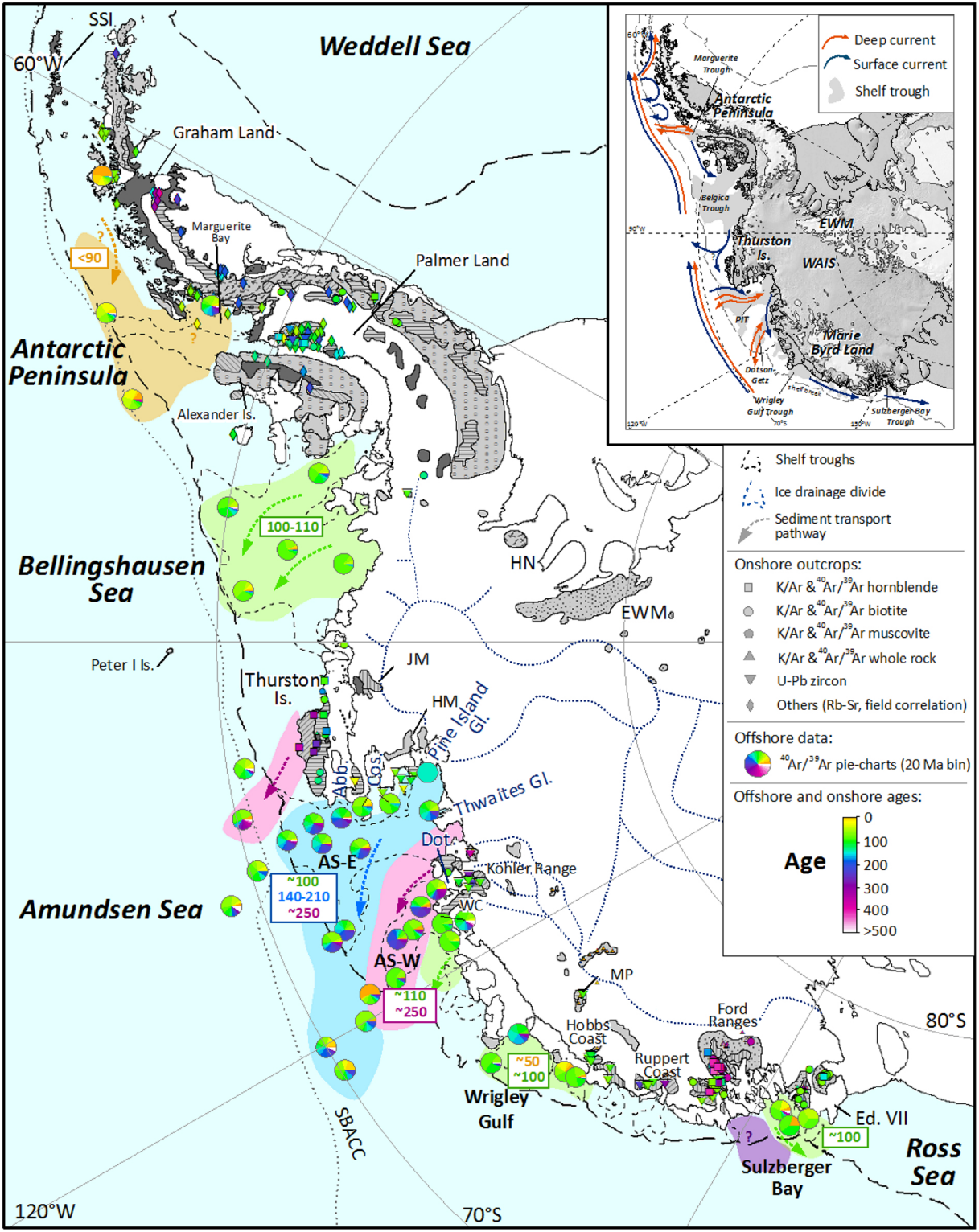
Weddell Sea
SSI
60°W
Graham Land
Marguerite Bay
Palmer Land
<90
Antarctic Peninsula
Alexander Is.
100-110
Bellingshausen Sea
Peter I Is.
Thurston Is.
JM
HM
HN
EWM
Pine Island Gl.
Abbot
Cosgrove
Thwaites Gl.
Dot
AS-E
~100
140-210
~250
Amundsen Sea
Kohler Range
WC
AS-W
~110
~250
MP
Hobbs Coast
Ruppert Coast
Ford Ranges
80°S
~50
~100
Wrigley Gulf
SBACC
Ed. VII
~100
Sulzberger Bay
Ross Sea
120°W
70°S
Deep current
Surface current
Shelf trough
Marguerite Trough
Antarctic Peninsula
Belgica Trough
EWM
Thurston Is.
WAIS
PIT
Marie Byrd Land
Dotson-Getz
Wrigley Gulf Trough
Sulzberger Bay Trough
Shelf troughs
Ice drainage divide
Sediment transport pathway
Onshore outcrops:
K/Ar & 40Ar/39Ar hornblende
K/Ar & 40Ar/39Ar biotite
K/Ar & 40Ar/39Ar muscovite
K/Ar & 40Ar/39Ar whole rock
U-Pb zircon
Others (Rb-Sr, field correlation)
Offshore data:
40Ar/39Ar pie-charts (20 Ma bin)
Offshore and onshore ages:
Age
0
100
200
300
400
>500

Figure 8

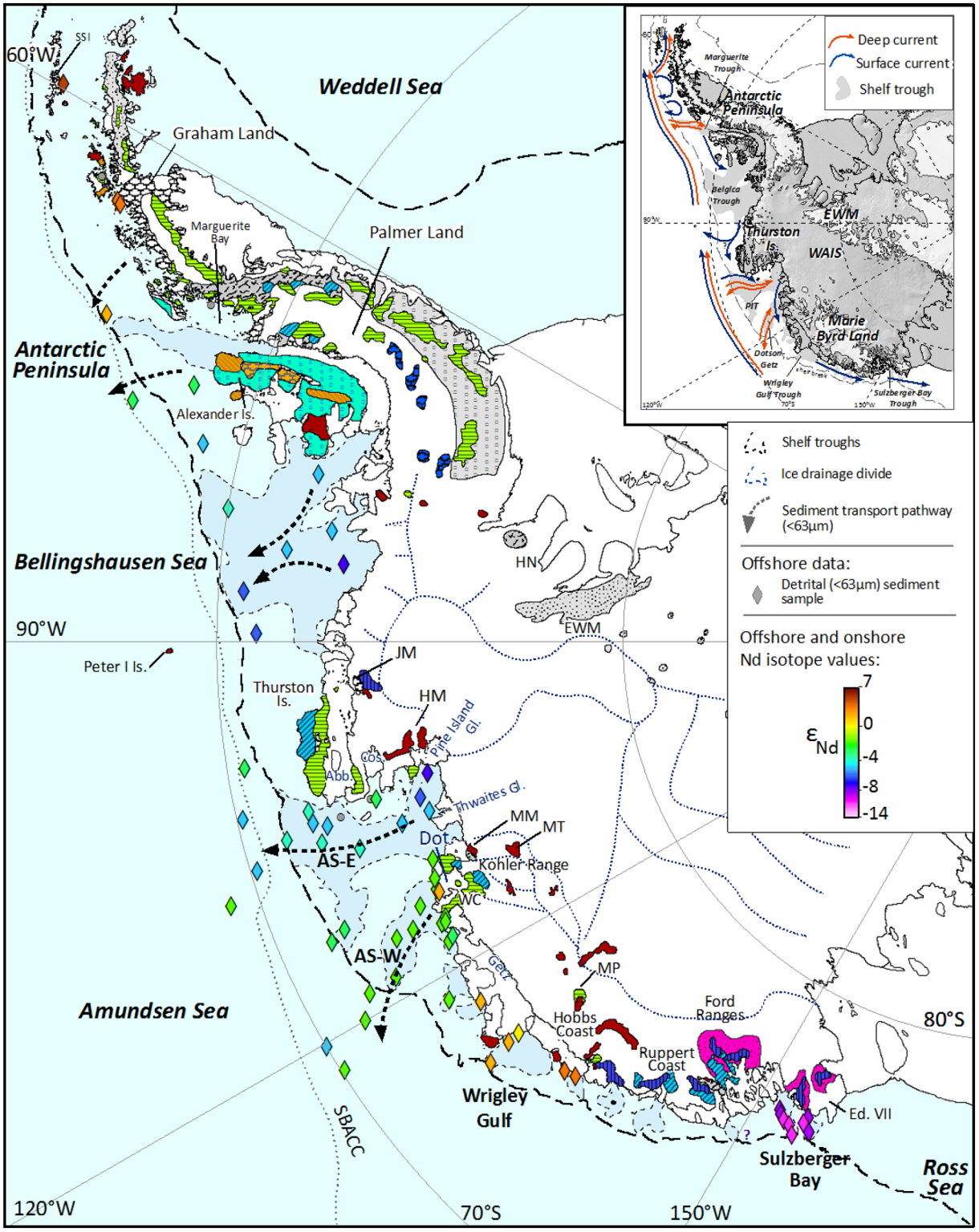
Weddell Sea
Graham Land
Palmer Land
Marguerite Bay
Antarctic Peninsula
Alexander Is.
Bellingshausen Sea
Peter I Is.
Thurston Is.
Amundsen Sea
SBACC
Wrigley Gulf
Ross Sea
Sulzberger Bay
Ed. VII
Ruppert Coast
Hobbs Coast
Ford Ranges
Kohler Range
Pine Island Gl.
Thwaites Gl.
Getz
JM
HM
MM
MT
MP
WC
Dot
Abb
Cos
AS-E
AS-W
HN
EWM
WAIS
PIT
Belgica Trough
Marguerite Trough
Dotson
Getz
Deep current
Surface current
Shelf trough
Shelf troughs
Ice drainage divide
Sediment transport pathway (<63µm)
Offshore data:
Detrital (<63µm) sediment sample
Offshore and onshore Nd isotope values:
εNd
7
0
-4
-8
-14
60°W
90°W
120°W
150°W
70°S
80°S

Figure 9

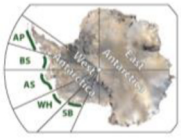

	Antarctic Peninsula	Bellingshausen Sea	Amundsen Sea Eastern	Amundsen Sea Western	Wrigley Gulf - Hobbs Coast	Sulzberger Bay
Geochronology $^{40}Ar/^{39}Ar$ ages	Hornblende / Biotite; < 30 Ma; 30-90 Ma; 90-140 Ma; 140-210 Ma; > 210 Ma	0% – 100%	0% – 100%	0% – 100%	0% – 100%	0% – 100%
Radiogenic fingerprints $^{87}Sr/^{86}Sr$	0.705 - 0.709	0.710 - 0.713	0.708 - 0.724	0.708 - 0.713	0.705 - 0.706	0.741 - 0.749
ε_{Nd}	2.2 – -3.6	-4.3 – -7.2	-3.0 – -7.2	-1.7 – -2.9	-0.5 – 1.3	-10.6 – -11.9
T_{DM}	1100	1180 - 1350	1000 - 1300	900 - 1000	700 - 770	1570 -1700
Trace element compositions Zr/Y	4.0	3.5- 4.7	4.4- 7.7	6.4- 9.2	9.7- 11.9	3.7- 4.8
Sr/Th	27	16- 22	6- 25	9- 17	25- 31	4- 5
Th/Sc	0.60	0.78-1.20	0.56- 1.58	0.91- 1.52	0.77- 1.05	1.19- 1.43
Eu/Eu*	0.79	0.69- 0.84	0.54- 0.76	0.56- 0.82	0.76- 0.82	0.54- 0.60
Clay mineral assemblages Illite; Smectite; Chlorite; Kaolinite	0% – 60%	0% – 60%	0% – 60%	0% – 60%	0% – 60%	0% – 60% *no data*
Major rock sources	• Cenozoic to late Cretaceous granitoids and volcanics • Mesozoic meta-sedimentary rocks	• Mafic (magnetite-rich) and felsic (illmenite-rich) granitoids	• Late Paleozoic, Jurassic and Cretaceous granitoids • Granitoids with crustal assimilation • Pre-Oligocene sedimentary rocks	• Late Palaeozoic and Cretaceous granitoids • Pre-Oligocene sedimentary rocks	• Late Cenozoic alkali basalts • Cenozoic (?) and Cretaceous granitoids	• Paleozoic meta-sedimentary rocks from the Ford Ranges • Cretaceous anorogenic granitoids

Figure 10